PRESSURE OSCILLATIONS IN LIQUID-FUELED RAMJET ENGINES

Thesis by

Vigor Yang

In Partial Fulfillment

of the Requirements for the Degree of

Doctor of Philosophy

California Institute of Technology

Pasadena, California

1984

(Submitted May 17, 1984)

ACKNOWLEDGEMENTS

First, I would like to express sincere thanks to Professor Fred E. C. Culick, my thesis advisor, for his valuable direction and constant encouragement throughout this work. The research program was supported partly by the California Institute of Technology and partly by the Air Force Office of Scientific Research, under Grant No. AFOSR-80-0265.

I am also indebted to Mr. Jay N. Levine for providing the current numerical code for the self-adjusting hybrid scheme, and to Dr. Saleh A. Tanveer for his help with the two-dimensional conformal mapping. Dorothy Eckerman 's assistance in typing the figure captions is greatly appreciated.

Finally, I wish to thank my parents, wife, and family for their love and moral support.

ABSTRACT

Pressure oscillations in liquid-fueled ramjet engines have been studied both analytically and numerically within the low frequency range. We examine first the linear unsteady motions in coaxial-dump configurations. The flowfield in the dump combustor is approximated by division into three parts: a flow of reactants, a region containing combustion products, and a recirculation zone, separated by two infinitesimally thin sheets: the flame and the vortex sheets. The three zones are matched at these sheets by taking into account kinematic and conservation relations. The oscillatory field in the inlet is coupled to the field in the combustor at the dump plane to determine the complex frequencies characterizing the linear stability of the engine. Favorable comparison with the experimental data obtained at the California Institute of Technology has been obtained.

Numerical analysis has been applied to investigate the nonlinear behavior of the shock wave in the inlet diffuser. Both viscous effects and the influences of injecting fuel/air mixture are accounted for. The response of a shock wave to various disturbances, including finite and large amplitude oscillations, has been studied in detail. The results obtained serve as a basis for analyzing the stability characteristics of the inlet flow.

Numerical calculations have also been conducted for the pressure oscillations in side-dump ramjet engines. The flowfields have been constructed in two regions: the inlet section, including a region of fuel injection, and a dump combustor. Each region is treated separately and matched with the other at the dump plane. Following the calculation of the mean flowfield, the oscillatory characteristics of the engine are determined by its response to a disturbance imposed on the mean flow. Results for the frequencies and mode shapes have shown good agreement with the experimental data reported by the Naval Weapons Center, China Lake.

TABLE OF CONTENTS

LIST OF FIGURES

Chapter 1

INTRODUCTION

Recent developments in liquid-fueled ramjet engines led to serious difficulties with pressure oscillations.[1,2] Disturbances of this type, called generically combustion instabilities, are a consequence of the sensitivity of combustion processes to local pressure and velocity fluctuations. If compensating influences acting to attenuate the oscillations are weak, then unsteady motions in the flowfield may reach sufficient amplitude to interfere with proper operation. Table 1.1, taken from reference 2, presents some practical examples in which pressure oscillations have serious impact on engine development programs.

Several modes of oscillations have been observed. They are classified as transverse, longitudinal, and bulk modes according to the frequency range and spacial structure. Because the driving mechanism is ultimately associated with combustion and characteristic features of the inlet and the combustor flows, this classification is best based on the oscillatory flowfields in the combustion chamber.

Transverse mode oscillation, also known as screech instability, may enhance heat transfer to engine components and therefore compromise engine performance and durability. Rogers and Marble[3] carried out experiments in a two-dimensional ramjet combustor. They found that in the presence of screech, vortices were shed at the flame attachment points, distorting the flame front as they were swept downstream. A mechanism for the screeching oscillations was proposed, based upon transient combustion in the vortices. In spite of the potential detrimental influences, this mode of oscillation can be controlled effectively with a flow obstructor such as baffle or a damper such as acoustic liner, and no longer be considered as a major design problem.

Program	Organization	Customer	Combustor Type	Combustion Instability Encountered			Consequences
				Type	Frequency, Hz	Amplitude, %	
Advanced strategic air-launched missile (ASALM)	CSD/UTRC	AFWAL/PORA	Coaxial center dump; high L/D ratio; 16-in. diameter	Longitudinal Transverse	200 1,200	15 to 20 15 to 20	Minor program impact; solution - change fuel distribution
Liquid fuel ramjet engine demonstration (LFRED)	Marquardt	AFWAL/PORT	Coaxial center dump; high L/D ratio; 7-in. diameter	Longitudinal Transverse	300 2,500	20 8	Minor program impact; solution - change fuel distribution
ASALM propulsion technology validation (PTV)	Marquardt	AFWAL/PORA	Coaxial center dump; short L/D ratio; 18-in. diameter	-	-	-	No significant combustion stability problems; successful ground and flight tests
Firebrand	Marquardt	NAVSEA	Podded engine; normal shock inlet; short L/D ratio; 21-in. diameter	Tangential • First mode • Second mode	 900 to 1,000 1,700	 <15 <15	Moderate impact on program cost and schedule; solution - change fuel array
Liquid fuel ramjet (LIFRAM)	Marqumrdt	NWC	Side dump; dual axisymmetric inlets; high L/D ratio; 45° dump angle; 8.2-in. diameter	Longitudinal • High altitude • Low altitude	 80 to 190 80 to 190	 <100 <50	Severe program impact; configuration dropped by NWC
Generic ordnance ramjet engine (GORJE)	NWC	NAVAIR	Side dump; four axisymmetric inlets; short L/D ratio; 12-in. diameter	Longitudinal Tangential (first mode)	250 to 300 2,200	25 15	Severe program impact; flight tests cancelled by NAVAIR
Modern ramjet engine (MRE)	CSD/UTRC	NWC	Side dump; two 2-D inlets; short L/D ratio; 15-in. diameter	-	-	-	No significant stability problems; successful connected-pipe and free-jet test program
Supersonic tactical missile (STM)	CSD/UTRC	Vought/NWC	Side dump; four 2-D inlets; short L/D ratio; 15-in. diameter	-	-	-	No significant stability problems; successful ground and flight tests
Integral booster ramjet technology (IBRT)	UTRC	AFWAL/POR	Side dump (low angle, forward dome); short L/D ratio; 18.5-in. diameter	Transverse Longitudinal	1,500 100 to 150	20 30	Program cost impact; solution - install inlet flow straighteners and change fuel distribution

Note: AFWAL = Air Force Wright Aeronautical Laboratories, L/D = length-to-diameter ratio, NAVAIR = Naval Air Systems Command, NAVSEA = Naval Sea System Command, NWC = Naval Weapons Center, UTRC = United Technologies Research Center, 2-D = two-dimensional

TABLE 1,1. Recent History of Combustion Stability in Liquid-Fueled Ramjet Engines

For contemporary ramjet engines, the low frequency oscillations, including both bulk and longitudinal modes, seem to be most troublesome. It may interact with the inlet shock structure and reduces the stability margin of the system. In the worst situation, the shock is displaced out of the inlet diffuser, leading to failure of the mission. The purpose of this thesis is to examine the unsteady behavior of ramjet engines within the low frequency range.

The basic ramjet configuration illustrated in Figure 1.1 includes a shock wave system at the entrance, an inlet diffuser, a fuel injection system, a dump combustor, and an exhaust nozzle. Air is delivered to a supersonic diffuser, decelerates externally through an oblique shock wave attached to the ramp, then becomes subsonic after passing through the terminal shock wave. Either fuel or fuel-air mixture, depending on the injector and atomizer used, is injected into the main flow downstream of the shock system to provide the necessary combustible mixture. The combustion processes in the dump combustor are extremely complicated, involving turbulent mixing, droplet vaporization, flame propagation, shear layer, recirculating flow, and finite-rate chemical kinetics. Attempts to model these complicated phenomena have been made for over three decades; understanding remains poor. Most of the past work concentrated on investigation of the mean flowfields in the combustor; information available on the treatment of the unsteady flowfields is limited. An excellent review paper concerning the computer modeling of the steady combustion in ramjet combustor has been given by Lilley.[4]

Experimental investigations of low frequency oscillations in ramjet engines have been recently conducted by several research organizations. The results obtained have provided information about the effects of combustor configuration, fuel management, and inlet system on the overall instability processes. Jarosinski and Wojcicki[5] considered the low frequency combustion instability in a dump combustor which is connected upstream to an acoustic resonator. Shadowgraphs and

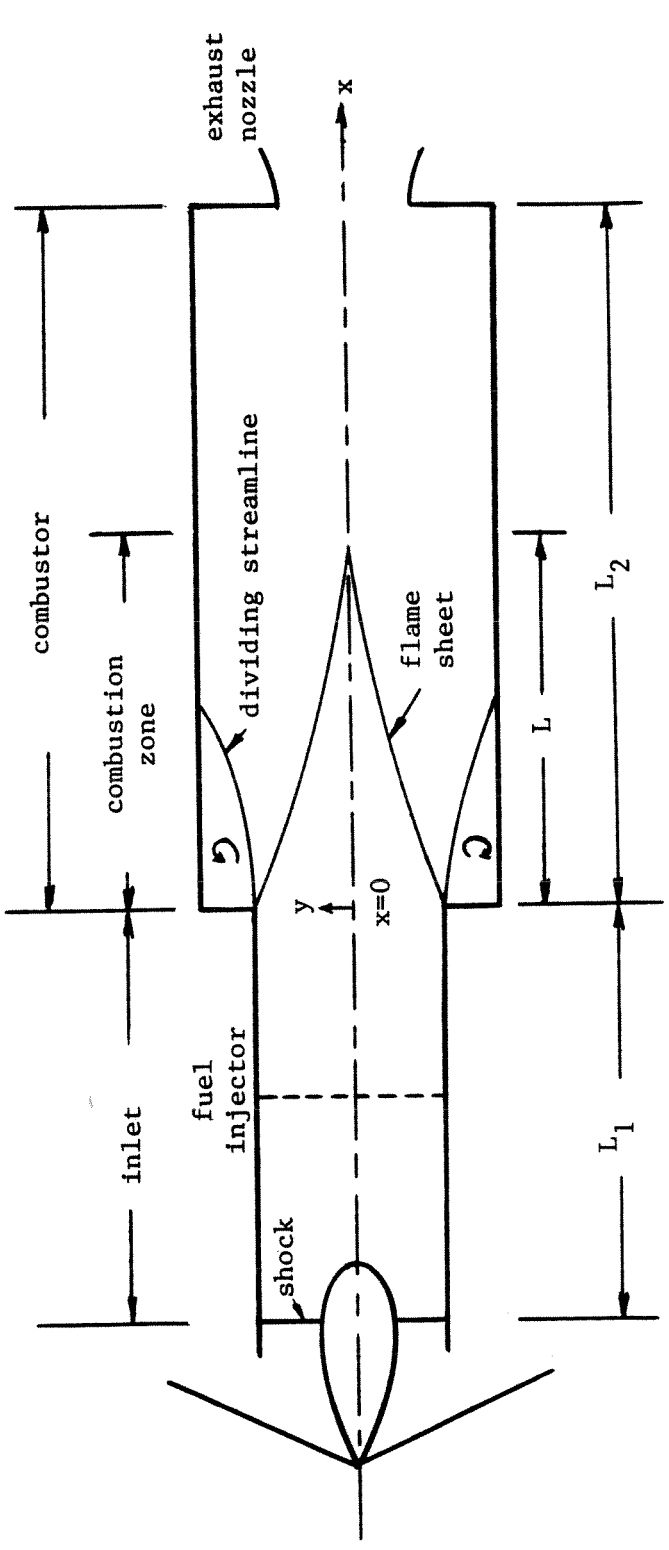

FIGURE 1.1. Typical Geometry for a Ramjet Engine with a Dump Combustor

motion pictures were taken, and measurements were made of the pressure, velocity and local chemi-ionization. They concluded that the combustion instability of this type is closely related to the instability of laminar flames although the combustion processes are distributed throughout much of the volume.

Rogers[6] summarized the features of the pressure oscillations in two liquid-fueled engines having very different geometrical configurations. One had an coaxial dump with a single inlet, and the other had two inlets with a side dump arrangement. Significant differences appear in the structure of the oscillations excited in the combustion chamber. Schadow and co-works have studied[7-9] oscillations in several research dump combustors with special attention focused on the inlet shock/acoustic wave interaction. The entire device was extensively instrumented during testing. Two kinds of data have been taken under various operational conditions: the acoustic wave structure and the properties of the inlet shock. In references 10 and 11 results for various dual side-dump ramjet combustors were reported.

So far, most analytical treatments of low frequency motions in ramjet engines employed linear perturbation techniques, giving results valid in the limit of small amplitudes. Nonlinear analysis has not yet been applied to this subject although some numerical solutions of nonlinear governing equations have been obtained.[12] Culick and Rogers[13] gave the first detailed analysis with both inlet and combustor accounted for. Some formulas were given for frequencies and mode shapes approximating the oscillations which had been observed in two engines. The combustion processes were accommodated in a crude fashion, not treated in detail. Later, Yang and Culick[14] constructed a one-dimensional analysis using an integral formulation. A more realistic model of the mean flowfield and a proper treatment including the inlet diffuser were included. Favorable comparison of calculations with experimental data for the amplitude and phase distributions in an axial laboratory device

were acquired. The same authors[12] also carried out a numerical analysis for dual side-dump ramjet engines. The detailed information obtained provides a better understanding of the flowfields, especially for finite and large amplitude oscillations. Reardon[15] applied a combustion time lag model, originally developed for dealing with bulk oscillations in liquid propellant rockets, to the corresponding ramjet problems. In reference 16 the rumble (bulk mode) oscillations in a coaxial dump combustor have been investigated by considering the interplay of entropy and acoustic waves. The acoustic field in the inlet is represented as a leftward traveling wave, the reflection process of the shock being ignored.

Because observations of the unsteady behavior suggest that the low frequency oscillations do not involve significant transverse motions anywhere in the engine, the work reported here is based on a quasi one-dimensional model. We start with an analytical linear analysis, followed by a numerical nonlinear analysis. In Chapter 2 a simple linear stability model accommodating both acoustic and entropy fluctuations is presented to identify the acoustic modes associated with pressure oscillations. The engine is approximated by division into two parts: the inlet section and the combustion chamber. Each region is treated separately and then matched with the other at the dump plane. The combustion zone is assumed to be acoustically compact, its unsteady behavior being represented by the Crocco's sentitive time-lag hypothesis.[17] As a first approximation, we ignore the cross sectional area change in each section and assume the mean flowfields to be uniform. The oscillatory field is therefore the superposition of two simple plane acoustic waves running downstream and upstream, and an entropy wave carried with the mean flow. Combination of these wave equations with the proper boundary conditions at the shock wave and the entrance of the exit nozzle forms a well-posed problem for the unsteady motion.

While this analysis provides reasonable solution for the frequencies and mode shapes, it is seriously incomplete not including, among other things, treatment of the mean flowfield in the combustor. Chapter 3 is devoted to correcting this matter. It is intended to develop a suitable simple and realistic model accommodating the fundamental features of the flowfield in the combustor, including the flame front, the shear layer, and the recirculating flow. For low frequency oscillations, the flame front and the shear layer can be represented adequately by two infinitesimally thin sheets: the flame and the vortex sheets respectively. The flowfield is, accordingly, decomposed into a flow of reactants, a region containing combustion products, and a recirculation zone, as shown in Figure 1.1. The three zones are then matched at those sheets by taking into account conservation and kinematic relations. Determination of their shapes is part of the solution. The unsteady motions are treated within linear acoustics and approximated as quasi one-dimensional motion in each region.

In Chapters 2 and 3 the oscillations are confined to the small amplitude regime where linear analysis is properly used. The main results of the analysis are frequencies, growth rates, mode shapes, and perhaps more important, the first step towards nonlinear analysis. For many practical cases, the flowfields involve finite/large amplitude motions in which nonlinear effects play essential roles. It is of fundamental importance to answer such questions as: how does the flowfield respond to a disturbance with finite or large amplitude?; and how does an initially small amplitude disturbance grow and finally reach certain limiting value? Officially, this can be achieved using either asymptotic expansion method or numerical technique. Each method has advantages which are complementary to the other. A fruitful discussion of an asymptotic expansion method has been recently given by Awad[18] in his study of combustion instabilities in solid propellant rockets. Owing to the singular behavior of the shock wave and to the complicated

configuration of the engine, we resort to numerical methods here.

Chapter 4 starts with the formulation of a two-phase flow problem with both gas and liquid fuel accounted for, followed by the specification of boundary conditions. After a review of the theories underlying numerical methods for hyperbolic problems, some important criteria for choosing proper solution techniques are discussed. This chapter serves as a basis for the work given in the subsequent chapters.

In chapter 5 the response of a normal shock wave to various disturbances is discussed. This is motivated by two reasons. First, the greatest combustion related operational problem in ramjet engines is inlet unstart due to the loss of shock stability. Second, the shock wave is an important upstream boundary in the entire analysis. The oscillatory behavior of the engine depends strongly on the reflection processes at the shock. Both linear and numerical nonlinear analyses are carried out. The influences of shock motion on the downstream flow properties, such as entropy and mass flow rate, are also discussed in great detail.

Chapter 6 deals with pressure oscillations in dual side-dump ramjet engines, using a one-dimensional numercial analysis. The engine is treated in two parts: the inlet section, including a region of two-phase flow downstream of fuel injection, and a dump combustor. Combustion processes are crudely modeled as a stirred reactor, occupying the forward portion of the combustor, followed by a length of plug flow. Calculations are first carried out for the steady flowfields. The unsteady behavior of the engine is then determined by its response to a small disturbance imposed on the mean flow. In addition to the spacial distributions of flow properties at various times, spectral information is obtained for the time history of the pressure.

Finally, we conclude this thesis with a summary of the results and future exten-

sions of the analysis. The work reported here provides a convenient means of analyzing the unsteady behavior of liquid-fueled ramjet engines within the low frequency range. Favorable comparison of calculations with experimental data for various laboratory devices, including both coaxial- and side-dump engines, has been obtained.

REFERENCES 1

1. Culick, F. E. C., 'Report of the JANNAF Workshop on Pressure Oscillations in Ramjets," *1980 JANNAF Propulsion Meeting*, March 1980; *17th JANNAF Combustion Meeting*, September 1980.

2. Waugh, R. C., et al., 'Ramjet Combustor Instability Investigation: Literature Survey and Preliminary Design Study," *United Technologies Report CSD-2770-IR-1*, Jan.1982.

3. Rogers, D. E. and Marble, F. E., "A Mechanism for High Frequency Oscillations in Ramjet Combustors and Afterburners," *Jet Propulsion*, Vol.26, 1956, pp.458-462.

4. Lilley, G. D., 'Computer Modeling of Ramjet Combustor," *AIAA Journal*, Vol.19, No.12, 1981, pp.1582-1563.

5. Jarosinski, J. and Wojcicki, S., 'The Mechanism of Interaction between a Combustion Region and Acoustic Resonator," *Acta Astronautica*, Vol.3, 1976, pp.567-572.

6. Rogers, T., 'Pressure Oscillations in Small Ramjet Engines," *16th JANNAF Combustion Meeting*, September 1980.

7. Crump, J. E., Schadow, K. C., and Blomshield, F., and Bicker, C. J., 'Combustion Instability in a Research Dump Combustor: Pressure Oscillations," *18th JANNAF Combustion Meeting*, October 1981.

8. Schadow, K. C., Crump, J. E., and Blomshield, F., 'Combustion Instability in a Research Dump Combustor: Inlet Shock Oscillations," *18th JANNAF Combustion Meeting*, October 1981.

9. Crump, J. E., Schadow, K. C., Blomshield, F., Culick, F. E. C., and Yang, V., 'Combustion Instability in Dump Combustor: Acoustic Mode Determination," *19th JANNAF Combustion Meeting*, November 1982.

10. Clark, W. H., 'Experimental Investigation of Pressure Oscillations in a Side-Dump Ramjet Combustor," *Journal of Spacecraft and Rockets*, Vol.19, No.1, January 1982, pp.47-53.

11. Clark, W. H., 'Geometric Scale Effects on Combustion Instabilities in a Side-Dump Liquid Fuel Ramjet," *19th JANNAF Combustion Meeting*, October 1982.

12. Yang, V. and Culick, F. E. C., 'Numerical Calculations of Pressure Oscillations in a Side-Dump Ramjet Engine," *1984 AIAA Sciences Meeting*, Jan.1984.

13. Culick, F. E. C. and Rogers, T., 'Modeling of Pressure Oscillations in Ramjets," *AIAA/SAE/ASME 16th Joint Propulsion Conference*, June 1980.

14. Yang, V. and Culick, F. E. C., 'Linear Theory of Pressure Oscillations in Liquid-Fueled Ramjet Engines," *AIAA 21st Aerospace Sciences Meeting*, Jan.1983.

15. Reardon, F. H., 'The Sensitive Time Lag Model Applied to Very Low Frequency Oscillations in Side-Dump Liquid-Fueled Ramjet Engines," *20th JANNAF Combustion Meeting*, Oct.1983.

16. Abouseif, G. E., Keklak, J. A., and Toong, T. Y., 'Ramjet Ramble: The Low Frequency Instability Mechanism in Coaxial Dump Combustors," *submitted for publication in AIAA Journal*, May 1983.

17. Crocco, L. and Cheng, S. I., *Theory of Combustion Instability in Liquid Propellant Rocket Motors*, AGARD No.8, Butterworths Scientific Publications, 1956.

18. Awad, E. A., *Nonlinear Acoustic Instabilities in Combustion Chamber*, Ph.D. Thesis, California Institute of Technology, August 1983.

Chapter 2

A SIMPLE LINEAR ANALYSIS

In this chapter, a simple linear stability analysis of low frequency pressure oscillations is developed, based on a one-dimensional approximation for a device having a coaxial inlet, as shown in Figure 2.1. The engine contains two parts, the inlet duct and the combustion chamber; in each region we treat the flowfield separately. Boundary conditions are specified as admittance functions for a normal shock at the entrance plane and for a choked nozzle at the exhaust plane. The solutions for the two chambers are then matched at the dump plane to determine the unsteady behaviors of the engine. Recent experiments conducted at the Naval Weapons Center[1,2] prompted the work discussed here.

Stability of pressure oscillations may be expressed in terms of gains and losses of energy for the acoustic waves. Within linear analysis, these energy exchange processes can be conveniently classified as acoustic, entropy, and vorticity modes according to the mechanisms controlling oscillations.[3] Each mode behaves independently, but can be generated by the others through the interaction with the mean flowfields and the boundaries. Since the vorticity mode is a multidimensional effect, in the present analysis only acoustic and entropy disturbances are accounted for. Treated in this way, the process contributing to the excitation of oscillations can be visualized as follows. When pressure fluctuations occur in the combustion zone, density and temperature fluctuations are produced which are not in general related isentropically. The isentropic fluctuations propagate with the speed of sound, but the non-isentropic residues are carried with the mean flow. Upon reaching the exit plane and the exhaust nozzle, these entropy fluctuations interact with the boundary and the local flow to produce pressure fluctuations which in turn propagate upstream. If those disturbances arrive, at the proper time,

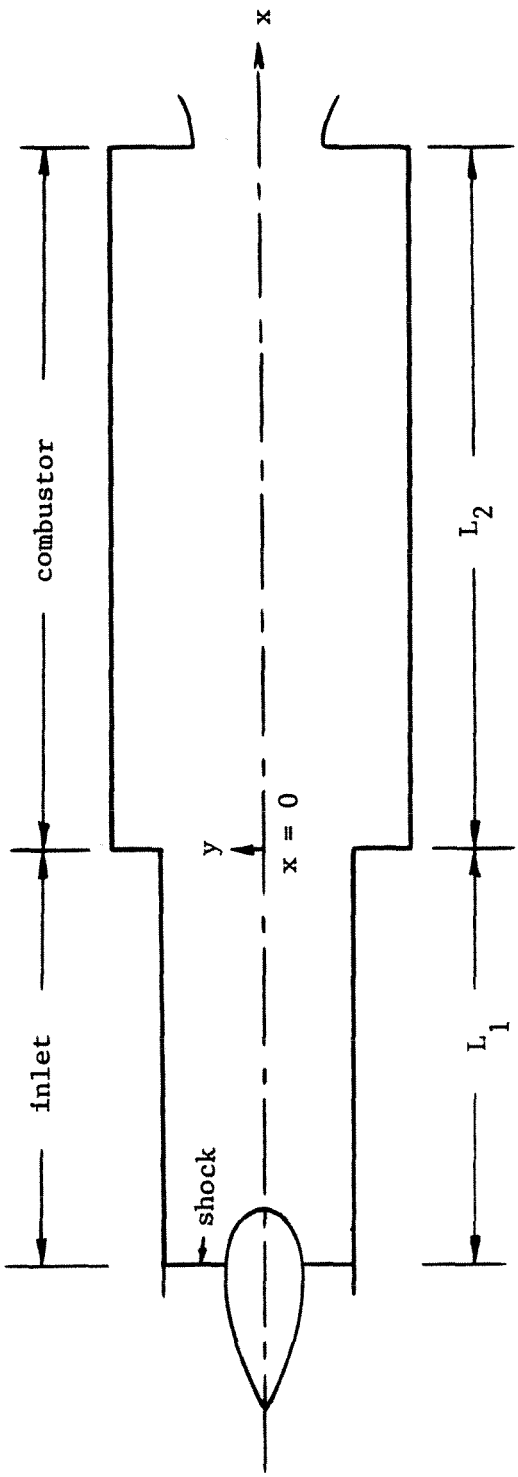

FIGURE 2.1. Schematic Diagram of Ramjet Engine

at the upstream region where the entropy wave generated, the process may be repeated cyclically. Thus a feedback loop has been established in the flow and unstable motions may be a result.

Two major assumptions are introduced here. First, because tests with premixed gaseous systems have shown that fuel droplet breakup and/or vaporization is not a necessary condition for oscillatory combustion,[1] the flow is treated as single-phase. Second, the combustion zone is assumed to be acoustic compact, its length being much smaller than the acoustic wave length, and confined to the dump plane across which jumps in temperature and density take place. While this approximation applies only for very low frequency oscillation in the strict sense, it serves as a convenient means of identifying acoustic mode structures and assessing the influence of various parameters on the stability characteristics of the engine. The obvious deficiency due to the neglect of distributed combustion will be corrected in the next chapter.

The analysis starts with formulating the equations for acoustic and entropy fluctuations in a one-dimensional flowfield. After the fields in the inlet and combustor have been found separately, a transcendental equation for the complex frequency characterizing the oscillatory field in the entire engine is obtained by applying proper matching conditions at the dump plane. Calculated results are then compared with the experimental data reported in reference 2. Favorable agreement suggests that the model is a satisfactory representation of some of the global behavior of the device.

2.1. Formulation

If we neglect viscous effects and all other distributed losses, the equations governing the one-dimensional flowfield in the inlet and the combustor are

mass equation

$$\frac{\partial \rho}{\partial t} + \frac{\partial}{\partial x}\rho u = 0 \tag{2.1.1}$$

momentum equation

$$\frac{\partial}{\partial t}\rho u + \frac{\partial}{\partial x}\rho u^2 + \frac{\partial p}{\partial x} = 0 \tag{2.1.2}$$

energy equation

$$\frac{\partial s}{\partial t} + u\frac{\partial s}{\partial x} = 0 \tag{2.1.3}$$

The energy equation asserts that the entropy is preserved following fluid particle since the combustion has been confined to the dump plane.

To simplify the analysis, the cross-sectional area changes in each region are ignored. The rapid variations in the diffuser and the nozzle sections will appear indirectly through their influences on the boundary conditions. Therefore, we treat the problem of oscillatory waves in a uniform mean flowfield. The flow variables are accordingly written as sums of mean and fluctuating quantities:

$$\rho(x,t) = \bar{\rho} + \rho'(x,t) \tag{2.1.4a}$$

$$u(x,t) = \bar{u} + u'(x,t) \tag{2.1.4b}$$

$$p(x,t) = \bar{p} + p'(x,t) \tag{2.1.4c}$$

$$s(x,t) = \bar{s} + s'(x,t) \tag{2.1.4d}$$

Substitution of these decomposed variables into (2.1.1-3) and collection of terms of first order in the fluctuations produce the equations for linear motions:

$$\frac{\partial \rho'}{\partial t} + \bar{\rho}\frac{\partial u'}{\partial x} + \bar{u}\frac{\partial \rho'}{\partial x} = 0 \tag{2.1.5}$$

$$\rho \frac{\partial u'}{\partial t} + \bar{\rho}\bar{u} \frac{\partial u'}{\partial x} + \frac{\partial p'}{\partial x} = 0 \tag{2.1.6}$$

$$\frac{\partial s'}{\partial t} + \bar{u} \frac{\partial s'}{\partial x} = 0 \tag{2.1.7}$$

For convenience, the equation of state for a perfect gas is expressed in terms of entropy:

$$p = \rho^{\gamma} e^{(\frac{s}{c_v})} \tag{2.1.8}$$

Linearization leads to

$$\frac{\rho'}{\bar{\rho}} = \frac{1}{\gamma} \frac{p'}{\bar{p}} - \frac{s'}{c_p} \tag{2.1.9}$$

Hence, a small change in density may be attributed to both acoustic and entropy oscillations. Substitution of (2.1.9) for the density fluctuations in (2.1.5) gives

$$\frac{\partial p'}{\partial t} + \gamma \bar{p} \frac{\partial u'}{\partial x} + \bar{u} \frac{\partial p'}{\partial x} = 0 \tag{2.1.10}$$

This equation involves no entropy fluctuation, the entropy mode being decoupled from the acoustic mode. For convenience, (2.1.10) is further combined with (2.1.6) to produce a single wave equation governing the acoustic motions.

$$(\frac{\partial}{\partial t} + \bar{u} \frac{\partial}{\partial t})^2 p' - \bar{a}^2 \frac{\partial^2 p'}{\partial x^2} = 0 \tag{2.1.11}$$

The field consists of two waves travelling upstream and downstream. Appropriate solutions to (2.1.11) and (2.1.6) are

$$p' = [P^+ e^{iKx} + P^- e^{-iKx}] \, e^{-i(\Omega t + \overline{M}Kx)} \tag{2.1.12}$$

$$u' = \frac{1}{\bar{\rho}\bar{a}} [P^+ e^{iKx} - P^- e^{-iKx}] \, e^{-i(\Omega t + \overline{M}Kx)} \tag{2.1.13}$$

where Ω is the complex frequency, P^+ and P^- are complex amplitudes of the right and the left running waves, and K is the modified wave number defined as

$$K = \frac{k}{1-\bar{M}^2} = \frac{\Omega/\bar{a}}{1-\bar{M}^2} = \frac{(\omega + i\alpha)/\bar{a}}{1-\bar{M}^2} \tag{2.1.14}$$

The wave number is complex, the imaginary part being nonzero because of losses in the system.

As far as the entropy fluctuation is concerned, it is convected downstream with the mean flow. The solution to (2.1.7) can be written as

$$s' = S(\frac{c_p}{\gamma \bar{p}})e^{-i(\Omega t - \frac{\Omega}{\bar{u}}x)} \tag{2.1.15}$$

The quantity in the parentheses is introduced so that S has the dimension of pressure.

2.2 Acoustic Field in the Inlet

Because the entropy fluctuation associated with unsteady shock motion is a third order effect in comparison with the pressure fluctuation,[4] the inlet flow is considered isentropic. Consequently, the oscillatory flowfields in this region are

$$s_1' = 0 \tag{2.2.1}$$

$$p_1' = [P_1^+ e^{iK_1 x} + P_1^- e^{-iK_1 x}]\, e^{-i(\Omega t + \bar{M}_1 K_1 x)} \tag{2.2.2}$$

$$u_1' = \frac{1}{\bar{\rho}_1 \bar{a}_1}[P_1^+ e^{iK_1 x} - P_1^- e^{-iK_1 x}]\, e^{-i(\Omega t + \bar{M}_1 K_1 x)} \tag{2.2.3}$$

The subscript 1 refers to the quantity in the inlet section. The influence of the shock and diffuser can be conveniently represented by an admittance function A_s, defined at the plane $x=-L_1$:

$$A_s = \bar{\rho}_1 \bar{a}_1 \frac{u_1'}{p_1'} \tag{2.2.4}$$

If the shock behaves quasi-steady and the flow is isentropic on both sides of the shock, then the admittance function presented to downstream disturbances is[5]

$$A_s = \frac{-\frac{2}{\gamma+1}\left[\frac{\bar{M}_{1s}^2+1}{\bar{M}_{2s}^2}\right]i\Omega_s + \frac{2\gamma}{\gamma+1}\bar{M}_{2s}}{\frac{4\bar{M}_{1s}}{\gamma+1}\left[\frac{\bar{p}_{1s}}{\bar{p}_{2s}}\right]i\Omega_s - \frac{1}{\gamma}\left[\frac{\gamma^2+1}{\gamma+1}\right]\left[\frac{\bar{M}_{1s}^2+(\frac{\gamma-1}{\gamma^2+1})}{\bar{M}_{1s}^2-(\frac{\gamma-1}{2\gamma})}\right]} \tag{2.2.5}$$

where the subscript 1s and 2s represent the quantities immediately in front of and behind the shock, and the dimensionless frequencies Ω_s is

$$\Omega_s = \frac{\omega/\bar{a}_{2s}}{\left[\frac{1}{A}\frac{dA}{dx}\right]_{shock}} \tag{2.2.6}$$

In this representation, the shock wave acts to dissipate acoustic energy. The left-running wave is effectively attenuated, leading to a small-amplitude reflected wave travelling downstream. Since this is a linear problem, the wave amplitude can be arbitrarily specified without violating the governing equation. For convenience, P_1^- is chosen to be unity so (2.2.2) and (2.2.3) may be written in the following forms by applying acoustic reflection condition at the shock ($x=-L_1$).

$$p_1' = [\beta_s e^{iK_1(2L_1+x)} + e^{-iK_1x}]e^{-i(\Omega t + M_1K_1x)} \tag{2.2.7}$$

$$u_1' = \frac{1}{\bar{\rho}_1\bar{a}_1}[\beta_s e^{iK_1(2L_1+x)} - e^{-iK_1x}]e^{-i(\Omega t + M_1K_1x)} \tag{2.2.8}$$

where β_S represents the acoustic reflection coefficient at the shock and can be determined from the shock admittance function.

$$\beta_s = \frac{1+A_s}{1-A_s} \tag{2.2.9}$$

By rearranging (2.2.7), the acoustic pressure is expressed in terms of its amplitude and phase.

$$p_1' = P_1 e^{-i(\Omega t + \bar{M}_1K_1x - \psi_p)} \tag{2.2.10}$$

where

$$P_1 = [1 + |\beta_s|^2 + 2|\beta_s|\cos(2K_1x + \varphi)]^{\frac{1}{2}} \tag{2.2.11}$$

$$\psi_p = \tan^{-1}\left[\frac{-\sin K_1x + |\beta_s|\sin(K_1x + \varphi)}{\cos K_1x + |\beta_s|\cos(K_1x + \varphi)}\right] \tag{2.2.12}$$

,and φ is the phase of the reflection coefficient β_S. It is clear that the acoustic field depends only on the admittance function for the shock wave, the Mach number of the flow, and the complex wave number because any viscous losses in the inlet have been ignored. The calculation of the complex wave number will be described in detail later.

To check the validity of this simple analysis and the shock admittance given by (2.2.5), a series of numerical comparison with the experimental results obtained at the Naval Weapons Center[2] were conducted, using the measured frequencies of oscillations as known conditions. Figure 2.2 shows a typical comparison of the calculated and the measured phase distributions. The phase varies almost linearly because of the small acoustic reflection coefficient at the shock β_S. A good approximation is given by $(\bar{M}_1+1)K_1x$, as easily proven by (2.2.10) and (2.2.12). Figure 2.3 illustrates the acoustic pressure distributions at various times within one cycle of oscillation. The presence of the extremes on the envelope of the pressure amplitude indicates that the wave is non-stationary standing, rather than travelling. Each pressure node moves around its mean position periodically, no fixed node point being observed. The same conclusion was reached experimentally by Crump et al.[2]

2.3 Oscillatory Field in the Dump Combustor

The oscillatory flowfields in the combustion chamber are similar to those in the inlet except for the presence of an entropy wave due to unsteady combustion. Following the analysis given in Section 2.1, the equations governing the unsteady motions are

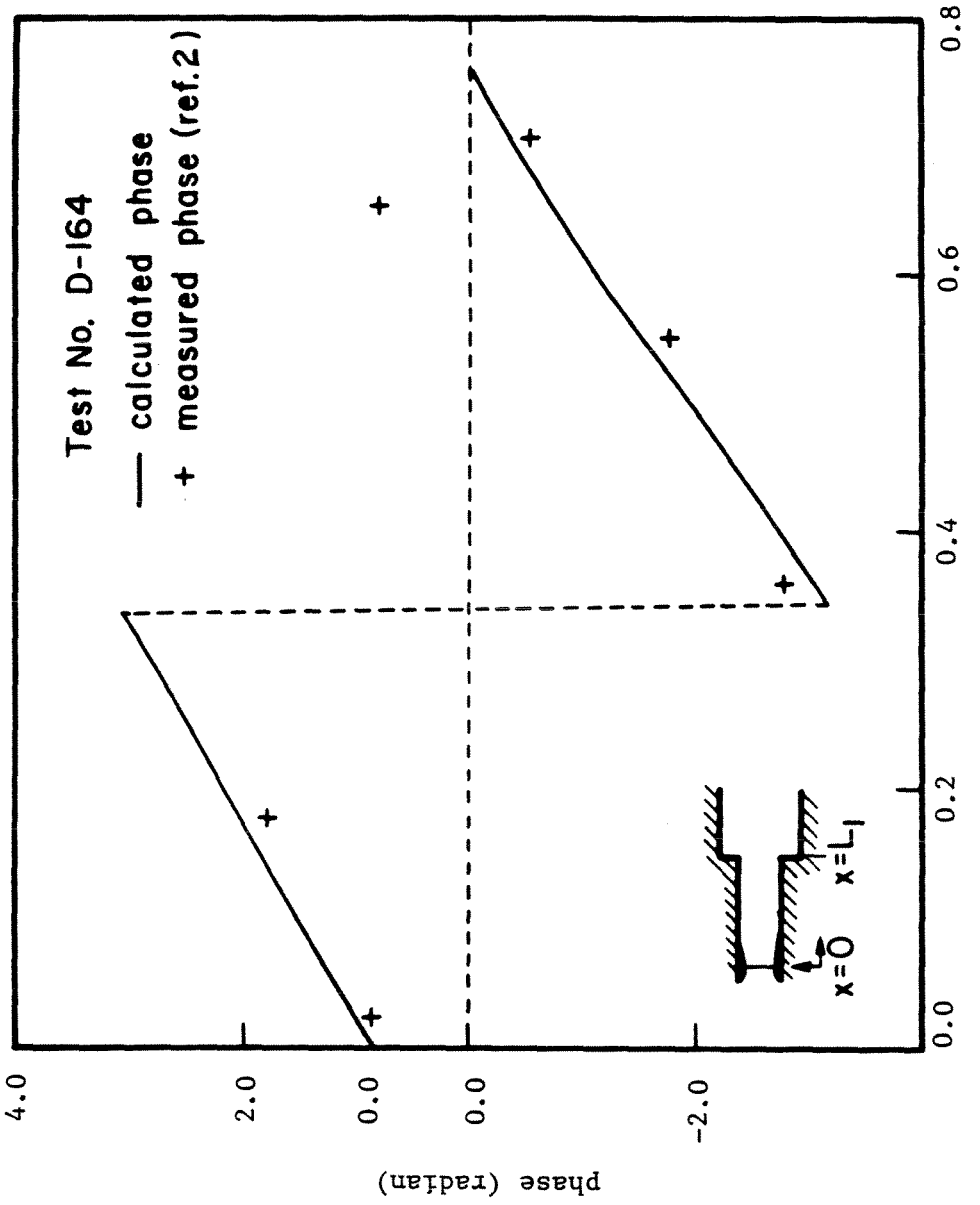

FIGURE 2.2. Measured and Calculated Phase Distributions in the Inlet (f = 300 Hz)

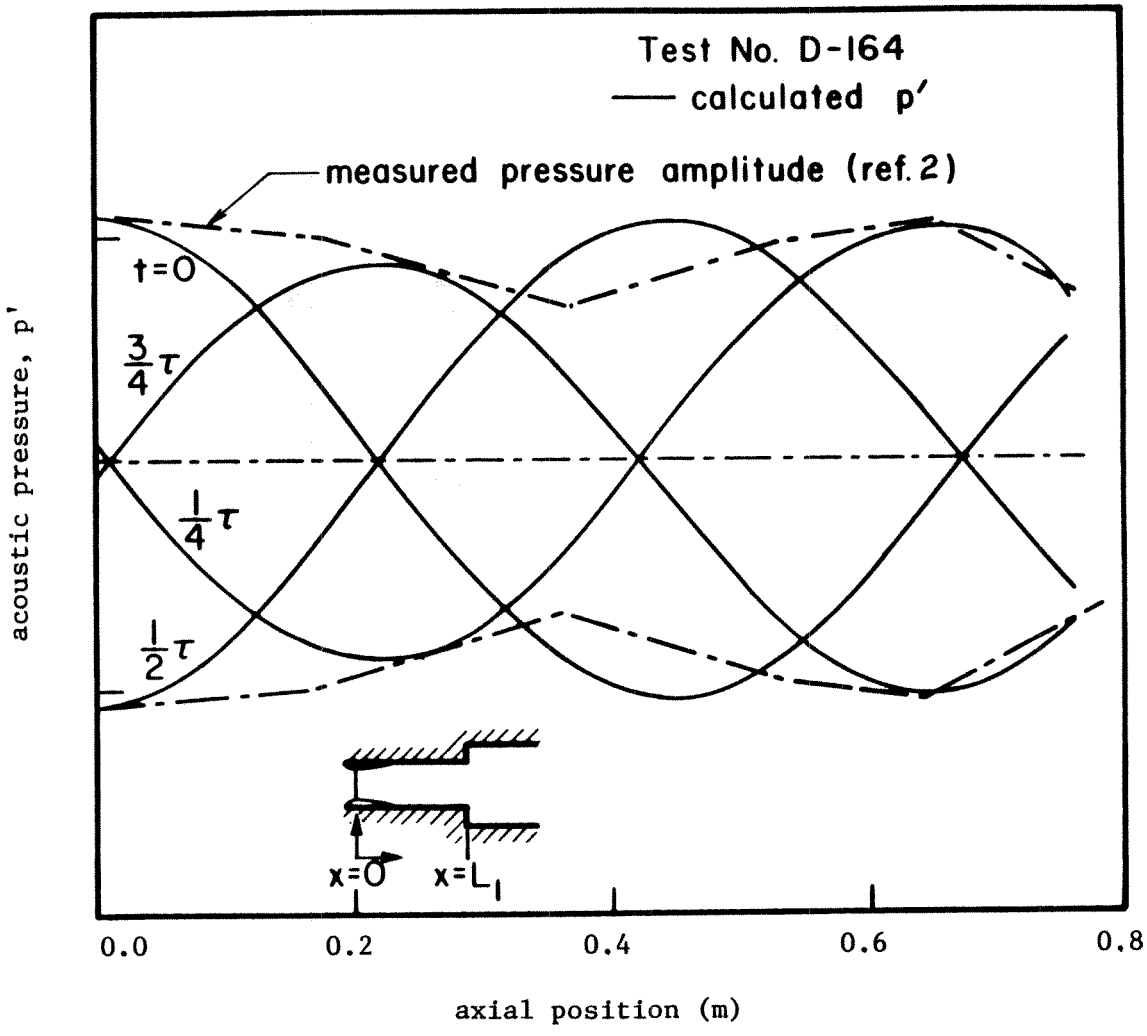

FIGURE 2.3. Measured and Calculated Acoustic Pressure Distributions in the Inlet (f = 300 Hz)

$$s_2' = S_2\left(\frac{c_{p_2}}{\gamma_2 \bar{p}_2}\right) e^{-i\left(\Omega t - \frac{\Omega}{u_2} x\right)} \tag{2.3.1}$$

$$p_2' = \left[P_2^+ e^{iK_2 x} + P_2^- e^{-iK_2 x}\right] e^{-i(\Omega t + M_2 K_2 x)} \tag{2.3.2}$$

$$u_2' = \frac{1}{\bar{\rho}_2 \bar{a}_2}\left[P_2^+ e^{iK_2 x} - P_2^- e^{-iK_2 x}\right] e^{-i(\Omega t + M_2 K_2 x)} \tag{2.3.3}$$

The subscript 2 denotes the quantity in the combustion chamber. Since the reflected pressure fluctuation at the nozzle entrance $x=L_2$ contains contributions from both the incident acoustic and entropy waves, we have

$$P_2^- = \beta_a P_2^+ e^{2iK_2 L_2} + \beta_e S_2\left(\frac{c_{p_2}}{\gamma_2 \bar{p}_2}\right) e^{iL_2\left(K_2 + M_2 K_2 + \frac{\Omega}{u_2}\right)} \tag{2.3.4}$$

where β_a and β_e are the acoustic and the entropy reflection coefficients respectively. For a choked compact nozzle, they have been found to be[6]

$$\beta_a = \frac{2 - (\gamma - 1)\bar{M}_2}{2 + (\gamma - 1)\bar{M}_2} \tag{2.3.5}$$

$$\beta_e = \frac{-\bar{M}_2}{2 + (\gamma - 1)\bar{M}_2} \tag{2.3.6}$$

The reflected pressure wave is out of phase with the incident entropy wave: a positive entropy disturbance always produces a negative acoustic disturbance. This phenomenon can be easily explained as follows. For a choked compact nozzle, the Mach number at the entrance of the nozzle is fixed by the area ratio of the entrance to the throat. Since a positive entropy oscillation means an increase of the speed of sound through its influence on the temperature field, the velocity must increase as well in order to maintain the same Mach number. In general, this can be achieved only by a negative pressure disturbance.

As a consequence of the decoupling of the acoustic from the entropy fluctuations, the temperature disturbance is conveniently split into two parts: one is

related isentropically to the pressure oscillation p', and the other has zero p' and is related to the entropy oscillation s', according to the linearized equation of state.

$$\frac{T'}{\bar{T}} = T_p' + T_s' = \frac{\gamma - 1}{\gamma}\frac{p'}{\bar{p}} + \frac{s'}{c_p} \tag{2.3.7}$$

where T_p' and T_s' denote the contributions from p' and s' respectively. Note that both T_p' and T_s' are directly proportional to p' and s', but no general statement can be made for the entire temperature disturbance due to the phase difference α between them. Figure 2.4 shows the time histories of T' for various α, where T_p' and T_s' are represented by two sinusoidal functions.

2.4 Oscillatory Field in the Entire Engine

The oscillatory field in the inlet is coupled to the field in the dump combustor in order to determine the stability characteristics of the engine. This procedure is based on continuity of mass, pressure, and total energy at the dump plane. By linearizing the continuity relations, the conditions to be satisfied at x=0 are

continuity of mass

$$\bar{\rho}_1 u_1' + \rho_1' \bar{u}_1 = (\bar{\rho}_2 u_2' + \rho_2' \bar{u}_2)\frac{A_2}{A_1} \tag{2.4.1}$$

continuity of pressure

$$p_1' = p_2' \tag{2.4.2}$$

continuity of energy

$$\bar{u}_1 u_1' + c_{p_1} T_1' + Q' = \bar{u}_2 u_2' + c_{p_2} T_2' \tag{2.4.3}$$

where Q' is the fluctuation of heat release at the dump plane. The momentum conservation relation is represented by the continuity of pressure. The complete momentum balance including pressure and momentum flux does not hold as the inlet flow is subsonic and discharged into the combustor through the dump plane

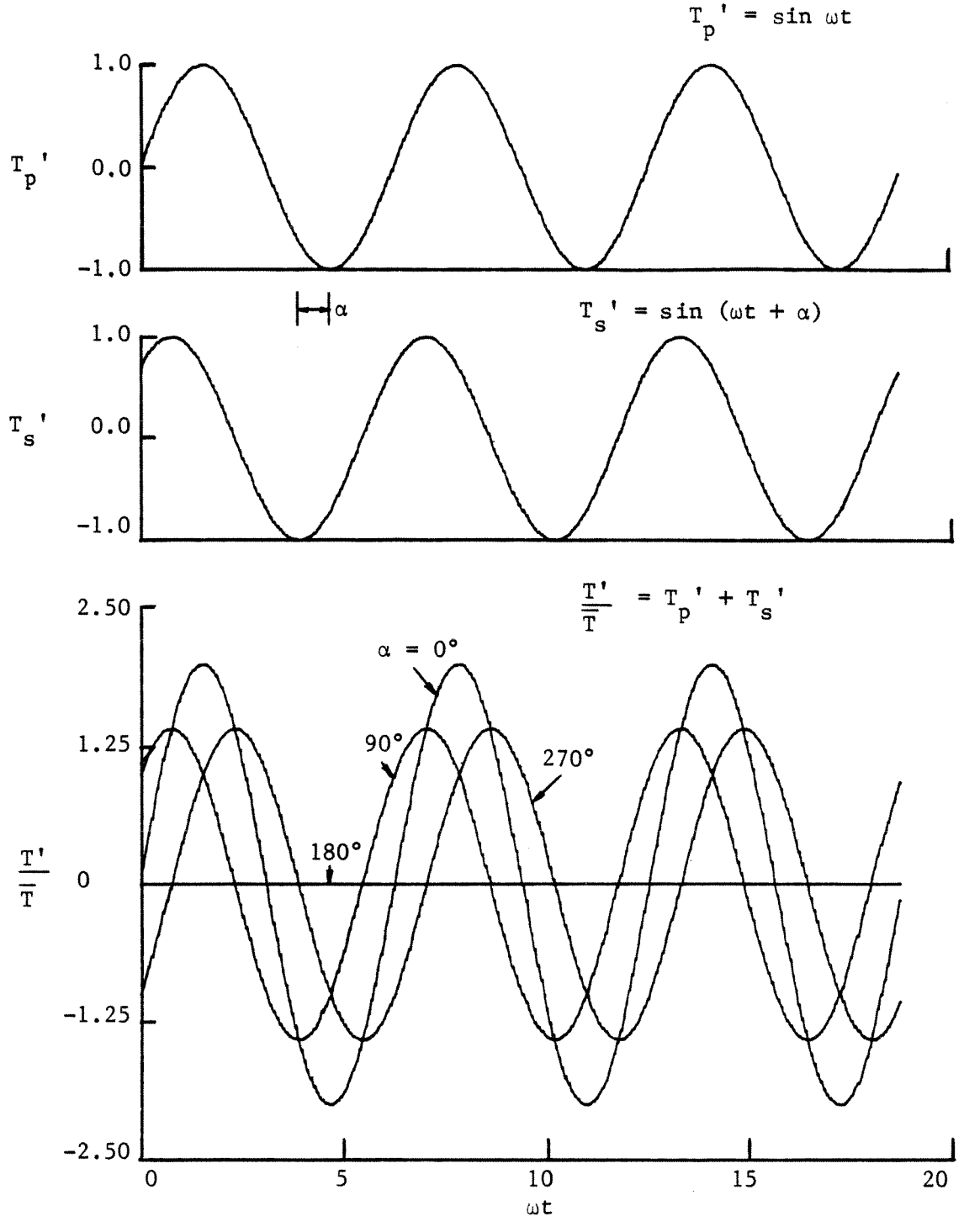

FIGURE 2.4. Dependence of Temperature Fluctuation on Pressure and Entropy Disturbances

at which the cross-sectional area changes suddenly. It would imply a physically unrealistic shock at the dump plane and violation of the second law of thermodynamics. A comprehensive discussion of this matter has been given in Section 4.7 of reference 7. The energy balance (2.4.3) is required only when the entropy fluctuation is included in the analysis. For a pure acoustic model, this equation is replaced by the isentropic relation between density and pressure fluctuations.

The energy source term Q' is described with Crocco's sentitive time-lag (n-τ) hypothesis.[8] The basic idea is that the reactant material requires a finite amount of time τ to burn, and therefore, when a sudden change in flow condition is applied to the steady-state combustion, the process assumes its new condition only after the time lag τ. If we further assert that the reaction rate depends only on pressure and is proportional to p^n, then Q' can be modeled as

$$\frac{Q'(t)}{\bar{Q}} = n\frac{p_2'(0,t) - p_2'(0,t-\tau)}{\bar{p}_2} \tag{2.4.4}$$

where n is called the interaction index, being taken to be the overall order of chemical reaction. For the combustion of hydrocarbon fuel in air, n is between 1.7 to 2.2.[9] Equation (2.4.4) indicates that Q' vanishes if there is no time delay; the reactants entering the combustor burn immediately behind the dump plane, regardless of the flow condition. Physically, τ is attributed to the ignition delay and the turbulent mixing between unburned and burned gases, and can be crudely estimated by considering various time and length scales associated with turbulent eddy structure and chemical reaction.[10] It must be treated here as a phenomenological constant whose value can be determined only by global comparison of calculated results with experiments. The model of the combustion used here is too crude to produce a precise definition of τ in terms of fundamental processes.

Substitution of perturbed flow quantities at x=0 into (2.4.1-3) and rearrange-

ment of the results produces a transcendental equation for the complex frequency Ω,

$$\frac{\bar{\rho}_2}{\bar{\rho}_1}\left\{\bar{M}_1(P_1^+ - P_1^-) + (P_1^+ + P_1^-)\right\}$$

$$= \bar{M}_2(P_2^+ - P_2^-) + \left[1 - \frac{n\bar{Q}\bar{\rho}_2}{\bar{p}_2}(1 - e^{i\Omega\tau})\right](P_2^+ + P_2^-) + \frac{1}{\gamma - 1}S_2 \tag{2.4.5}$$

where

$$P_1^+ = \beta_s e^{2iK_1L_1} \tag{2.4.6}$$

$$P_1^- = 1 \tag{2.4.7}$$

$$S_2 = \frac{\alpha_2 - \alpha_1 - \beta_a(\alpha_1 - \alpha_2)e^{2iK_2L_2}}{\bar{M}_2 + \beta_a\bar{M}_2e^{2iK_2L_2} + 2\beta_e e^{iL_2(K_2 + \bar{M}_2K_2 + \frac{\Omega}{\bar{u}_2})}} \tag{2.4.8}$$

$$P_2^+ = \frac{1}{2}(\alpha_1 + \alpha_2 + \bar{M}_2S_2) \tag{2.4.9}$$

$$P_2^- = \frac{1}{2}(\alpha_1 - \alpha_2 - \bar{M}_2S_2) \tag{2.4.10}$$

and

$$\alpha_1 = [(1 + \bar{M}_1)P_1^+ - (1 - \bar{M}_1)P_1^-]\frac{\bar{a}_2}{\bar{a}_1}\frac{A_1}{A_2} - \bar{M}_2(P_1^+ + P_1^-) \tag{2.4.11}$$

$$\alpha_2 = P_1^+ + P_1^- \tag{2.4.12}$$

2.5 Discussion of Results

Calculations have been carried out to determine the acoustic modes that are excited in two research coaxial-dump ramjet engines having different combinations of inlet and combustor lengths.[2] The data characterizing a typical experiment are given in Table 2.1.

Table 2.1 Input parameters

length (engine A)	L_1 = 0.85 m	L_2 = 0.76 m
length (engine B)	L_1 = 0.85 m	L_2 = 0.57 m
area ratio	$\frac{A_2}{A_1} = 4.0$	
speed of sound	$\bar{a}_1$ = 426.7 m/s	$\bar{a}_2$ = 853.4 m/s
Mach number	$\bar{M}_1 = 0.4$	$\bar{M}_2 = 0.2$
specific heat ratio	$\gamma_1 = 1.38$	$\gamma_2 = 1.26$
chamber pressure	5.4 atm	
shock Mach number	$M_{1s} = 1.825$	

Table 2.2 summarizes the calculated frequencies and growth rates of oscillations, based on various models including pure acoustic and acoustic/entropy fluctuations. All these calculations provide reasonable solutions for the frequencies, but only the result for a combustion time lag τ=0.001 sec is physically realistic as it gives both positive and negative growth rates. Since stability can be determined by the energy flowing to and from the acoustic fields, this result indicates that the acoustic energy gained in the second mode oscillation is dissipated by the first mode oscillation through the energy exchange processes between modes. In fact, the second mode has been found to be dominant in most experiments.[2]

For a pure acoustic model containing no entropy fluctuation, the growth rates are always negative. The wave amplitude decays with time. This is a consequence of incomplete representation of the combustion processes. The acoustic energy gained from the combustion processes does not compensate the energy losses at the inlet shock and the exhaust nozzle. Hence, the waves appear to be stable. The same situation occurs for the model with no combustion time lag as it can not produce a non-zero fluctuation of energy, Q'.

TABLE 2.2 Measured and Calculated Frequencies and Growth Constants

Engine A (baseline combustor)		Engine B (short combustor)		Comments
$f_{measured}$ = 540 Hz		$f_{measured}$ = 190 Hz, 650 Hz		
$f_{calculated}$	$\alpha_{calculated}$	$f_{calculated}$	$\alpha_{calculated}$	
131	-54	140	-55	No entropy fluctuation included
595	-59	664	-60	
134	-56	141	-60	Entropy fluctuation included, τ = 0 sec
580	-58	669	-61	
139	-37	163	-41	Entropy fluctuation included, τ = 0.0005 sec
624	13	679	-9.8	
133	-24	160	-17	Entropy fluctuation included, τ = 0.001 sec
569	6	622	23.5	

Figure 2.5 shows the calculated and measured pressure and phase distributions of the second mode oscillations in the baseline engine A. Because the theory is linear, the amplitude contains an arbitrary multiplying constant whose value has been adjusted to provide reasonable comparison with experimental data. This mode is the first longitudinal mode of the combustor with a non-stationary standing wave in the inlet, and has been observed in the majority of tests. The acoustic field is driven by the pressure oscillations in the combustor and attenuated efficiently by the shock. The mode structure in the combustion chamber is similar to that for a half wave in a closed-closed organ pipe. A pressure node exists in the middle of the combustor across which a phase jump of nearly 180 degrees occurs. In the inlet section, the waveform is mainly affected by the mean flow and the shock. The influence of the former arises from the Doppler effect, which, together with the smaller speed of sound, causes a reduction of wavelength in comparison with the wave in the combustor. The phase distribution is almost linear because of the efficient absorption of the left-running wave by the shock, as explained in Section 2.2.

When a short combustor (engine B) is tested, the dominant oscillations occur at frequencies of 190 Hz and 650 Hz. Figure 2.6 shows the pressure and the phase distributions for the first mode oscillation. The acoustic field in the combustor is a bulk mode, giving a uniform phase distribution. Figure 2.7 shows the second mode shapes and phase distributions. In comparison with the oscillation in engine A, the frequency increases from 540 Hz to 660 Hz as a result of the shorter burner.

To further identify the mode structures and the controlling mechanisms, a parametric study of the influences of engine geometry on the second mode pressure oscillations is conducted, giving the result shown in Figure 2.8. The calculated frequencies are relatively insensitive to the changes in the inlet length, but decreases almost linearly with the combustor length. This is due to the half wave

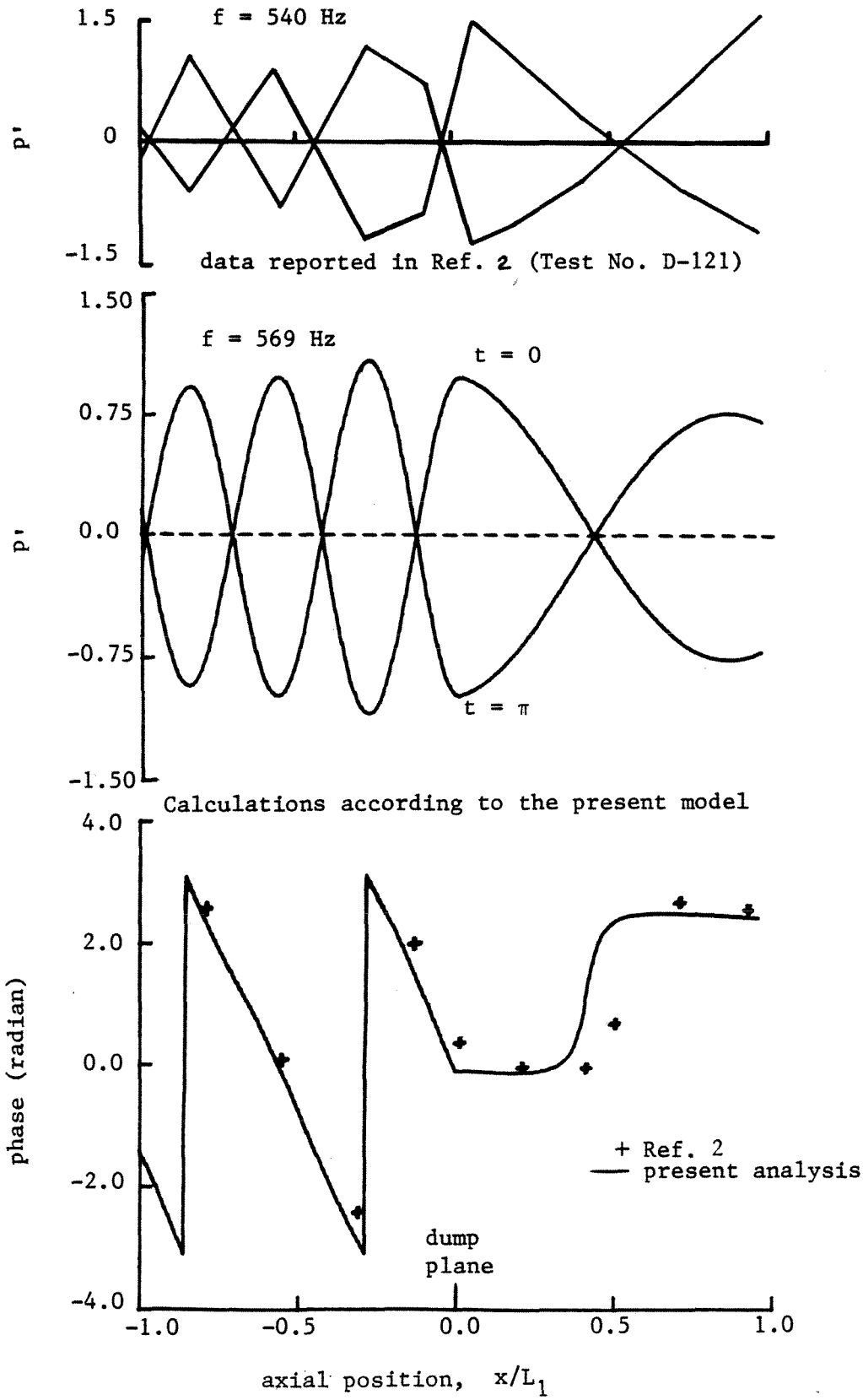

FIGURE 2.5. Measured and Calculated Acoustic Wave Amplitude and Phase Distributions (Baseline Combustor)

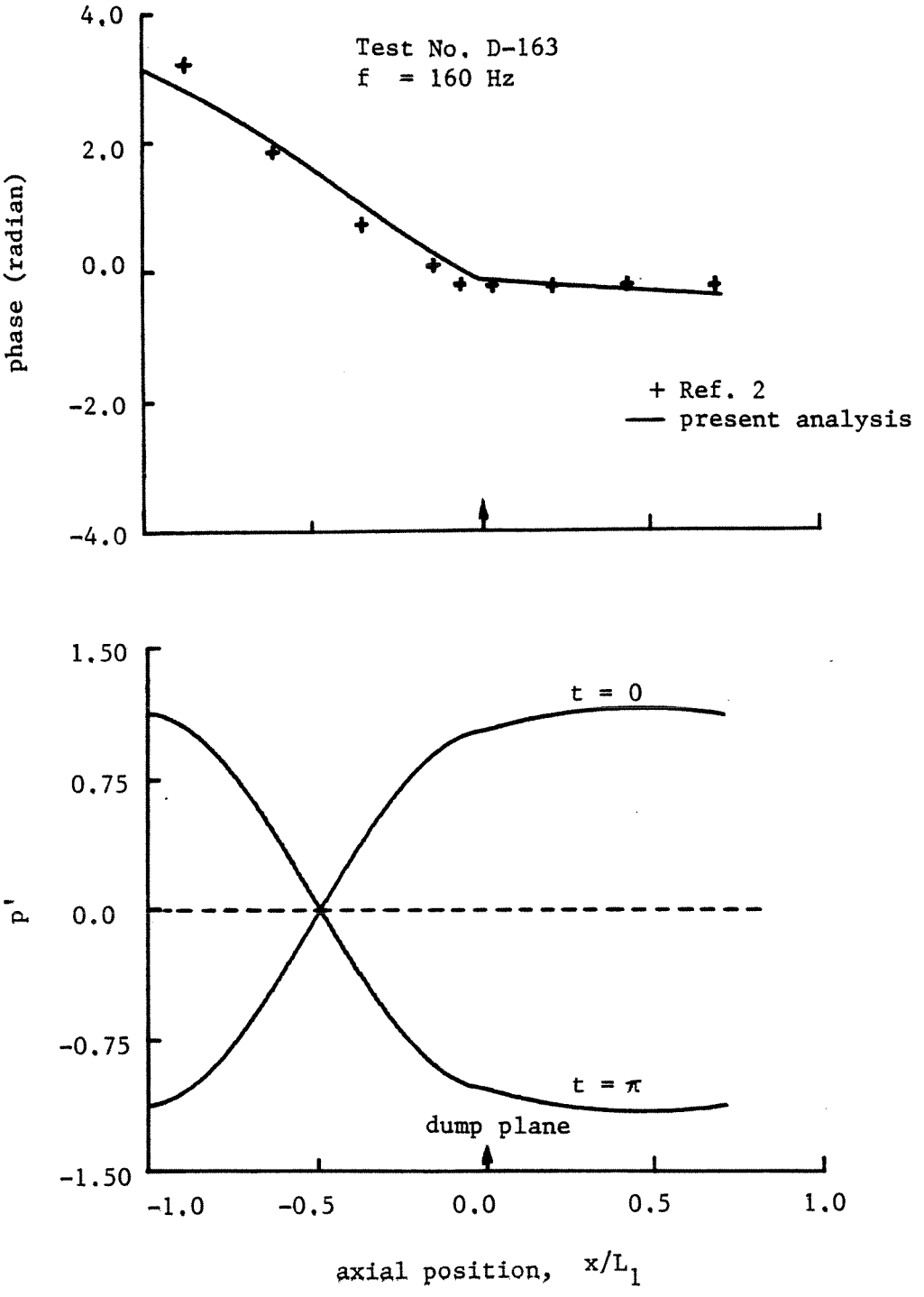

FIGURE 2.6. Measured and Calculated Acoustic Wave Amplitude and Phase Distributions (Short Combustor)

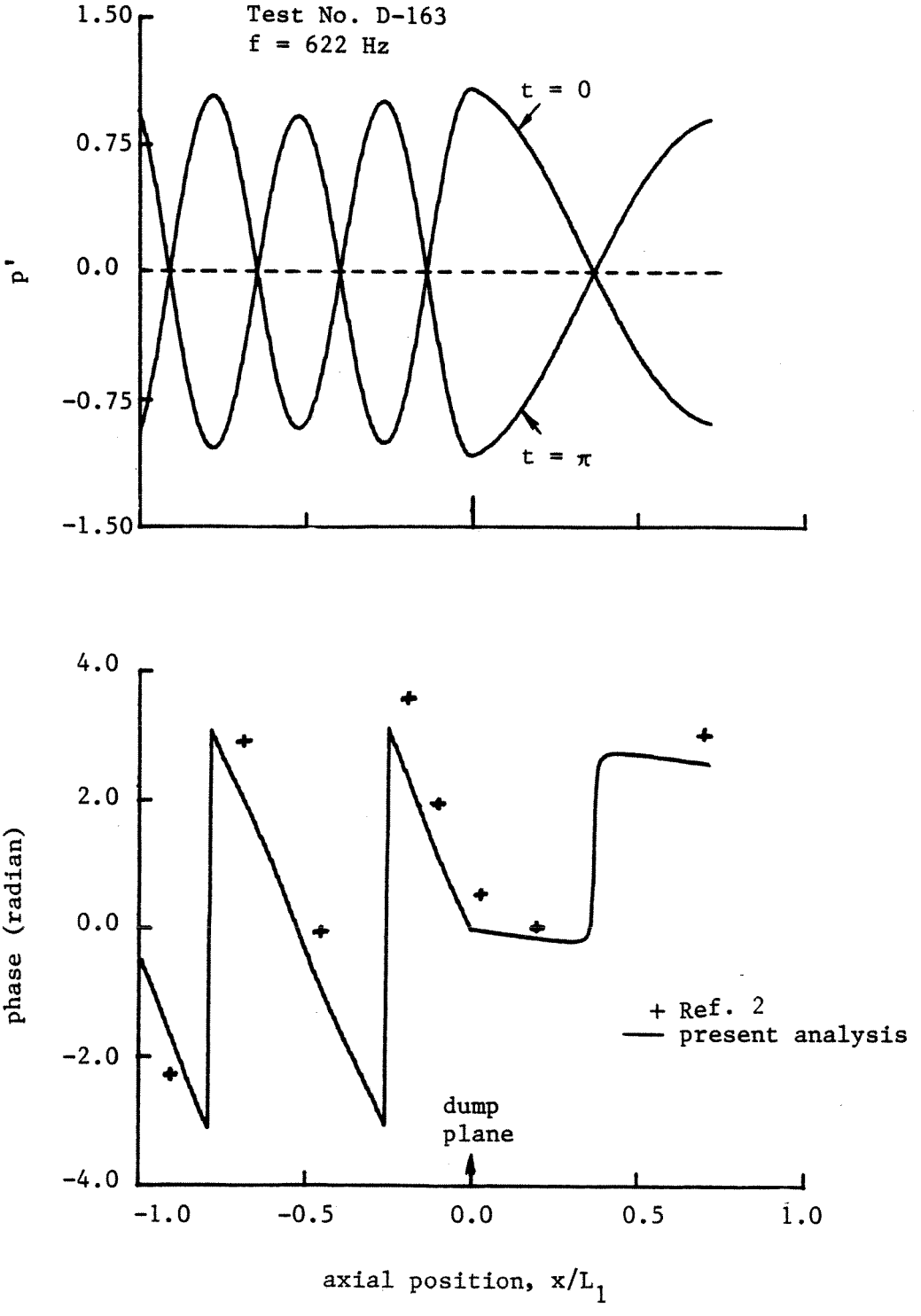

FIGURE 2.7. Measured and Calculated Acoustic Wave Amplitude and Phase Distributions (Short Combustor)

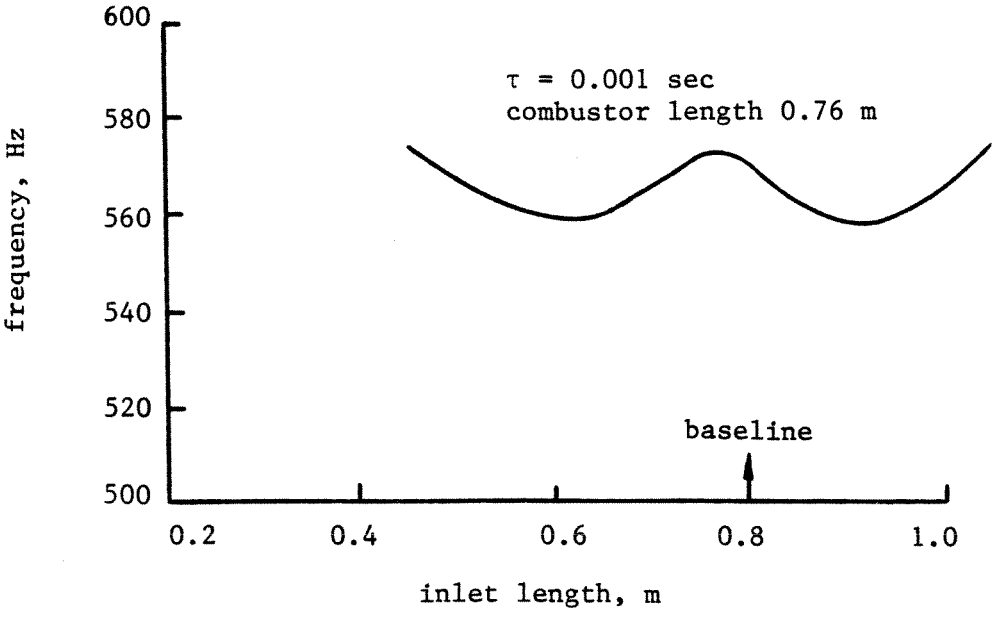

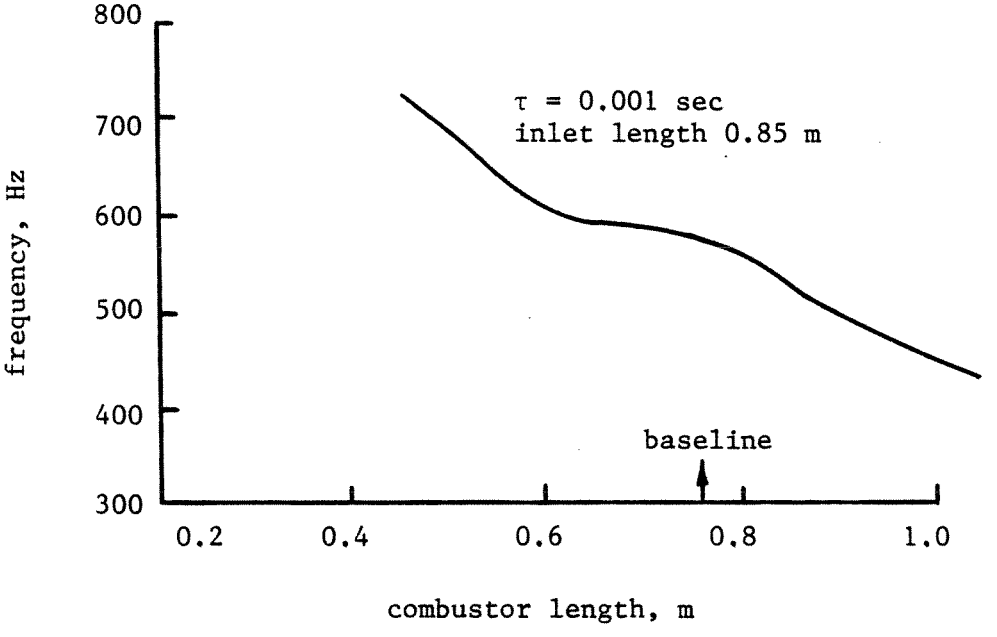

FIGURE 2.8. Dependence of the Second Mode Frequency on the Inlet and Combustor Lengths

structure in the combustion chamber and suggests that the unsteady motion in the engine is mainly determined by the flowfield in the combustor. The inlet flow plays a minor role since the shock absorbs effectively the left-running acoustic wave generated by the combustion. The contribution of the small-amplitude refected wave to the excitation of pressure oscillations is negligibly small in comparison with that of the combustor flow. The cause for the small hump in Figure 2.8a is not clear; it may be due to the interaction among the shock admittance function, the combustion time lag, and the engine geometry.

REFERENCES 2

1. Crump, J. E., Schadow, K. C., Blomshield, F.and Bicker, C. J., "Combustion Instability in a Research Dump Combustors: Pressure Oscillations," *18th JANNAF Combustion Meeting*, October 1982.

2. Crump, J. E., Schadow, K. C., Blomshield, F., Culick, F. E. C., and Yang, V., "Combustion Instability in Dump Combustors: Acoustic Mode Determinations," *19th JANNAF Combustion Meeting*, November 1982.

3. Kovasnay, L. S. G., 'Turbulence in Supersonic Flow," *Journal of the Aeronautical Sciences*, Vol.20, October 1953, pp.657-674.

4. Whitham, G. B., *Linear and Nonlinear Waves*, John Wiley and Sons, Inc., 1974.

5. Culick, F. E. C. and Rogers, T., 'The Response of Normal Shocks in Diffusers," *AIAA Journal*, Vol.21, October 1983, pp.1382-1390.

6. Marble, F. E. and Candel, S. M., "Acoustic Disturbance from Gas Non-Uniformities Convected through a Nozzle," *Journal of Sound and Vibration*, Vol.55, 1977, pp.225-243.

7. Shapiro, A. H., *The Dynamics and Thermodynamics of Compressible Fluid Flow*, Ronald Press, Inc., 1953.

8. Crocco, L. and Cheng, S. I., *Theory of Combustion Instability in Liquid Propellant Rocket Motors*, AGARD No.8, Butterworths Scientific Publications, 1956.

9. Kanury, A. M., *Introduction to Combustion Phenomena*, Gordon and Breach, Inc., 1977.

10. Yang, V., Private Communication with F. E. C. Culick, August 1983.

NOMENCLATURE 2

a	speed of sound
A	cross-sectional area of the engine
A_s	shock admittance function
c_p	constant pressure specific heat
K	modified complex wave number, defined by (2.1.14)
M	Mach number
p	pressure
Q	heat of combustion
s	entropy
t	time
T	temperature
u	velocity
x	position coordinate along the axis of the engine
α	growth constant
γ	ratio of specific heats
ω	frequency
Ω	complex frequency, $\Omega = \omega + i\alpha$
Ω_s	dimensionless frequency, defined by (2.2.6)
ρ	density

superscript

$(\bar{})$	average value
$(\ )'$	fluctuation

subscripts

1	value in the inlet
2	value in the combustor

Chapter 3

PRESSURE OSCILLATIONS IN TWO-DIMENSIONAL DUMP COMBUSTORS

In the last chapter, we presented an approximate linear analysis of pressure oscillations by assuming the mean flowfield uniform. While the treatment is appropriate for the inlet, situations are quite different for the combustor where the flow is highly non-uniform. There are strong gradients of density and temperature due to the energy release in the combustion zone. In addition, the recirculating flow immediately downstream of the dump plane complicates the velocity and pressure fields significantly. The purpose of this chapter is to develop an adequate model accommodating these matters within the low frequency range. We consider here only the case of two-dimensional flow.

The model of the flow is sketched in Figure 3.1, representing the experimental facility operated at the California Institute of Technology.[1] Premixed gaseous mixture of air and methane is supplied in a connected pipe facility and delivered to the dump combustor, which is formed by placing a rearward-facing step in the duct. In some cases, especially when the flow speed is small and the acoustic resonance occurs in the plenum chamber, large structure vortices with dimensions of the order of the step height were shed at the flame attachment point, distorting the flame front as they were swept downstream. Substantial longitudinal oscillations could thus arise due to the interaction between unsteady combustion and the acoustic field *upstream* of the flameholder. This mode of oscillation has also been reported in reference 2. To circumvent the problem, the plenum chamber is filled with acoustic damping material such as steel wool; the leftward acoustic wave transmitted into the chamber is effectively dissipated. Consequently, no regular shedding of vortices is observed and the wake behind the dump plane is stable in this sense.

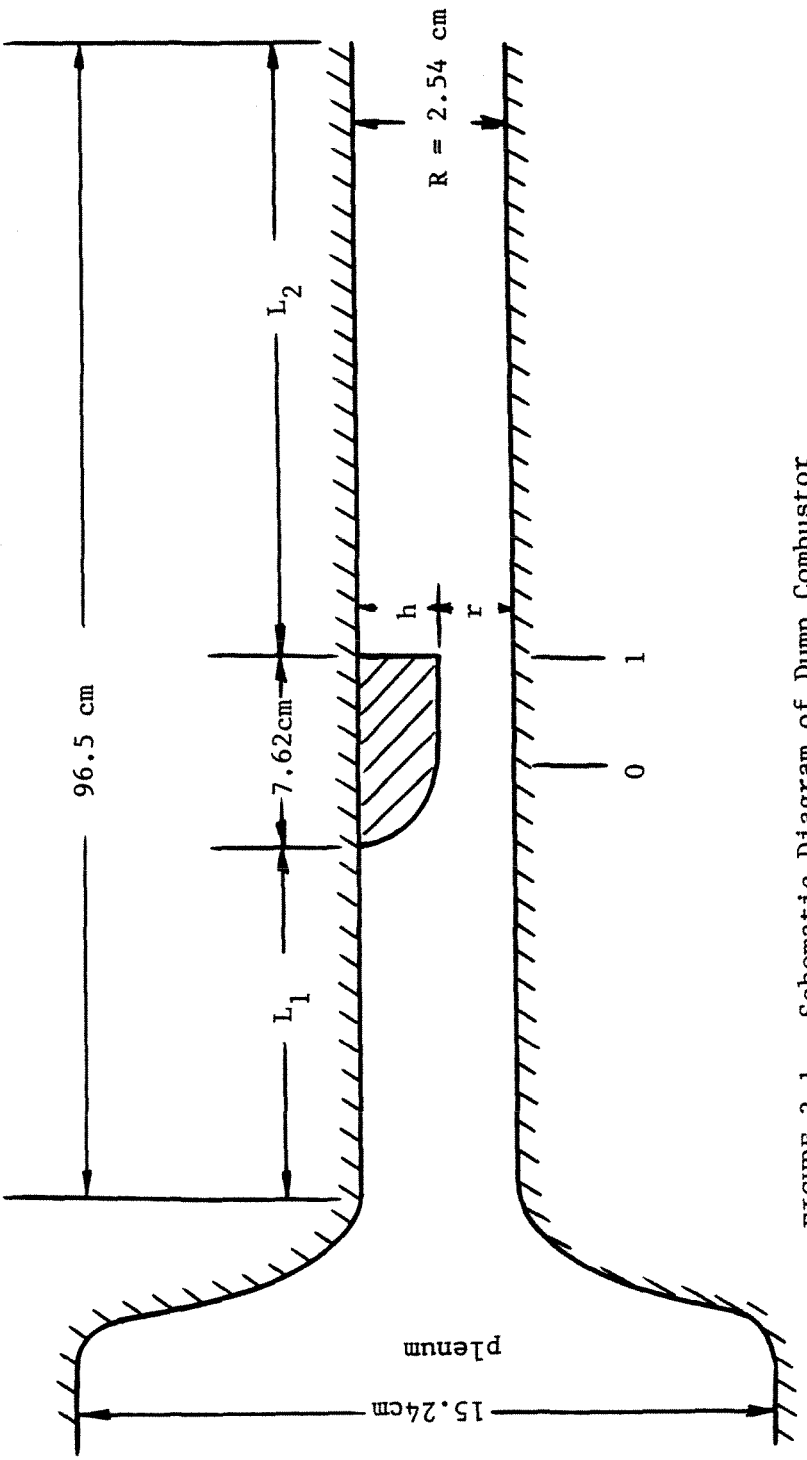

FIGURE 3.1. Schematic Diagram of Dump Combustor

For convenience of analysis, the oscillatory fields are constructed for three regions spanning the length of the device: the inlet duct (I), the combustion region from the dump plane to the end of the flame zone (II), and the length from the end of the flame zone to the exit plane (III). The formulation of the fields in regions I and III are relatively simple since the mean flows to a good approximation may be assumed uniform. The results obtained in Chapter 2 can be directly applied. The main issue is the combustor flow. It seems essential that the two-dimensional character of the mean flowfield be accounted for. Owing to the non-uniform geometry, and to the interactions with the mean flow, the acoustic field must also be two-dimensional. From experience with previous problems one might expect that there are modes of oscillation which have relatively small components of motion almost everywhere in planes transverse to the axis. Early observations and the initial analyses of ramjet combustors established that indeed the low frequency instabilities are basically longitudinal modes for the chamber and inlet. Accordingly, the analysis of unsteady motions described here treats plane one-dimensional oscillations with a two-dimensional mean flowfield.

The analysis is based on the integral formulation, being developed by integrating the conservation equations with respect to y-coordinate. Because the mean flow appears only in integrals, the consequent errors in its representation tend to be softened. Thus we can likely be satisfied with a cruder model than would be required, for example, to compute the combustion efficiency. The intent is to represent approximately the main feature of the pressure, velocity, and temperature fields. For low frequency oscillations, the flame front and the shear layer are collapsed to two infinitesimally thin sheets: flame and vortex sheets respectively. The flowfield in the combustion zone is thus decomposed into a flow of reactants, a region containing combustion products, and a recirculation zone, as shown in Figure 3.2. The three regions are then matched at these sheets by taking into account

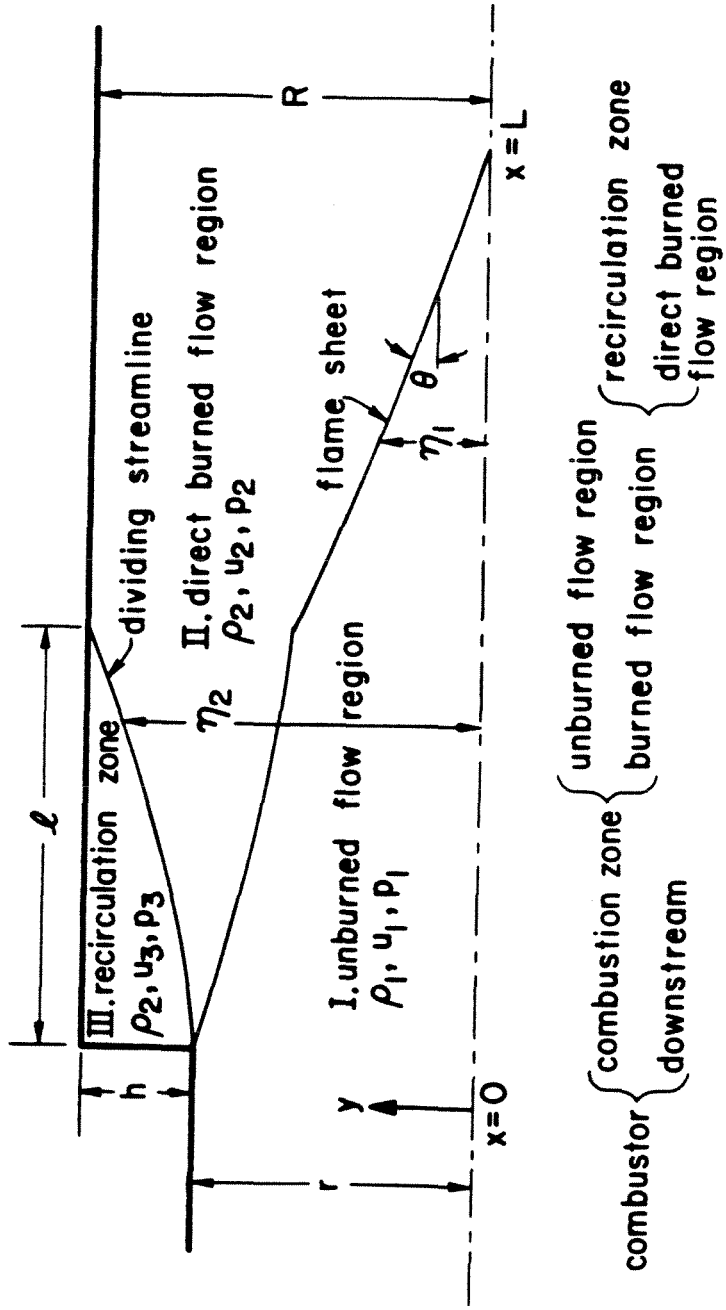

FIGURE 3.2. Flowfield in the Two-Dimensional Dump Combustor

kinematic and conservation relations. Determination of their shapes are part of the solution.

The unsteady flowfields are treated within linear analysis and approximated as quasi one-dimensional motions. The pressure waves are assumed to be planar everywhere in the engine, but the acoustic velocities are different in the unburned and burned flows due to the different acoustic characteristics. Treated in this way, the recirculating flow and the vortex sheet, or dividing streamline, are considered steady. The energy sustaining pressure oscillations is gained mainly from the interaction between the unsteady flowfields and the flame sheet. As a result of the periodic fluid dynamic stretching of the flame sheet, the rate of the combustible mixture entering the flame zone and the consequent energy release may oscillate as well. If this happens at the proper time and is positively correlated with the pressure fluctuation, a feedback loop is thus formed and the possibility for self-excited oscillation exists.

In the following sections, an integral scheme is first developed to analyze the flowfields in the combustion region. The model extends the previous analysis[3] of the unsteady flame spreading from a point flameholder and accommodates the recirculating flow and gas compressibility. Results can therefore be obtained for dump combustors. After the fields in the three regions have been treated, with appropriate matching conditions at the interfaces, the acoustic mode shapes and frequencies characterizing the linear oscillations in the entire device are determined. Calculations have shown favorable comparison with experimental data reported in reference 1.

3.1 Flow Field in the Combustion Zone

The flowfield in the combustion zone is first approximated by division into two

parts: the unburned and the burned regions, separated by a flame sheet, as shown in Figure 3.2. The flame sheet is an idealized treatment of the combustion processes. It is a surface of discontinuity on which the chemical reactions and rapid state variations take place. The flow speed tangential to the sheet is continuous, but the normal component suffers a step change due to the discontinuity of density. Although the model serves as an effective tool in the analysis of laminar flame propagation, application to turbulent flames is at best a crude approximation. Only those flows with turbulent scales much greater than flame thickness permit this application,[4] a case not relevant here. As far as the computation of the low frequency unsteady motions with flame propagations is concerned, the representation of the flame front by a thin sheet is justified since the sensitivity of combustion processes is mainly associated with fluid dynamic processes, rather than chemical kinetics, and the ratio of the oscillation wavelength to the flame thickness is large.

The sudden change in the cross sectional area at the dump plane produces recirculating flow which is bounded by a shear layer. The density and temperature fields of the recirculating flow are very close to those of the direct burned flow, but the mean velocity and pressure fields are greatly different.[5] There are strong reversing flows and nonuniformities of the pressure distributions in the recirculation zone. Therefore, it is convenient to treat the recirculating flow and the direct burned flow separately. In real flows, the shear layer entrains flow and continuous passage of hot combustion products into and out of the recirculation zone takes place. We ignore that process and assume that the shear layer is a sheet of tangential velocity discontinuity, represented by a dividing streamline here. Nevertheless, the model is expected to be valid when the acoustic wave length is long compared with the shear layer thickness.[6] For low frequency oscillations this criterion is met.

If we neglect viscous effects, the flow field in each region can be described by the following equations of continuity and momentum.

$$\frac{\partial \rho}{\partial t} + \frac{\partial}{\partial x}\rho u + \frac{\partial}{\partial y}\rho v = 0 \tag{3.1.1}$$

$$\frac{\partial}{\partial t}\rho u + \frac{\partial}{\partial x}\rho u^2 + \frac{\partial}{\partial y}\rho uv + \frac{\partial p}{\partial x} = 0 \tag{3.1.2}$$

$$\frac{\partial}{\partial t}\rho v + \frac{\partial}{\partial x}\rho uv + \frac{\partial}{\partial y}\rho v^2 + \frac{\partial p}{\partial y} = 0 \tag{3..1.3}$$

Since combustion is confined to the flame sheet, there is no mechanism producing entropy outside the sheet. The entropy is preserved following fluid elements in each region. As a result, the energy equation can be written in the form

$$\frac{\partial}{\partial t}\rho s + \frac{\partial}{\partial x}\rho us + \frac{\partial}{\partial y}\rho vs = 0 \tag{3.1.4}$$

3.1.1 **Matching Conditions**

The unburned and the direct burned flows are matched at the flame sheet using conservation and kinematic relations.[7] For two-dimensional flow, the kinematic relations are

$$\frac{\partial \eta_1}{\partial t} + u_1(x,\eta_1,t)\frac{\partial \eta_1}{\partial x} = v_1(x,\eta_1,t) - W_1 \sec\vartheta \tag{3.1.5}$$

$$\frac{\partial \eta_1}{\partial t} + u_2(x,\eta_1,t)\frac{\partial \eta_1}{\partial x} = v_2(x,\eta_1,t) - W_2 \sec\vartheta \tag{3.1.6}$$

where W_1 and W_2 are the normal flow velocities relative to the flame sheet on the upstream and downstream sides, and η_1 is the y-coordinate of the flame sheet. Note that η_1 depends on both time and space, taking into account the unsteady motion of the flame sheet. For steady motions, (3.1.5) and (3.1.6) contain no time-dependent terms and can be derived simply by considering the geometric relations among the flow velocities at the flame sheet.

Conservation laws are applied by considering the flow quantities relative to the flame sheet. The conservations of mass and momentum give

$$\rho_1 W_1 = \rho_2 W_2 \tag{3.1.7}$$

$$\rho_1 W_1^2 + p_1 = \rho_2 W_2^2 + p_2 \tag{3.1.8}$$

Since the pressure is continuous along the flame sheet, the tangential velocity component is preserved:

$$u_1(x,\eta_1,t)\cos\vartheta - v_1(x,\eta_1,t)\sin\vartheta = u_2(x,\eta_1,t)\cos\vartheta - v_2(x,\eta_1,t)\sin\vartheta \tag{3.1.9}$$

For most cases the changes in the kinetic energy and the pressure across the flame sheet may be ignored in comparison with the heat of combustion, ΔH. Hence, energy conservation requires

$$c_{p1}T_1 + \Delta H = c_{p2}T_2 \tag{3.1.10}$$

Rearrangement of the above equation for a perfect gas leads to

$$\frac{\rho_1}{\rho_2} = \left(1 + \frac{\Delta H}{c_{p1}T_1}\right)\frac{p_2}{p_1} \tag{3.1.11}$$

Equation (3.1.8) implies that the difference between p_2 and p_1 is of order of the square of the Mach number based upon the flame speed. Thus, it is satisfactory to neglect the pressure change in (3.1.11).

$$\beta_\rho \equiv \frac{\rho_1}{\rho_2} = 1 + \frac{\Delta H}{c_{p1}T_1} \tag{3.1.12}$$

Physically, the density jump due to the combustion produces volume sources along the flame sheet; their unsteady behavior is partly responsible for the pressure oscillations in the chamber.

Kinematic relations at the dividing streamline are obtained by considering its instantaneous motion. The results are

$$\frac{\partial \eta_2}{\partial t} + u_2(x,\eta_2,t)\frac{\partial \eta_2}{\partial x} = v_2(x,\eta_2,t) \tag{3.1.13}$$

$$\frac{\partial \eta_2}{\partial t} + u_3(x,\eta_2,t)\frac{\partial \eta_2}{\partial x} = v_3(x,\eta_2,t) \tag{3.1.14}$$

Because the dividing streamline is a streamline across which there is no flow but the tangential velocity is discontinuous, the only conservation relation available is continuity of pressure:

$$p_2(x,\eta_2,t) = p_3(x,\eta_2,t) \tag{3.1.15}$$

The flame speed W_1 is required to complete the matching conditions. For the turbulent flame spreading from a bluff body flameholder, it appears to depend on the local flow speed and to a less extent on the turbulence level in the unburned stream.[8,9] The influences of the fuel-air ratio, the gas temperature, and the properties of the fuel are relatively small. Therefore,

$$W_1 = \beta_f V_1 \approx \beta_f u_1(x,\eta_1,t) \tag{3.1.16}$$

where V_1 is the speed of the upstream flow and β_f is determined empirically.

3.1.2 Integral Formulation

To formulate the flowfield in terms of integral variables, conservation equations are integrated with respect to y over each region. We first treat the continuity equation for the unburned flow in the region 1.

$$\int_0^{\eta_1} \frac{\partial \rho_1}{\partial t} dy + \int_0^{\eta_1} \frac{\partial}{\partial x}\rho_1 u_1 dy + \int_0^{\eta_1} \frac{\partial}{\partial x}\rho_1 v_1 dy = 0$$

Integration by parts, with η_1 a function of axial position and time, gives

$$\frac{\partial}{\partial t}\int_0^{\eta_1} \rho_1 dy + \frac{\partial}{\partial x}\int_0^{\eta_1} \rho_1 u_1 dy - \rho_1 u_1(x,\eta_1,t)\frac{\partial \eta_1}{\partial x}$$

$$-\rho_1\frac{\partial\eta_1}{\partial t}+\rho_1 v_1(x,\eta_1,t)-\rho_1 v_1(x,0,t)=0$$

Application of the kinematic relation (3.1.5) at the flame sheet and the boundary condition at the wall gives the final result for the integral mass equation in region 1:

$$\frac{\partial}{\partial t}\int_0^{\eta_1}\rho_1 dy+\frac{\partial}{\partial x}\int_0^{\eta_1}\rho_1 u_1 dy+\rho_1 W_1\sec\vartheta=0 \tag{3.1.17}$$

A similar integration of the other conservation equations results in the following integral equations:

momentum equation (region 1)

$$\frac{\partial}{\partial t}\int_0^{\eta_1}\rho_1 u_1 dy+\frac{\partial}{\partial x}\int_0^{\eta_1}\rho_1 u_1^2 dy+\int_0^{\eta_1}\frac{\partial p_1}{\partial x}dy+\rho_1 u_1(x,\eta_1,t)W_1\sec\vartheta=0 \tag{3.1.18}$$

mass equation (region 2)

$$\frac{\partial}{\partial t}\int_{\eta_1}^{\eta_2}\rho_2 dy+\frac{\partial}{\partial x}\int_{\eta_1}^{\eta_2}\rho_2 u_2 dy-\rho_2 W_2\sec\vartheta=0 \tag{3.1.19}$$

momentum equation (region 2)

$$\frac{\partial}{\partial t}\int_{\eta_1}^{\eta_2}\rho_2 u_2 dy+\frac{\partial}{\partial x}\int_{\eta_1}^{\eta_2}\rho_2 u_2^2 dy+\int_{\eta_1}^{\eta_2}\frac{\partial p_2}{\partial x}dy-\rho_2 u_2(x,\eta_1,t)W_2\sec\vartheta=0 \tag{3.1.20}$$

mass equation (region 3)

$$\frac{\partial}{\partial t}\int_{\eta_2}^{R}\rho_3 dy+\frac{\partial}{\partial x}\int_{\eta_2}^{R}\rho_3 u_3 dy=0 \tag{3.1.21}$$

momentum equation (region 3)

$$\frac{\partial}{\partial t}\int_{\eta_2}^{R}\rho_3 u_3 dy+\frac{\partial}{\partial x}\int_{\eta_2}^{R}\rho_3 u_3^2 dy+\int_{\eta_2}^{R}\frac{\partial p_3}{\partial x}dy=0 \tag{3.1.22}$$

As discussed in Chapter 2, an entropy fluctuation may be generated at the flame front and carried downstream with the mean flow. Since the flows are isentropic in the region upstream of the flame sheet and in the recirculation zone, the only

entropy equation required is that for region 2,

$$\frac{\partial}{\partial t}\int_{\eta_1}^{\eta_2}\rho_2 s_2 dy + \frac{\partial}{\partial x}\int_{\eta_1}^{\eta_2}\rho_2 u_2 s_2 dy - \rho_2 s_2(x,\eta_1,t)W_2\sec\vartheta = 0 \qquad (3.1.23)$$

In this work, we consider an incompressible two-dimensional mean flowfield with quasi one-dimensional unsteady motions. Because the radii of curvature of streamlines are large except in the recirculation zone, the equation of motion in the vertical direction assures that the variations of pressure across regions 1 and 2 are negligible. Consequently, the mean pressures in these regions are assumed to be functions of x only. The dependent variables are written as sums of mean and fluctuating quantities.

region 1

$$\rho_1(x,y,t) = \bar{\rho}_1 + \rho_1'(x,t) \qquad (3.1.24a)$$

$$u_1(x,y,t) = \bar{u}_1(x,y) + u_1'(x,t) \qquad (3.1.24b)$$

$$p_1(x,y,t) = \bar{p}_1(x) + p_1'(x,t) \qquad (3.1.24c)$$

$$s_1(x,y,t) = \bar{s}_1 \qquad (3.1.24d)$$

region 2

$$\rho_2(x,y,t) = \bar{\rho}_2 + \rho_2'(x,t) \qquad (3.1.24e)$$

$$u_2(x,y,t) = \bar{u}_2(x,y) + u_2'(x,t) \qquad (3.1.24f)$$

$$p_2(x,y,t) = \bar{p}_2(x) + p_1'(x,t) \qquad (3.1.24g)$$

$$s_2(x,y,t) = \bar{s}_2 + s_2'(x,t) \qquad (3.1.24h)$$

region 3

$$\rho_3(x,y,t) = \bar{\rho}_2 + \rho_3'(x,t) \qquad (3.1.24i)$$

$$u_3(x,y,t) = \bar{u}_3(x,y) + u_2'(x,t) \tag{3.1.24j}$$

$$p_3(x,y,t) = \bar{p}_3(x,y) + p_1'(x,t) \tag{3.1.24k}$$

$$s_3(x,y,t) = \bar{s}_2 \tag{3.1.24l}$$

The unsteady pressure is assumed uniform in the transverse direction as a result of the small Mach number of the flame speed, but the velocities are different in the unburned and burned regions. We do not make the strictly one-dimensional approximations for the acoustic fields, i,e.,

$$u_1'(x,t) = u_2'(x,t), \text{ etc.}$$

The model has two advantanges. First, the difference between the acoustic characteristics of the unburned and burned flows is taken into account. Second, the unsteady motion of the flame sheet as well as its effect on the acoustic field can be accommodated. Note that the recirculating flow is assumed to be steady due to the one-dimensional approximation to the velocity fluctuations in regions 2 and 3.

3.1.3 Mean Flow Fields in the Combustion Zone

The mean flowfield must be known for analysis of the unsteady motions. We consider the mean recirculating flow first. The recirculation zone is treated as a closed region bounded by a dividing streamline. Because the inner boundary layer thickness is small in comparison with the width of the recirculation zone and the viscous and turbulent stresses decay rapidly away from the shear layer, the so-called frozen vorticity theory[10] is used. The vorticity distribution is assumed to be uniform, the diffusion of vorticity due to viscosity and turbulence being ignored. The representation of the recirculating flow by a flow of constant vorticity with slip at the boundary has been found to be adequate. For example, Smith[11] considered such a representation for the flow in the region of the trailing edge of an aerofoil.

Taulbee and Robertson[12] used it to study the turbulent separation bubble ahead of a step. The model provided good agreement with experiments in all cases.

With the introduction of the stream function ψ, the equation of motion for the mean recirculating flow can be written in the following form:

$$\nabla^2\psi = -\omega_0, \quad \psi = 0 \text{ along the boundary} \tag{3.1.25}$$

where ω_0 is the constant vorticity, treated here as an empirical constant to be specified. The mean velocity and pressure fields are then obtained from the definition of the stream function and the preservation of total pressure along the streamline.

$$\bar{u}_3(x,y) = \frac{\partial\psi}{\partial y}; \quad \bar{v}_3(x,y) = -\frac{\partial\psi}{\partial x} \tag{3.1.26a}$$

$$\bar{p}_3 + \frac{1}{2}\bar{\rho}_2\bar{V}_3^2 = \text{constant} \tag{3.1.26b}$$

Legitimately, equation (3.1.25) can be solved either numerically or analytically. Both methods have been used, but the latter seems to be much more promising. The numerical technique using the successive over-relaxation (SOR) method[13] to solve the finite difference approximation encounters serious difficulties in the vicinities of the flow separating and reattaching points where strong velocity gradients exist. Unless very fine computational grids are used, the scheme may produce inaccurate results and sometimes becomes unstable. In addition, the rate of numerical convergence is usually slow. Because of these deficiencies, we resort to analytical methods here. The domain of concern is mapped conformally to a unit disk in which a closed-form solution to (3.1.25) is available. A detailed description of the analysis is given in Appendix 3A.

The integral conservation equations for the mean flowfields in regions 1 and 2 are obtained by considering the time invariant part of (3.1.17-20). Thus, we have

steady mass equation (region 1)

$$\frac{d}{dx}[\hat{u}_1\bar{\eta}_1] + W_1\sec\bar{\vartheta} = 0 \tag{3.1.27}$$

steady momentum equation (region 1)

$$\frac{d}{dx}[\hat{u}_1^2\bar{\eta}_1] + \frac{\bar{\eta}_1}{\bar{\rho}_1}\frac{dp_1}{dx} + \bar{u}_1(x,\bar{\eta}_1)W_1\sec\bar{\vartheta} = 0 \tag{3.1.28}$$

steady mass equation (region 2)

$$\frac{d}{dx}[\hat{u}_2(\bar{\eta}_2 - \bar{\eta}_1)] - W_2\sec\bar{\vartheta} = 0 \tag{3.1.29}$$

steady momentum equation (region 2)

$$\frac{d}{dx}[\hat{u}_2^2(\bar{\eta}_2 - \bar{\eta}_1)] + \frac{(\bar{\eta}_2 - \bar{\eta}_1)}{\bar{\rho}_2}\frac{d\bar{p}_2}{dx} - \bar{u}_2(x,\bar{\eta}_1)W_2\sec\bar{\vartheta} = 0 \tag{3.1.30}$$

where $\hat{u}_1$ and $\hat{u}_2$ are the average axial velocities defined as

$$\hat{u}_1 = \frac{1}{\bar{\eta}_1}\int_0^{\bar{\eta}_1}\bar{u}_1(x,y)dy,$$

$$\hat{u}_2 = \frac{1}{\bar{\eta}_2 - \bar{\eta}_1}\int_{\bar{\eta}_1}^{\bar{\eta}_2}\bar{u}_2(x,y)dy$$

In the derivation of (3.1.27-30), the following two conventional assumptions were made, similar to those used in shallow water wave calculations.

$$\int_0^{\bar{\eta}_1}[\bar{u}_1(x,y) - \hat{u}_1]^2dy = 0,$$

$$\int_{\bar{\eta}_1}^{\bar{\eta}_2}[\bar{u}_2(x,y) - \hat{u}_2]^2dy = 0,$$

Notice that the momentum integral equations explicitly involve the local velocity components at the flame sheet, $\bar{u}_1(x,\bar{\eta}_1)$ and $\bar{u}_2(x,\bar{\eta}_1)$. To complete the theoretical formulation, they must be determined in terms of the flame height $\bar{\eta}_1$ and the integral flow variables. The following remarks describe a simple independent

analysis of the flowfield in region 1, providing the necessary information.

Since the flow upstream of the flame sheet is inviscid and irrotational, the velocity potential satisfies the Laplace equation.

$$\nabla^2 \varphi = 0, \tag{3.1.31}$$

subject to the proper boundary conditions. Solution of the above equation may be written in the following form.

$$\varphi = u_{in}x + \sum_{m=1}^{m=\infty} A_m e^{\frac{m\pi}{r}x} \cos\left(\frac{m\pi}{r}y\right) \tag{3.1.32}$$

where u_{in} is the inlet flow velocity in the flat section of the flameholder (position 0 in Figure 3.1), and A_m's are constants to be calculated from the boundary conditions at the flame sheet. As a first approximation we shall account for the first term in the series only. This term is assumed to represent the general characteristics of the unburned flow to a sufficiently good approximation.[14] Thus, an equation relating the local velocities at the flame sheet is obtained from (3.1.32):

$$\frac{\bar{v}_1(x,\bar{\eta}_1)}{\bar{u}_1(x,\bar{\eta}_1) - u_{in}} = -\tan\left(\frac{\pi}{r}\bar{\eta}_1\right) \tag{3.1.33}$$

Combination of (3.1.33) with (3.1.5), (3.1.6), and (3.1.9) gives the expressions for $\bar{u}_1(x,\bar{\eta}_1)$ and $\bar{u}_2(x,\bar{\eta}_1)$.

$$\bar{u}_1(x,\bar{\eta}_1) = \frac{u_{in}\tan\left(\frac{\pi}{r}\bar{\eta}_1\right) - W_1\sec\bar{\vartheta}}{\frac{d\bar{\eta}_1}{dx} + \tan\left(\frac{\pi}{r}\bar{\eta}_1\right)} \tag{3.1.34}$$

$$\bar{u}_2(x,\bar{\eta}_1) = \frac{u_{in}\tan\left(\frac{\pi}{r}\bar{\eta}_1\right) - W_1\sec\bar{\vartheta}}{\frac{d\bar{\eta}_1}{dx} + \tan\left(\frac{\pi}{r}\bar{\eta}_1\right)} + W_1(\nu - 1)\sin\bar{\vartheta} \tag{3.1.35}$$

The theoretical model for the mean flow fields is completed by substituting the above two equations into the integral momentum equations.

The overall calculation using the integral scheme based upon iteration procedures proceeds as follows. We first assume a dividing streamline shape and solve the Poisson equation (3.1.25) and (3.1.26a) for the velocity field in the recirculation zone. The pressure distribution along the dividing streamline is calculated according to the Bernoulli equation (3.26b). With the result available as a known condition, the integral scheme governing the flowfields in the unburned and the direct burned regions is carried out to the end of the recirculation zone. Determination of the shapes of the dividing streamline and flame sheet is part of the solution obtained. Another calculation of the recirculating flow continues, using the new dividing streamline shape, and the whole procedure is repeated. The iterative computation halts when the solutions become convergent, the changes in the dividing streamline shape from step to step being small. The integral scheme is then performed to the end of the flame sheet to complete the solution.

Numerical calculations have been carried out for the mean flowfields in two dump combustors, referred to as combustors A and B here. They have the same inlet systems, but with step heights being one half and three quarters of the duct height respectively. The data characterizing a typical experiment reported in reference 1 is given in Table 3.1.

Table 3.1. Computer program input variables

u_{in}=71.32 m/s	p_{in}=101325 N/m^2
ρ_{in}=1.24 Kg/m^3	ω_0=100 1/s
T_{in}=283 K	a_{in}=337 m/s
L_1=0.559 m	L_2=0.406 m
β_ρ=4.94	β_f=0.05

Figure 3.3 summarizes the various distributions in the unburned flow in combustor A. The pressure variation upstream of the reattachment points is dominated by the recirculating flow. The effect of combustion appears in the determination of the flame and the dividing streamline shapes. For positions downstream the combustion plays a decisive role. As a consequence of the favorable pressure gradient generated by the combustion, the flow accelerates rapidly to the end of the flame zone. A kink, corresponding to the reattachment point, is observed on the flame sheet. The slope of the sheet gradually decreases near the kink, then grows after that point. This can be interpreted by appeal to the momentum balance. Because the pressure gradient tends to be small in the reattaching region, the flame shape must become flatter in order to reduce the momentum influx into the burned flow region.

Figure 3.4 shows the shapes of the dividing streamline and flame sheet for different cases in combustor B. These shapes are determined primarily by the flame speed parameter β_f and the density ratio across the flame, β_ρ, although the vortex strength affects the velocity field in the recirculation zone significantly. Because of the small radius of curvature of the dividing streamline caused by high vorticity, the length of the recirculation zone decreases as the vorticity ω_0 increases. The influences of the flame speed and the density ratio on the dividing streamline shape can be explained as follows. The higher flame speed, or the higher density ratio, usually implies the greater momentum influx into the direct burned region where the pressure field is mostly determined by the recirculating flow. For a given vortex strength this in turn produces a steeper dividing streamline to balance the momentum. Figure 3.5 shows the tangential velocity distributions along the dividing streamline. Obviously, they depend greatly on the vortex strength ω_0.

In the development of the integral scheme, we encountered a closure problem, which was then solved by proposing a simple independent equation (3.1.33) to

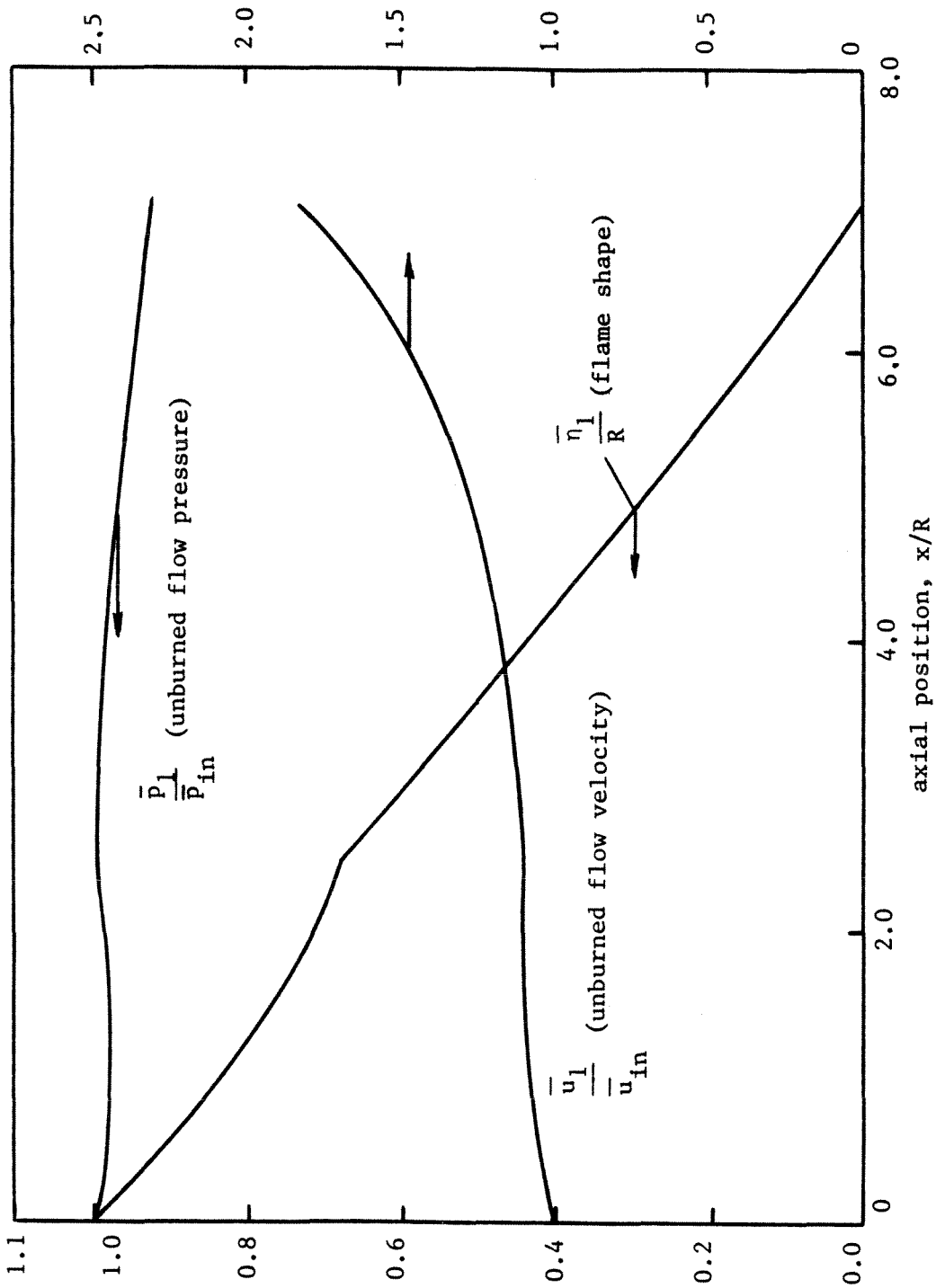

FIGURE 3.3. Distributions of Mean Flow Variables (Combustor A)

formulate the local flow velocities at the flame sheet. A similar difficulty was found by Subbaiah[15] in his study of the nonsteady behavior of a flame stabilized by a flame holder at the center of a two-dimensional duct. He carried out a more thorough analysis of the irrotational flow field upstream of the flame to provide the necessary conditions for the completeness of the model. In order to check the validity of the present work, specifically equation (3.1.33), we apply our model to the problem dealt with in reference 15 and use exactly the same input parameters. For this comparison, the recirculating flow immediately behind the flame holder is not accounted for. Figure 3.6 shows that the agreement is reasonably good.

3.1.4 Unsteady Flow Fields in the Combustion Zone

The unsteady flowfield in the combustion zone is formulated by considering the time-dependent counterpart to the steady analysis of the integral relations. It is treated within quasi one-dimensional linear oscillation. With the proposed decompositions of the flow variables and consideration of the first order terms only, the mass integral equation for the unburned flow in region I becomes

$$\frac{\partial}{\partial t}\left[\int_0^{\bar{\eta}_1}\rho_1'dy + \int_{\bar{\eta}_1}^{\bar{\eta}_1+\eta_1'}\bar{\rho}_1 dy\right] + \frac{\partial}{\partial x}\left[\int_0^{\bar{\eta}_1}(\bar{\rho}_1 u_1' + \rho_1'\bar{u}_1)dy + \int_{\bar{\eta}_1}^{\bar{\eta}_1+\eta_1'}\bar{\rho}_1\bar{u}_1 dy\right]$$

$$+ \rho_1' W_1 \sec\bar{\vartheta} - \bar{\rho}_1 W_1 \frac{\sin\bar{\vartheta}}{\cos^2\bar{\vartheta}}\frac{\partial\eta_1'}{\partial x} = 0$$

Rearrangement of the above equation yields

$$\frac{\partial}{\partial t}\left[\bar{\rho}_1\eta_1' + \rho_1'\bar{\eta}_1\right] + \frac{\partial}{\partial x}\left[\bar{\rho}_1\bar{u}_1(x,\bar{\eta}_1)\eta_1' + \rho_1'\hat{u}_1\bar{\eta}_1 + \bar{\rho}_1 u_1'\bar{\eta}_1\right]$$

$$+ \rho_1' W_1 \sec\bar{\vartheta} - \bar{\rho}_1 W_1 \frac{\sin\bar{\vartheta}}{\cos^2\bar{\vartheta}}\frac{\partial\eta_1'}{\partial x} = 0 \qquad (3.1.36)$$

Similar manipulations of the other integral formulas produce a system of equations governing the unsteady flow field:

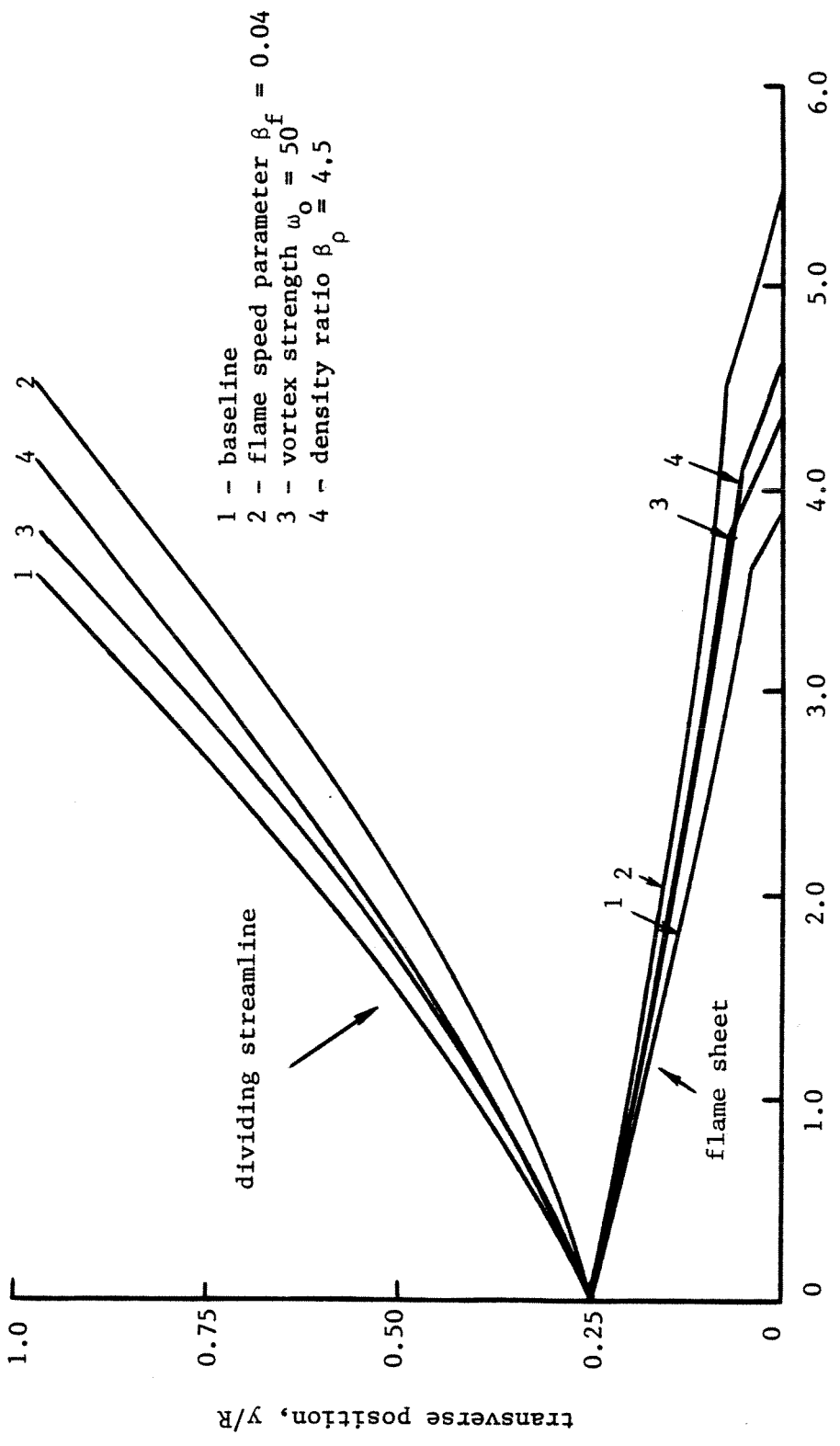

FIGURE 3.4. Shapes of Mean Dividing Streamline and Flame Sheet for Various Cases (Combustor B)

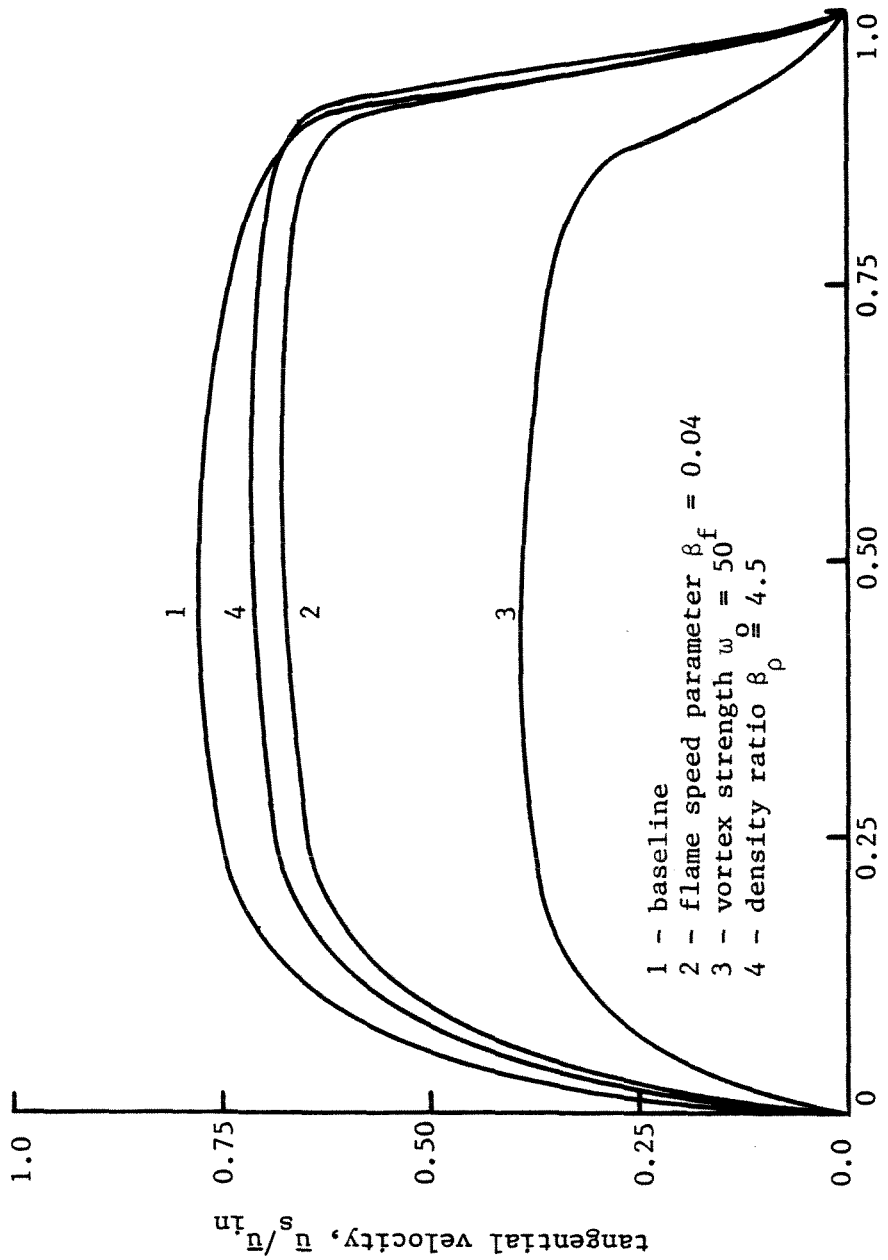

FIGURE 3.5. Distributions of Tangential Velocity along the Dividing Streamline

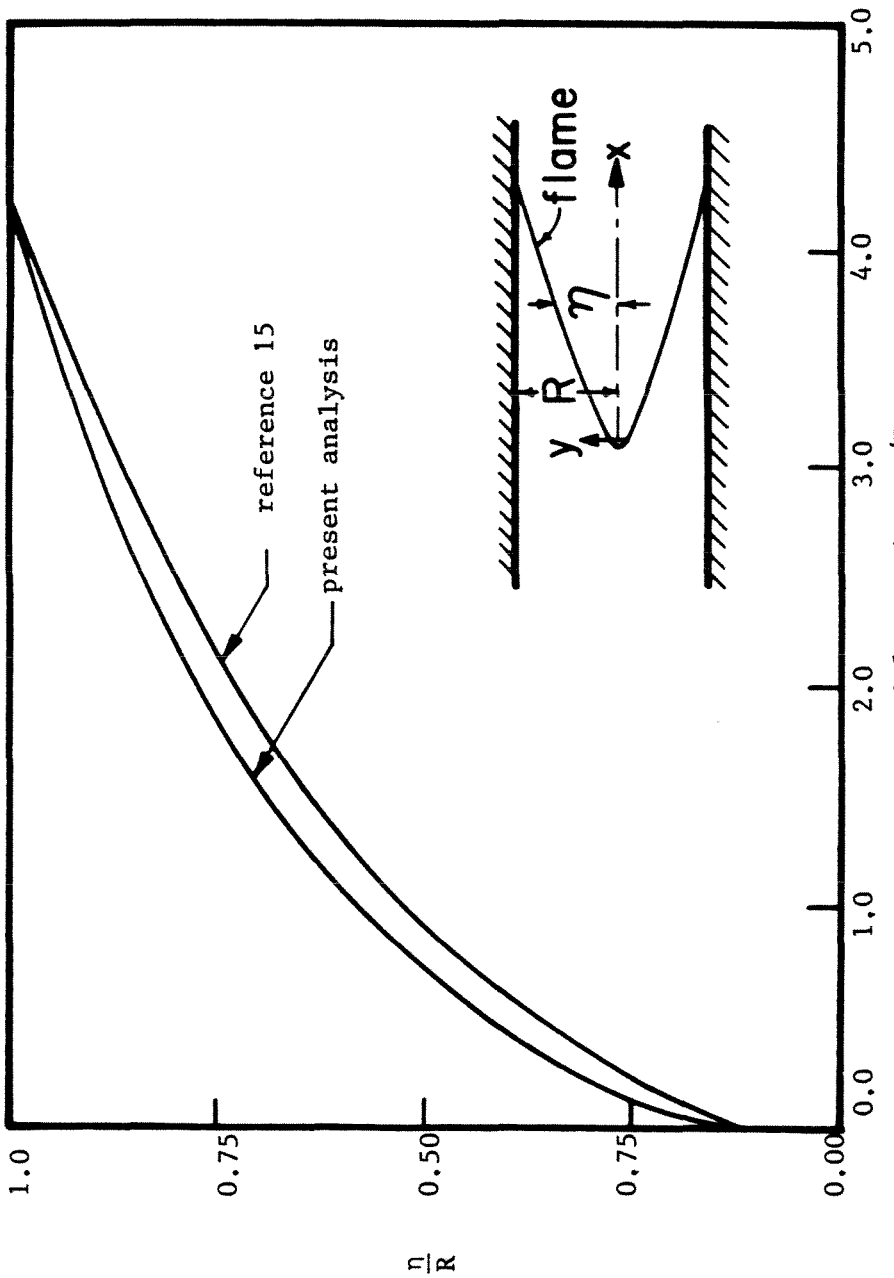

FIGURE 3.6. Steady Flame Sheets in a Two-Dimensional Duct

momentum equation (region 1)

$$\frac{\partial}{\partial t}[\bar{\rho}_1\bar{u}_1(x,\bar{\eta}_1)\eta_1' + \rho_1'\bar{\eta}_1 + \bar{\rho}_1 u_1'\eta_1] + \frac{\partial}{\partial x}[\bar{\rho}_1\bar{u}_1^2(x,\bar{\eta}_1)\eta_1' + \rho_1'\bar{\eta}_1\hat{u}_1^2$$

$$+ 2\bar{\rho}_1\hat{u}_1\bar{\eta}_1 u_1'] + \rho_1'\bar{u}_1(x,\bar{\eta}_1)W_1\sec\bar{\vartheta} + \bar{\rho}_1 u_1' W_1\sec\bar{\vartheta}$$

$$-\bar{\rho}_1\bar{u}_1(x,\bar{\eta}_1)W_1\frac{\sin\bar{\vartheta}}{\cos^2\bar{\vartheta}}\frac{\partial\eta_1'}{\partial x} + \bar{\eta}_1\frac{\partial p_1'}{\partial x} + \eta_1'\frac{\partial\bar{p}_1}{\partial x} = 0 \qquad (3.1.37)$$

mass equation (regions 2 and 3)

$$\frac{\partial}{\partial t}[\rho_3'(R-\eta_1') - \bar{\rho}_2\eta_1'] + \frac{\partial}{\partial x}[\bar{\rho}_2 u_2'(R-\bar{\eta}_1) + \rho_2'\hat{u}_2(\bar{\eta}_2-\bar{\eta}_1) - \bar{\rho}_2\bar{u}_2(x,\bar{\eta}_1)\eta_1']$$

$$-\rho_2' W_2\sec\bar{\vartheta} + \bar{\rho}_2 W_2\frac{\sin\bar{\vartheta}}{\cos^2\bar{\vartheta}}\frac{\partial\eta_1'}{\partial x} = 0 \qquad (3.1.38)$$

momentum equation (regions 2 and 3)

$$\frac{\partial}{\partial t}[\bar{\rho}_2 u_2'(R-\bar{\eta}_1) + \rho_2'\hat{u}_2(\bar{\eta}_2-\bar{\eta}_1) - \bar{\rho}_2\bar{u}_2(x,\bar{\eta}_1)\eta_1'] + \frac{\partial}{\partial x}[\rho_2'\hat{u}_2^2(\bar{\eta}_2-\bar{\eta}_1)$$

$$+ \rho_3'\int_{\bar{\eta}_2}^{R}\bar{u}_3^2 dy + 2\bar{\rho}_2 u_2'\hat{u}_2(\bar{\eta}_2-\bar{\eta}_1) - \bar{\rho}_2\bar{u}_2^2(x,\bar{\eta}_2)\eta_1'] - \rho_2' W_2\bar{u}_2(x,\bar{\eta}_1)\sec\bar{\vartheta}$$

$$-\bar{\rho}_2 u_2' W_2\sec\bar{\vartheta} + \bar{\rho}_2\bar{u}_2(x,\bar{\eta}_1)W_2\frac{\sin\bar{\vartheta}}{\cos^2\bar{\vartheta}}\frac{\partial\eta_1'}{\partial x} + (R-\bar{\eta}_1)\frac{\partial p_2'}{\partial x} - \eta_1'\frac{\partial\bar{p}_2}{\partial x} = 0 \qquad (3.1.39)$$

entropy equation (region 2)

$$\frac{\partial}{\partial t}[\bar{\rho}_2 s_2'(\bar{\eta}_2-\bar{\eta}_1)] + \frac{\partial}{\partial x}[\bar{\rho}_2\hat{u}_2(\bar{\eta}_2-\bar{\eta}_1)s_2'] - \bar{\rho}_2 W_2 s_2'(x,\bar{\eta}_1,t)\sec\bar{\vartheta} = 0 \qquad (3.1.40)$$

As a result of oscillations of flow properties at the flame sheet, entropy fluctuations may be generated and convected downstream. Consequently, the density disturbance in region 2 contains contributions from both the pressure and entropy fluctuations.

$$\frac{\rho_2'}{\bar{\rho}_2} = \frac{1}{\gamma}\frac{p_2'}{\bar{p}_2} - \frac{s_2'}{c_{p_2}} \tag{3.1.41}$$

In regions 1 and 3, the flows are isentropic; the oscillatory density fields are related to their pressure fields through the isentropic relations.

$$\rho_1' = p_1'/\bar{a}_1^2; \quad \rho_3' = p_2'/\bar{a}_2^2 \tag{3.1.42}$$

Thus, the formulation for the linear oscillatory fields is completed. In summary, there are five integral equations (3.1.36-40) for five unknowns u_1', u_2', p_1', η_1', and s_2'. For harmonic motions, the time- and the spatial-dependent parts of each flow variables are separated.

$$q'(x,t) = \tilde{q}(x)e^{-i\Omega t} \tag{3.1.43}$$

where q' denotes the unsteady flow variable. Substitution of (3.1.43) into the integral equations produces a system of ordinary differential equations with complex coefficients.

3.2 Acoustic Field in the Inlet

The analysis of the inlet is identical to that in Chapter 2. The acoustic field consists of two simple plane waves. One is driven by the pressure oscillations in the combustor and propagates upstream, and the other is reflected at the entrance and propagates downstream. Appropriate equations governing the acoustic pressure and velocity fields are

$$p_1' = [\beta_p e^{iK_1(2L_1 + x)} + e^{-iK_1 x}]\, e^{-i(\Omega t + M_1 K_1 x)} \tag{3.2.1}$$

$$u_1' = \frac{1}{\bar{\rho}_1 \bar{a}_1}[\beta_p e^{iK_1(2L_1 + x)} - e^{-iK_1 x}]\, e^{-i(\Omega t + M_1 K_1 x)} \tag{3.2.2}$$

where β_p is the acoustic reflection coefficient at the entrance ($x=-L_1$), and K_1 is the modified complex wave number.

$$K_1 = \frac{k_1}{1-\bar{M}_1^2} = \frac{\Omega/\bar{a}_1}{1-\bar{M}_1^2} = \frac{(\omega + i\alpha)/\bar{a}_1}{1-\bar{M}_1^2} \tag{3.2.3}$$

If we assume that the transition section from the plenum to the inlet is acoustically compact and the plenum serves as an acoustic energy absorber, to a good approximation, β_p=-1. The entrance is essentially an acoustic pressure node.

3.3 Acoustic Field Downstream of the Combustion Zone

Physically, this region contains the completely burned gas flow, ranging from the end of the flame sheet (x=L) to the exit plane ($x=L_2$). The mathematical treatment of the oscillatory fields in this region are similar to those in the inlet section except for the different mean flowfield and the presence of an entropy wave due to unsteady combustion. Since the duct is fully open at the exit, the incident pressure wave is perfectly reflected with phase difference 180 degrees. No contribution to the reflected pressure wave is made from the entropy fluctuation. The equations for the unsteady motions are

$$p_2' = P_2^+[e^{iK_2x} - e^{iK(2L_2 - x)}]\, e^{-i(\Omega t + \bar{M}_2K_2x)} \tag{3.3.1}$$

$$u_2' = \frac{P_2^+}{\bar{\rho}_2\bar{a}_2}[e^{iK_2x} + e^{iK(2L_2 - x)}]\, e^{-i(\Omega t + \bar{M}_2K_2x)} \tag{3.3.2}$$

where P_2^+ is the amplitude of the right-running wave and K_2 is defined as

$$K_2 = \frac{k_2}{1 - \bar{M}_2^2} = \frac{\Omega/\bar{a}_2}{1 - \bar{M}_2^2} = \frac{(\omega + i\alpha)/\bar{a}_2}{1 - \bar{M}_2^2} \tag{3.3.3}$$

The complex wave numbers K_2 differs from K_1 because the speeds of sound are different in the two regions.

3.4 Acoustic Field in the Entire Engine

The acoustic field in the combustion zone must be coupled to the fields upstream

of the dump plane and downstream of the end of the flame sheet. For linear problems this procedure eventually produces a transcendental equation for the complex wave number characterizing the acoustic field in the entire engine. The coupling is expressed by requiring that the acoustic pressure and mass flux be continuous.

For low frequency oscillations, the flameholder is acoustically compact. The boundary condition for the unburned flow at the dump plane (x=0) can be specified from (3.2.1-2).

$$p_1'(0,t) = [\beta_p e^{2iK_1L_1} + 1]\, e^{-i\Omega t} \tag{3.4.1}$$

$$u_1'(0,t) = \frac{1}{\bar{\rho}_1\bar{a}_1}\left(\frac{R}{r}\right)[\beta_p e^{2iK_1L_1} - 1]e^{-i\Omega t} \tag{3.4.2}$$

The flame sheet is assumed to be attached to the edge of the step. Thus,

$$\eta_1'(0,t) = 0. \tag{3.4.3}$$

Since the oscillatory velocity vanishes at the rigid wall,

$$u_2'(0,t) = 0. \tag{3.4.4}$$

The matching conditions at the end of the flame sheet (x=L) are given by (3.3.1-2).

$$p_2'(L,t) = P_2^+[e^{-iK_2L} - e^{iK_2(2L_2 - L)}]\, e^{-i(\Omega t + M_2K_2L)} \tag{3.4.5}$$

$$u_2'(L,t) = \frac{P_2^+}{\bar{\rho}_2\bar{a}_2}[e^{-iK_2L} + e^{iK_2(2L_2 - L)}]\, e^{-i(\Omega t + M_2K_2L)} \tag{3.4.6}$$

Because this is a linear problem, the complex wave number must be calculated before the wave amplitude P_2^+ can be determined. Hence, the proper boundary condition to be satisfied at x=L is

$$\frac{u_2'(L,t)\ (\bar{\rho}_2\bar{a}_2)}{p_2'(L,t)} = \frac{1 - e^{2iK_2(L_2 - L)}}{1 + e^{2iK_2(L_2 - L)}} \tag{3.4.7}$$

Combination of the integral scheme constructed in Section 3.1 and the boundary conditions given above forms a well-posed problem which can be solved for the complex frequency Ω. The computation is based on an iteration procedure and proceeds as follows. A value for the complex frequency is assumed, and the boundary conditions at the dump plane are calculated from (3.4.1-4). Consequently, we may determine the unsteady flowfields in the combustion zone by integrating (3.1.36-40). With the calculated flow variables at $x=L_4$ the boundary condition (3.4.7) is checked. A new procedure is repeated by assuming another complex frequency Ω until (3.4.7) is satisfied. To improve the rate of convergence of the iterative scheme, we utilize an IMSL routine ZANLYT in which the Muller method with deflation is used.[16]

3.5 Discussion of Results

The calculated frequencies and growth constants of oscillations in two research dump combustors (configuration B)[1] for the test conditions given in Table 3.1 are shown in Table 3.2. The second mode frequencies check the measured results well. The growth constants are positive except for the third mode oscillations, in which the wave amplitudes decay with time.

For ramjet combustors, there are at least two possible processes contributing to the excitation of pressure oscillations: shedding of vortices followed by periodic pulsing combustion; and fluctuation of burning rate due to fluid dynamic stretching of flame front. The former has long been recognized as the mechanism driving high frequency instability.[17] A similar phenomenon may be active in respect to low frequency longitudinal oscillations but no firm evidence has been given. According to the model constructed here, the interaction between the unsteady motions and the flame front provides the necessary energy required for sustaining pressure oscilla-

Table 3.2 Calculated complex frequencies

baseline combustor (L_2=0.406 m, $f_{measured}$=457 Hz)		
first mode	f=222 Hz	α= 9 1/s
second mode	f=454 Hz	α=14 1/s
third mode	f=562 Hz	α=−5 1/s
baseline combustor (L_2=0.508 m, $f_{measured}$=371 Hz)		
first mode	f=220 Hz	α=1.42 1/s
second mode	f=403 Hz	α=2.71 1/s
third mode	f=540 Hz	α=−1.3 1/s

tions. This is confirmed by the positive growth constants for the lower modes. Earlier works for the the unsteady flame spreading[3,18] have shown that indeed the acoustic signal may be amplified significantly at certain characteristic frequencies when passing through an unsteady flame sheet.

Figure 3.7 shows the distributions of the acoustic pressure amplitude and phase for various modes in the baseline combustor. The dominant second mode in the experiment corresponds to a quarter wave in a closed-open organ pipe. The phase distributions are uniform, suggesting that the waves be standing. When a longer combustor is treated, the frequencies decrease due to the increase of the chamber length, but the mode structure remains the same, as shown in Figure 3.8.

A parametric study of the influence of the vortex strength on the unsteady flowfield is also conducted. Results have indicated that in the present case, the frequencies are insensitive to the choice of ω_0. The geometry is the dominant factor. This may be due to the small Mach number of the mean flow and the high blockage of the duct at the dump plane.

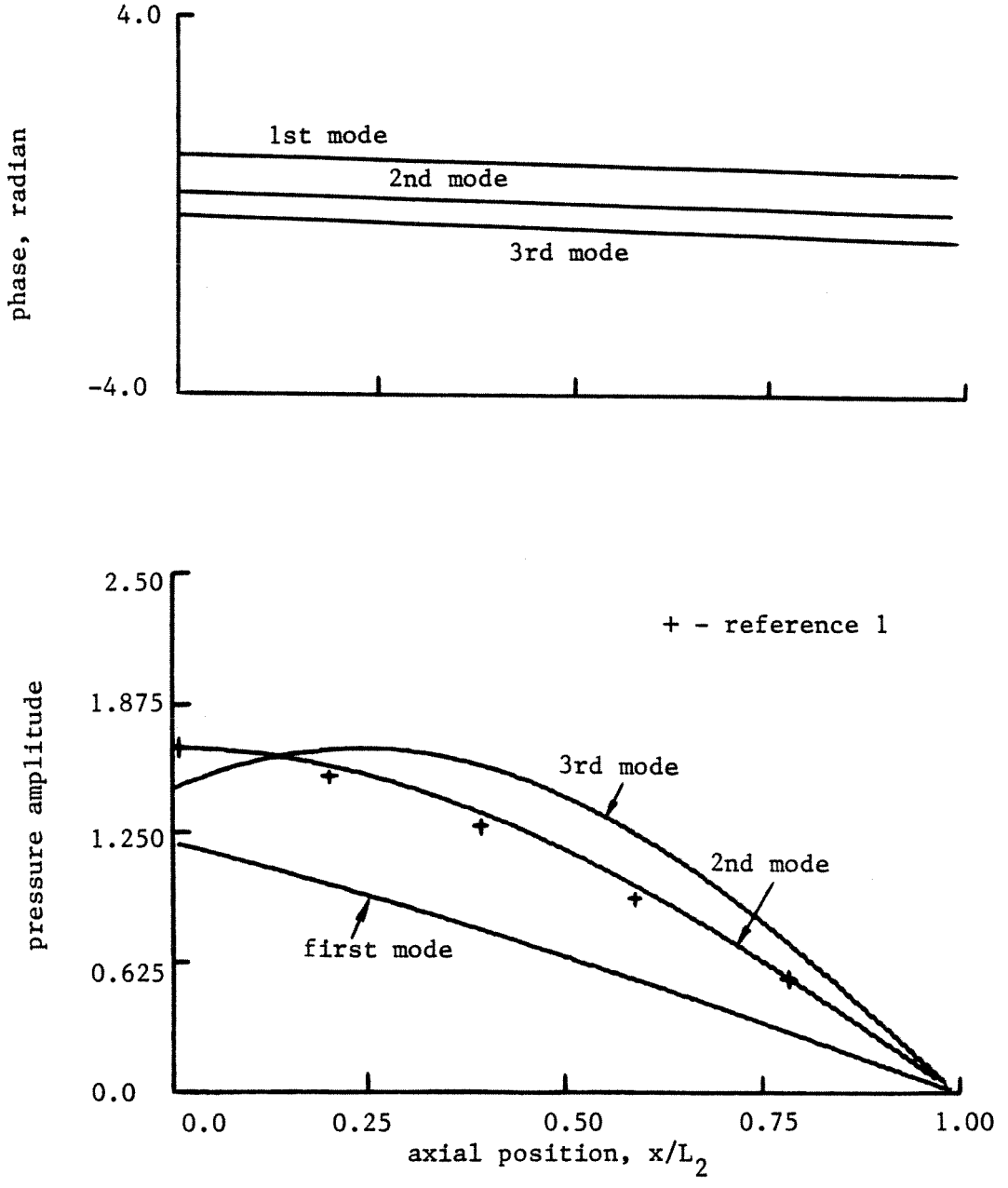

FIGURE 3.7. Measured and Calculated Acoustic Pressure Amplitude and Phase Distributions (Baseline Combustor)

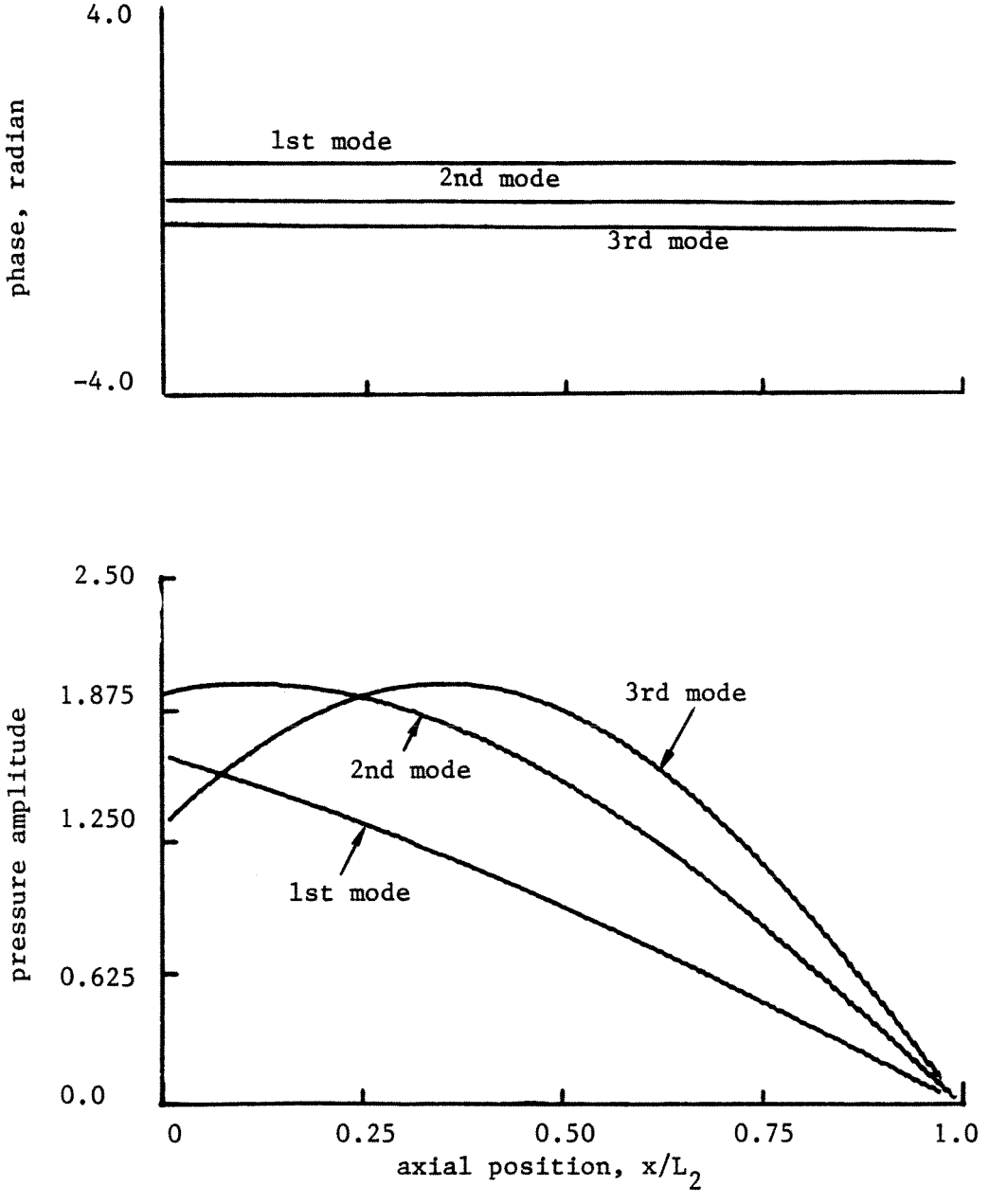

FIGURE 3.8. Measured and Calculated Acoustic Pressure Amplitude and Phase Distributions (Longer Combustor)

3.6 Concluding Remarks

An integral scheme has been developed to study the flowfields in two-dimensional dump combustors. This work is the first in which the severe gradients in the properties of the mean flow have been accounted for in the analysis of unsteady motions. Since the oscillations are treated within quasi one-dimensional approximation, the effects of the vortex shedding, either from the lip of the dump combustor or from the curved flame sheet, and the unsteady recirculating flow on the acoustic field are not accommodated. These merit thorough consideration in the future.

APPENDIX 3A

CALCULATION OF MEAN RECIRCULATING FLOW

This appendix presents the solution to the two-dimensional Poisson equation (3.1.25), using the conformal mapping technique. The procedure is essentially the approach taken in reference 19. Figure 3A.1 shows the model of the flow considered. Because of the dependence of the curve AB on the x-coordinate, no closed form solution can in general be obtained in the physical Z plane. We therefore map the configuration conformally to a unit semi-circle in the Q-plane where an analytic solution is available.

We assume that the curve AB in the Z plane is perpendicular to the coordinate axes at the points A and B. With the Schwarz-Christoffel transformation,[20] it can be transformed into an arc in the Z_1 plane according to the following formula.

$$Z_1 = \frac{Z^2 - a}{b}, \quad \text{where } a = \frac{1 - l_2^2}{2}, \text{ and } b = \frac{1 + l_2^2}{2} \tag{3A.1}$$

Since the radii of curvature are very small in the vicinities of the points A and B, unacceptable numerical inaccuacy may be generated due to the strong gradients.

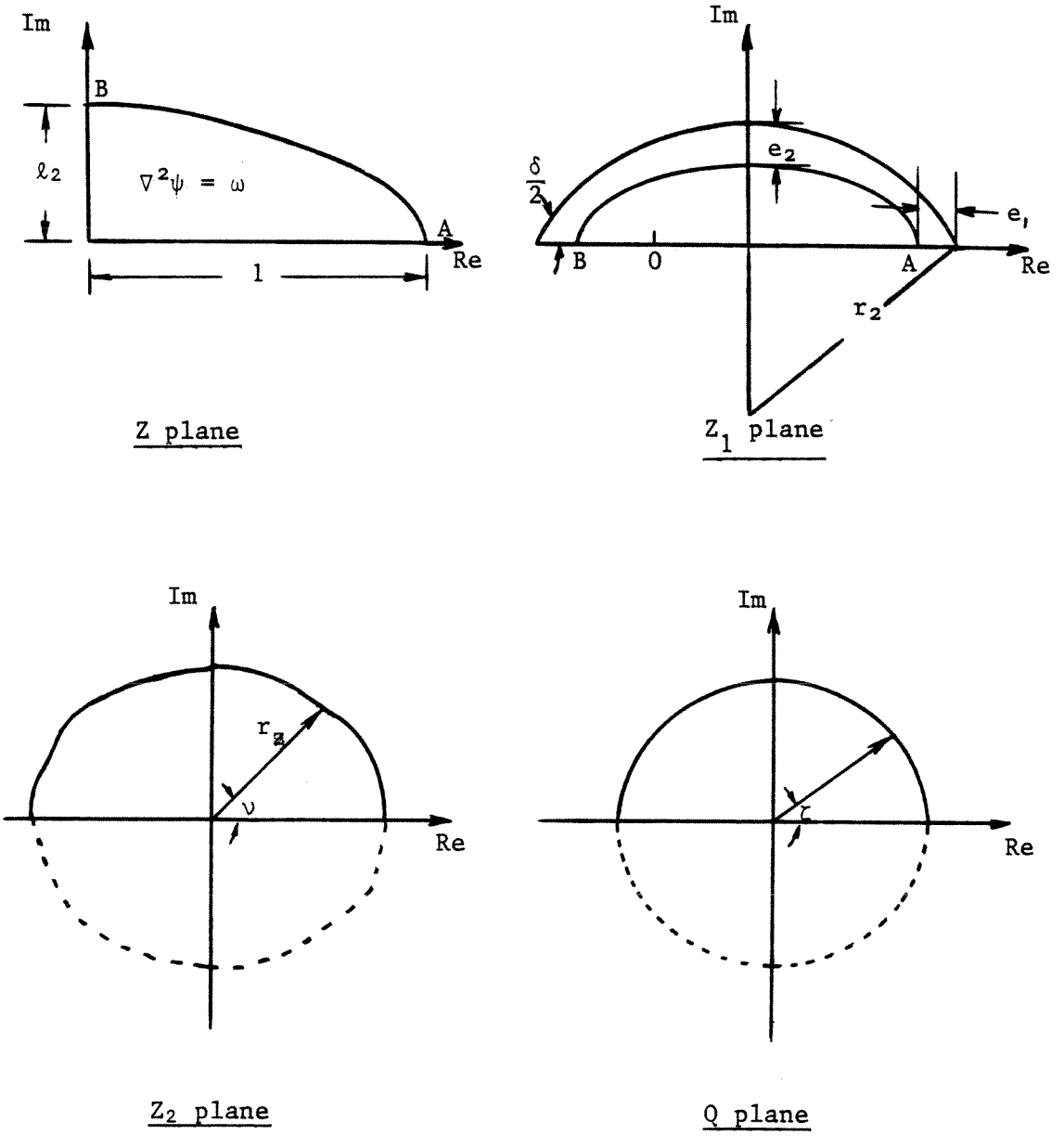

FIGURE 3A.1. Conformal Mapping of the Recirculation Zone to a Unit Semi-Circle

To aviod this difficulty, a second transformation is performed, which maps the circular arc enclosing the curve AB in the Z_1 plane to a semi-circle in the Z_2 plane.

$$Z_2 = \frac{(r_2\sin\frac{\delta}{2} + Z_1)^{\frac{\pi}{\delta}} - (r_2\sin\frac{\delta}{2} - Z_1)^{\frac{\pi}{\delta}}}{(r_2\sin\frac{\delta}{2} + Z_1)^{\frac{\pi}{\delta}} + (r_2\sin\frac{\delta}{2} - Z_1)^{\frac{\pi}{\delta}}} \tag{3A.2}$$

where $\delta/2$ is the angle between the circular arc and the real axis. Treated in this manner, the curve AB becomes a nearly semi-circle in the Z_2 plane. The strong gradients in the vicinities of the points A and B have been significantly reduced.

The mapping from a nearly semi-circle to a unit semi-circle in the Q plane is achieved using Theodorson's integral formula.[21] Mathematically, this formula maps a unit disk to any given domain and, with the notations in Figure 3A.1, is written as

$$\nu(\xi) - \zeta = \mathbf{C}[\ln r_z(\nu)] \tag{3A.3}$$

where **C** represents the complex conjugate function. Equation (3A.3) can be easily solved using the iterative Fast Fourier Transformation method.[21] We first expressed the functions on the both sides of (3A.3) in the complex Fourier series:

$$\ln r_z(\nu) = \sum_{-\infty}^{\infty} a_m e^{im\sigma} \tag{3A.4}$$

$$\nu - \zeta = \sum_{-\infty}^{\infty} b_m e^{im\sigma} \tag{3A.5}$$

Since each function is conjugate harmonic to the other, the Fourier coefficients a_m and b_m are simply related as[21]

$$b_m = \begin{cases} -ia_m & \text{if } m>0 \\ 0 & \text{if } m=0 \\ ia_m & \text{if } m<0 \end{cases} \tag{3A.6}$$

The overall calculation proceeds as follows.

$$\nu^{j+1} - \zeta = C[\ln r_z(\nu^j)] \tag{3A.7}$$

With the information known at the jth step, we may compute ν at the (j+1)th step from (3A.4-7). The same procedure is repeated until the solution becomes convergent.

Having found the mapping functions, we are now able to derive the solution to the Poisson equation (3.1.25). For convenience, the particular and harmonic parts of the solution are treated separately. The particular solution ψ_p has the form

$$\psi_p = \frac{1}{\pi}\mathrm{Im}(Z^2 \ln Z) + \frac{1}{2}(\mathrm{Im}Z)^2 \tag{3A.8}$$

where Im denotes the imaginary part of the complex function. Note that ψ_p vanishes on both the real and imaginary axes, producing a symmetric solution of ψ_h about the real axis in the Q plane. The method of image can thus be applied. Since the domain of the solution has been mapped conformally into a unit semi-disk, the harmonic function ψ_h in the Q plane can be represented by the Fourier series with coefficients determined from the boundary conditions.

$$\psi_h = \sum_{-\infty}^{\infty} \Psi_k e^{ik\zeta} \tag{3A.9}$$

The velocity field in the recirculation zone is calculated by taking the normal derivative of the stream function.

$$V = \left(\frac{\partial \psi}{\partial n}\right)_Z = \left(\frac{\partial \psi}{\partial n}\right)_Q \left|\frac{dQ}{dZ}\right| = \left(\frac{\partial \psi_h}{\partial n} + \frac{\partial \psi_p}{\partial n}\right)_Q \left|\frac{dZ}{dQ}\right|^{-1} \tag{3A.10}$$

Substitution of (3A.8-9) into the above equation and rearrangement of the result lead to

$$V = \left|\frac{dZ}{dQ}\right|^{-1}\left\{\left(\frac{\partial \psi_h}{\partial n}\right)_Q + \frac{1}{\pi}\mathrm{Im}[2ZQ\ln Z(\frac{dZ}{dQ}) + QZ(\frac{dZ}{dQ})] + (\mathrm{Im}Z)\mathrm{Im}(Q\frac{dZ}{dQ})\right\} \tag{3A.11}$$

where

$$\left(\frac{\partial \psi_h}{\partial n}\right)_Q = \sum_{-\infty}^{\infty} |k| \Psi_k e^{ik\zeta} \tag{3A.12}$$

To check the validity of the analysis, a series of numerical calculations of the velocity field in the recirculation zone are carried out with different allowances e_1 and e_2 in the Z_1 plane. The step height l_2 and the vortex strength ω_0 are chosen to be one sixth and unity respectively, and the dividing streamline AB is represented by an ellipic arc. Figure 3A.2 shows the velocity distributions on the dividing streamline. The solution depends heavily on e_1 and e_2. By using suitable mappings, the difficulties associated with the singular behaviors at points A and B can be effectively overcome.

REFERENCES 3

1. Smith, D, *Investigation of Flame Stabilized by a Rearward-Facing Step*, Ph.D. Thesis, California Institute of Technology, Pasadena, California, 1985.
2. Jarosinski, J. and Wojcicki, S., 'The Mechanism of Interaction between a Combustion Region and Acoustic Resonator," *Acta Astronautica*, Vol.3, 1976, pp. 567-572.
3. Marble, F. E. and Candel, S. M., "An Analytical Study of the Non-Steady Behavior of Large Combustor," *Seventeenth Symposium (International) on Combustion*, August 1978, pp.761-769.
4. Williams, F. A., "A Review of Some Theoretical Considerations of Turbulent Flame Structures," *AGARD-CP-164* 1974, Sec. II-1.
5. Williams, F. A., *Combustion Theory*, Addison-Wesley Publishing Company, 1965.
6. Michalke, A., "On the Inviscid Instability of Hyperbolic Tangent Velocity Profile," *Journal of Fluid Mechanics*, Vol.19, 1964, pp. 543-556.
7. Markstein, G. H., *Nonsteady Flame Propagation*, The MacMillan Company, 1964.
8. Thurston, D. W., "An Experimental Investigation of Flame Spreading from Bluff Body Flameholder," Thesis, California institute of Technology, Pasadena, Californis, 1958..
9. Wright, F. H. and Zukoski, E. E., 'Flame Spreading from Bluff Body Flame Holders," *8th Symposium (International) on Combustion*, 1960.
10. Batchelor, G. K., "A Proposal Concerning Laminar Wakes behind Bluff Bodies at Large Reynolds Number," *Journal of Fluid Mechanics*, Vol.1, 1956, pp. 388-398.
11. Smith, P. D., "A Note on the Computation of the Inviscid Rotational Flow Past the Trailing Edge of an Aerofoil," *R. A. E. Tech Memo. Aero. 1217.*

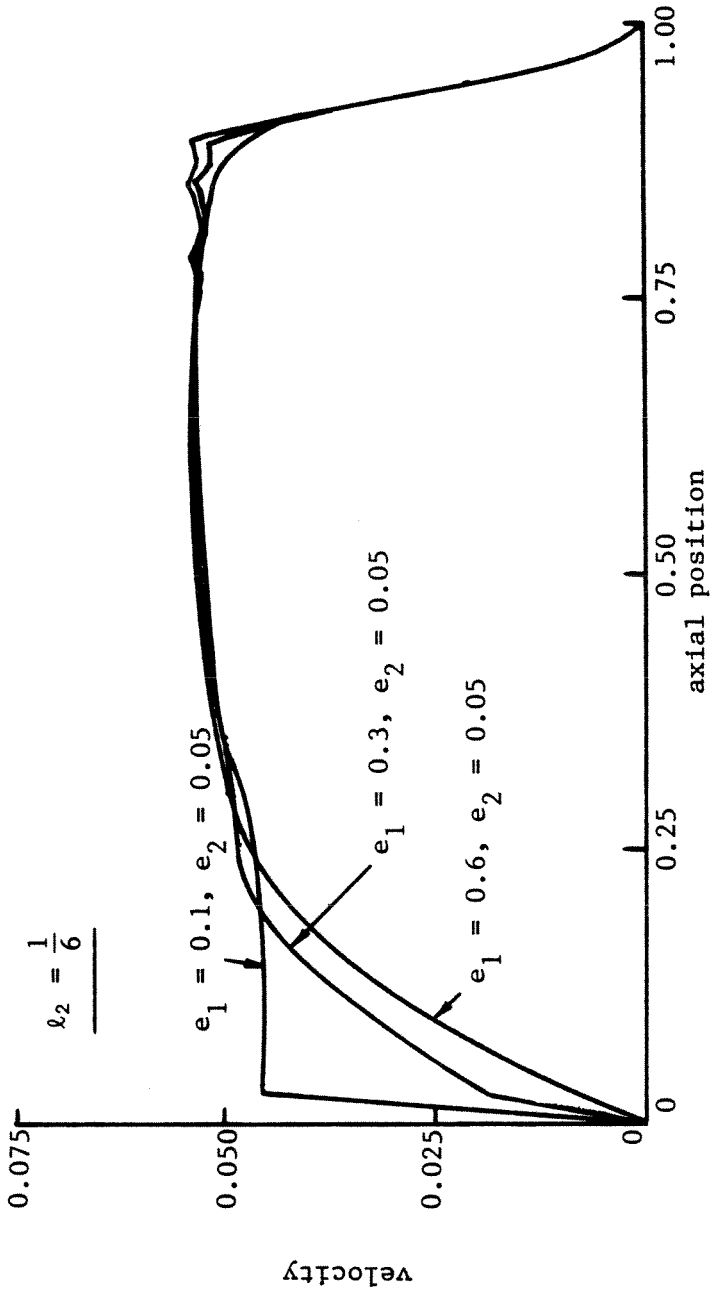

FIGURE 3A.2. Distributions of the Tangential Velocity along the Dividing Streamline

12. Taulbee, D. B. and Robertson, J.M., 'Turbulent Separation Analysis Ahead of a Step," *Journal of Basic Engineering*, Vol.D94, 1972, pp. 544-550.

13. Meis, T., *Numerical Solution of Partial Differential Equations*, Springer-Verlag, New York, 1981.

14. Zeldovich,Y. B., Istratov, A. G., Kidin, N. I., and Librovich, V. B., 'Flame Propagation in Tubes: Hydrodynamics and Stability," *Combustion Science and Technology*, Vol.24, 1980, pp. 1-13.

15. Subbaiah, M. V., 'Nonsteady Flame Spreading in Two-Dimensional Ducts," *AIAA Journal*, Vol.21, No.11, November 1983.

16. *IMSL Library*, Edition 9, IMSL, Inc., 1982

17. Rogers, D. E. and Marble, F. E., "A Mechanism for High Frequency Oscillations in Ramjet Combustors and Afterburners," *Jet Propulsion*, Vol.26, 1956, pp.456-462.

18. Yang, V., Private Communication with F. E. C. Culick, August 1981.

19. Saffman, P. G. and Tanveer, S., 'Prandtl-Batchelor Flow Past a Flat Plate with a Forward Facing Flap," accepted for publication in *Journal of Fluid Mechanics*,

20. Nehari, Z., *Conformal Mapping*, McGraw-Hill Book Co. Inc., 1952.

21. Henrici, P., 'Fast Fourier Methods in Computational Complex Analysis," *SIAM Review*, Vol.21, No.4, Oct.1979.

NOMENCLATURE 3

a	speed of sound
h	step height
K	modified complex wave number, defined by (3.2.3)
M	Mach number
p	pressure
r	inlet height at the dump plane
R	height of combustor
s	entropy
t	time
T	temperature
u	axial velocity
v	transverse velocity
W	flame speed
x	position coordinate along the axis of the engine
α	growth constant
β_f	flame speed parameter, define by (3.1.16)
β_p	acoustic reflection coefficient at the entrance

β_ρ density ratio of the unburned to the burned gases

η_1 y-coordinate of flame sheet

η_2 y-coordinate of dividing streamline

γ ratio of specific heats

ω frequency

ω_o vortex strength

Ω complex frequency, $\Omega = \omega + i\alpha$

φ velocity potential

ψ stream function

ρ density

ΔH heat of combustion per unit mass of fuel

superscript

$(\bar{})$ mean quantity

$(\ )'$ fluctuation

$\hat{}$ average quantity

subscripts

1 values of the unburned flow (reion 1)

2 values of the direct burned flow (reion 2)

3 values of the recirculating flow (reion 3)

in values of the inlet flow at the dump plane

Chapter 4

FORMULATION OF TWO-PHASE FLOW PROBLEMS AND NUMERICAL TECHNIQUES

So far we have only investigated linear unsteady motions in a coaxial-dump ramjet engine. In practice, the unsteady motions are such that nonlinear effects must be accounted for. Examples of these are finite amplitude oscillations, and behavior which apparently shows the existence of limiting cycles. For ramjet engines, moreover, it appears that the fundamental processes responsible for the the excitation of oscillations are nonlinear.

Theoretical analysis of nonlinear oscillations may be carried out either analytically or numerically. Each method has advantages which are complementary to the other; the choice depends on the features of the problem. An analytical treatment provides a formal way to link linear and nonlinear analyses, a detailed description of physical processes, and a less expensive means of accessing parametric influences. On the other hand, it suffers difficulties from lengthy formulation and sometimes cannot represent easily and accurately the various processes involved. In the present work, the flowfields are so complicated even within the one-dimensional approximation; that we shall use numerical techniques. The purpose of this chapter is to give a general formulation of the problem, followed by a description of relevant numerical methods.

4.1 Formulation

The analysis is based on a one-dimensional model for two-phase flow. The gas phase contains air, fuel vapor, and combustion products; its instantaneous composition depends on the flow condition and the chemical reactions. The liquid phase is composed of fuel droplets and treated as a fluid with density ρ_p^*, mass per unit volume of the chamber. Conversion of liquid phases to gas may occur at the rate $\dot{\omega}_v^*$

due to the droplet vaporization or combustion. For convenience, $\dot{\omega}_v^*$ is written in terms of the surface regression rate of the droplet, r_b^*.

$$\dot{\omega}_v^* = A_s^* \rho_l^* r_b^* \tag{4.1.1}$$

where A_s^* is the specific surface area of droplets, total surface area of droplets per unit volume of the chamber, and ρ_l^* is the density of the liquid fuel. If we neglect viscous effects, heat conduction and relative diffusion of species, and assume the fuel droplets are monodispersed and uniformly distributed over the entire cross-sectional area, the the conservation equations are

mass equation (gas-phase)

$$\frac{\partial \rho^*}{\partial t^*} + \frac{1}{A^*}\frac{\partial(\rho^* u^* A^*)}{\partial x^*} = \dot{\omega}_g^* + A_s^* \rho_l^* r_b^* \tag{4.1.2}$$

mass equation (liquid phase)

$$\frac{\partial \rho_p^*}{\partial t^*} + \frac{1}{A^*}\frac{\partial(\rho_p^* u_p^* A^*)}{\partial x^*} = \dot{\omega}_p^* - A_s^* \rho_l^* r_b^* \tag{4.1.3}$$

momentum equation

$$\frac{\partial}{\partial t}(\rho^* u^* + \rho_p^* u_p^*) + \frac{1}{A^*}\frac{\partial}{\partial x^*}\left[(p^* + \rho^* u^{*2} + \rho_p^* u_p^{*2})A^*\right]$$

$$= \frac{p^*}{A^*}\frac{dA^*}{dx^*} + u_{sg}^* \dot{\omega}_g^* + u_{sp}^* \dot{\omega}_p^* \tag{4.1.4}$$

energy equation

$$\frac{\partial}{\partial t^*}\left[\rho^*\left(\frac{c_p^*}{\gamma}T^* + \frac{u^{*2}}{2}\right) + \rho_p^*\left(c_l^* T_p^* + \frac{u_p^{*2}}{2}\right)\right]$$

$$+ \frac{1}{A^*}\frac{\partial}{\partial x^*}\left[\rho^* u^* A^*\left(\frac{c_p^*}{\gamma}T^* + \frac{u^{*2}}{2}\right) + \rho_p^* u_p^* A^*\left(c_l^* T_p^* + \frac{u_p^{*2}}{2}\right)\right]$$

$$= \frac{-1}{A^*}\frac{\partial(u^*p^*A^*)}{\partial x^*} + \dot{\omega}_g^*(c_p^*T_{sg}^* + \frac{u_{sg}^{*2}}{2}) + \dot{\omega}_p^*(c_l^*T_{sp}^* + \frac{u_{sp}^{*2}}{2}) + \ + \dot{m}_{k,f}^*\Delta H^* \qquad (4.1.5)$$

species equation

fuel $$\frac{\partial(\rho^*Y_f)}{\partial t^*} + \frac{1}{A^*}\frac{\partial(\rho^*Y_f u^*A^*)}{\partial x^*} = -\dot{m}_{k,f}^* + A_s^*\rho_l^* r_b^* \qquad (4.1.6)$$

oxydizer $$\frac{\partial(\rho^*Y_o)}{\partial t^*} + \frac{1}{A^*}\frac{\partial(\rho^*Y_o u^*A^*)}{\partial x^*} = -\dot{m}_{k,o}^* \qquad (4.1.7)$$

where asterisks denote dimensional quantities. A nomenclature is given in the end of this chapter. Note that the mass source terms $\dot{\omega}_g^*$ and $\dot{\omega}_p^*$ are introduced only at the injector position, representing respectively the mass fluxes of air and liquid fuel entering the chamber through the fuel injection system.

Following some straightforward manipulations, we can write the momentum and energy equations for each phase by taking into account the proper interactions between the gas and liquid flows.

momentum equation (gas-phase)

$$\frac{\partial(\rho^*u^*)}{\partial t^*} + \frac{1}{A^*}\frac{\partial}{\partial x^*}\left[(p^* + \rho^*u^{*2})A^*\right] = \frac{p^*}{A^*}\frac{dA^*}{dx^*} + u_{sg}^*\dot{\omega}_g^* + F_p^*$$

$$+ A_s^*\rho_l^* r_b^* u_p^* \qquad (4.1.8)$$

momentum equation (liquid-phase)

$$\frac{\partial(\rho_p^*u_p^*)}{\partial t^*} + \frac{1}{A^*}\frac{\partial}{\partial x^*}(\rho_p^*u_p^{*2}A^*) = u_{sp}^*\dot{\omega}_p^* - F_p^* - A_s^*\rho_l^* r_b^* u_p^* \qquad (4.1.9)$$

energy equation (gas-phase)

$$\frac{\partial}{\partial t^*}\left[\rho^*(\frac{c_p^*}{\gamma}T^* + \frac{u^{*2}}{2})\right] + \frac{1}{A^*}\frac{\partial}{\partial x^*}\left[\rho^*u^*A^*(\frac{c_p^*}{\gamma}T^* + \frac{u^{*2}}{2})\right]$$

$$= \frac{-1}{A^*}\frac{\partial(u^*p^*A^*)}{\partial x^*} + \dot{\omega}_g^*(c_p^*T_{sg}^* + \frac{u_{sg}^{*2}}{2}) + Q_p^* + u_p^*F_p^*$$

$$+ A_s^*\rho_l^*r_b^*(h_v^* + \frac{u_p^{*2}}{2}) + \dot{m}_{k,f}^*\Delta H^* \qquad (4.1.10)$$

energy equation (liquid-phase)

$$\frac{\partial}{\partial t^*}\left[\rho_p^*(c_l^*T_p^* + \frac{u_p^{*2}}{2})\right] + \frac{1}{A^*}\frac{\partial}{\partial x^*}\left[\rho_p^*u_p^*A^*(c_l^*T_p^* + \frac{u_p^{*2}}{2})\right]$$

$$= \omega_p^*(c_l^*T_{sp}^* + \frac{1}{2}u_{sp}^{*2}) - Q_p^* - u_p^*F_p^* - A_s^*\rho_l^*r_b^*(h_v^* + \frac{u_p^{*2}}{2}) \qquad (4.1.11)$$

The energy equation for the liquid phase (4.1.11) is valid only for the subcooled droplets, accounting for the initial heating-up process. The fuel vaporized in this period is ignored. As soon as the droplets reach their saturated states, vaporization occurs and T_p^* remains the boiling temperature. The interactions between two phases depend mainly on the regression rate r_b^* and the velocity difference $u^* - u_p^*$. Therefore, (4.1.11) is replaced by a formula for the surface regression rate written in the Lagrangian coordinate.

$$\frac{Dr_p^*}{Dt^*} \equiv \frac{\partial r_p^*}{\partial t^*} + u_p^*\frac{\partial r_p^*}{\partial x^*} = r_b^* \qquad (4.1.12)$$

4.1.1 Auxiliary Equations

To complete the formulation, the modeling of chemical reactions and the empirical correlations for the initial droplet size, drag force, heat transfer, and the droplet regression rate are required. These terms constitute an important part of the analysis, taking into account the rate of heat release and the coupling between two phases. Among them, the chemical reactions and the droplet regression rate are strongly problem-oriented; it is impractical to make a general statement here. We therefore leave them to Chapter 6 in which some specific problems are dealt with.

Initial Droplet Size. The diameter of the fuel droplet immediately downstream of the injection needs be specified as it is the necessary boundary condition for the liquid flow. The break-up of a fuel stream into small droplets depends greatly on the injector/atomizer employed, the physical properties of the fuel, and the flow conditions. For liquid-fueled ramjet engines, the most commonly used system falls into the category of a blast atomizer to which the correlation obtained by Hussein et al[1] can be directly applied.

$$SMD = 0.703\left(\frac{\sigma_l^* d_{jo}^*}{V_a^{*2}}\right)^{0.5} + 0.04\left(\frac{\mu_l^{*2}}{\sigma_l^* \rho_l^*}\right)^{0.45} d_{jo}^{*0.55} \tag{4.1.13}$$

where SMD stands for the Sauter mean diameter. Equation (4.1.13) indicates that there is *no* influence of liquid jet velocity on the droplet size. The second term on the right hand side accounts for the effect of viscosity, being negligibly small in most cases.

Drag Force. The drag force per unit volume exerted on fuel droplets by the surrounding gas may be expressed in terms of a drag coefficient C_d through the following equation.

$$F_p^* = \frac{3}{8}\rho^* |u_p^* - u^*| (u_p^* - u^*) \frac{1}{\rho_p^*}\left(\frac{\rho_p^*}{\rho_l^*}\right) C_d \tag{4.1.14}$$

Dickerson and Schuman[2] have summarized the experimental data for C_d, giving the result as shown below.

$$C_d = \begin{cases} 27 R_{ei}^{-0.48}, & 0 \le R_{ei} \le 80 \\ 0.271 R_{ei}^{0.217}, & 80 \le R_{ei} \le 10^4 \\ 2, & 10^4 < R_{ei} \end{cases} \tag{4.1.15}$$

where R_{ei} is the Reynolds number based on the relative flow velocity,

$$R_{ei} = \frac{\rho^* |u_p^* - u^*| d_p^*}{\mu^*} \tag{4.1.16}$$

The viscosity μ^* varies with temperature according to the Sutherland law.[3]

Convective Heat Transfer. Carlson and Hoglund's formula[4] for the convective heat transfer coefficient is used to calculate the heat transfer between gas and liquid flows.

$$Q_p^* = \left(\frac{24 c_p^*}{\rho_l^* P_r r_p^{*2}} \right) \mu^* \rho_p^* (T - T_p^*)[2 + 0.459 R_{ei}^{0.55} P_r^{0.55}] \tag{4.1.17}$$

4.1.2 Nondimensionalization

Before the numerical computation is attempted, the governing equations formulated above should be normalized. This procedure is attractive from both the analytical and the numerical points of view. First, it is easier to identify the relative importance of each term in the equation and to interpret the results obtained. Second, the normalized variables with uniform magnitudes improve the numerical accuracy.

By choosing suitable reference quantities, the flow variables are nondimensionalized as given in Table 4.1. Substitution of them into the governing equations and rearrangement of the result produce the nondimensional forms of the equations.

gas-phase mass equation

$$\frac{\partial \rho}{\partial t} + \frac{1}{A} \frac{\partial (\rho u A)}{\partial x} = \omega_g + 3 \rho_p r_b \tag{4.1.18}$$

Table 4.1 Normalized Flow Variables

$x = x^*/L^*_{ref}$	$u_{sg} = u^*_{sg}/a^*_{ref}$	$\omega_p = \omega^*_p L^*_{ref}/\rho^*_{ref}a^*_{ref}$
$A = A^*/A^*_{ref}$	$T_{sg} = T^*_{sg}/T^*_{ref}$	$F_p = F^*_p L^*_{ref}/\rho^*_{ref}a^{*2}_{ref}$
$u = u^*_{sg}/a^*_{ref}$	$u_{sp} = u^*_{sp}/a^*_{ref}$	$Q_p = Q_p L^*_{ref}/\rho^*_{ref}c^*_p a^*_{ref}T^*_{ref}$
$a = a^*/a^*_{ref}$	$T_{sp} = T^*_{sp}/T^*_{ref}$	$c_l = c^*_l/c^*_p$
$t = t^* a^*_{ref}/L^*_{ref}$	$u_p = u^*_p/a^*_{ref}$	$r_b = (r^*_b/r^*_{p,ref})L^*_{ref}/a^*_{ref}$
$T = T^*_{sg}/T^*_{ref}$	$\rho_p = \rho^*_p/\rho^*_{ref}$	$r_p = r^*_p/r^*_{p,ref}$
$p = p^*/p^*_{ref}$	$T_p = T^*_p/T^*_{ref}$	
$\rho = \rho^*/\rho^*_{ref}$	$\omega_g = \omega^*_g L^*_{ref}/\rho^*_{ref}a^*_{ref}$	

gas-phase momentum equation

$$\frac{\partial(\rho u)}{\partial t} + \frac{1}{A}\frac{\partial}{\partial x}\left[\left(\frac{p}{\gamma} + \rho u^2\right)A\right] = \frac{p}{\gamma A}\frac{dA}{dx} + F_p + u_{sg}\omega_g + 3\rho_p r_b u_p \tag{4.1.19}$$

gas-phase energy equation

$$\frac{\partial}{\partial t}\left[\rho\left(\frac{T}{\gamma(\gamma-1)} + \frac{u^2}{2}\right)\right] + \frac{1}{A}\frac{\partial}{\partial x}\left[\rho u A\left(\frac{T}{\gamma(\gamma-1)} + \frac{u^2}{2}\right)\right]$$

$$= \frac{-1}{\gamma A}\frac{\partial(upA)}{\partial x} + \frac{Q_p}{\gamma-1} + u_p F_p + \omega_g\left(\frac{T_{sg}}{\gamma-1} + \frac{u^2_{sg}}{2}\right)$$

$$+ 3\rho_p r_b\left(h_v + \frac{u_p^2}{2}\right) + \dot{m}_{k,f}\Delta H \tag{4.1.20}$$

species equation

fuel $$\frac{\partial(\rho Y_f)}{\partial t} + \frac{1}{A}\frac{\partial(\rho Y_f u A)}{\partial x} = -\dot{m}_{k,f} + 3\rho_p r_b \tag{4.1.21}$$

oxydizer $$\frac{\partial(\rho Y_o)}{\partial t} + \frac{1}{A}\frac{\partial(\rho Y_o u A)}{\partial x} = -\dot{m}_{k,o} \tag{4.1.22}$$

liquid-phase mass equation

$$\frac{\partial \rho_p}{\partial t} + \frac{1}{A}\frac{\partial(\rho_p u_p A)}{\partial x} = \omega_p - 3\rho_p r_b \quad . \tag{4.1.23}$$

liquid-phase momentum equation

$$\frac{\partial(\rho_p u_p)}{\partial t} + \frac{1}{A}\frac{\partial}{\partial x}(\rho u^2 A) = u_{sp}\omega_p - F_p - A_s \rho_l r_b u_p \tag{4.1.24}$$

liquid-phase energy equation

$$\frac{\partial}{\partial t}\left[\rho_p(c_l T_p + \frac{u^2}{2})\right] + \frac{1}{A}\frac{\partial}{\partial x}\left[\rho_p u_p(c_l T_p + \frac{u^2}{2})A\right]$$

$$= \omega_p(c_l T_{sp} + \frac{u_{sp}^2}{2}) - Q_p - u_p F_p - 3\rho_p r_b(h_v + \frac{u_p^2}{2}) + \dot{m}_{k,f}\Delta H \tag{4.1.25}$$

surface regression rate of droplet

$$\frac{Dr_p}{Dt} \equiv \frac{\partial r_p}{\partial t} + u_p\frac{\partial r_p}{\partial x} = r_b \tag{4.1.26}$$

4.1.3 Eigenvalues and Compatibility Relations of the System

The eigenvalues and their associated eigenvectors of the governing equations must be determined in order to have a deeper insight into the problem. As we shall show, this procedure is essential to the development of proper techniques of solution.

With the assumption that the source and the coupling terms can be expressed in algebraic forms, the eigenvalues for each phase are calculated separately. For simplicity, we recast the gas-phase conservation equations (4.1.18-20) in the following matrix form.

$$\begin{bmatrix} 0 & 1 & -\rho \\ \rho & 0 & 0 \\ 0 & 0 & 1 \end{bmatrix}\frac{\partial}{\partial t}\begin{bmatrix} u \\ p \\ T \end{bmatrix} + \begin{bmatrix} p & u & -\rho u \\ \rho u & 1/\gamma & 0 \\ T(\gamma-1) & 0 & u \end{bmatrix}\frac{\partial}{\partial x}\begin{bmatrix} u \\ p \\ T \end{bmatrix} = \begin{bmatrix} c_1 \\ c_2 \\ c_3 \end{bmatrix} \tag{4.1.27}$$

where c_1, c_2, and c_3 are the inhomogeneous terms defined as

$$c_1 = T(3\rho_p r_b - \frac{\rho u}{A}\frac{dA}{dx})$$

$$c_2 = F_p + \omega_g(u_{sg} - u) + 3\rho_p r_b(u_p - u)$$

$$c_3 = -\frac{uT(\gamma - 1)}{A}\frac{dA}{dx} + \frac{\gamma Q_p}{\rho} + \frac{F_p}{\rho}\gamma(\gamma - 1)(u_p - u)$$

$$+ \frac{\omega_g}{\rho}\gamma(\gamma - 1)[\frac{T_{sg}}{\gamma - 1} - \frac{T}{\gamma(\gamma - 1)} + \frac{1}{2}(u - u_{sg})^2]$$

$$+ \frac{3\rho_p r_b}{\rho}\gamma(\gamma - 1)[h_v - \frac{T}{\gamma(\gamma - 1)} + \frac{1}{2}(u - u_p)^2]$$

This equation is conveniently represented by

$$C_1\frac{\partial}{\partial t}X + C_2\frac{\partial}{\partial x}X = C_3 \qquad (4.1.28)$$

where C_1 and C_2 are 3x3 coefficient matrices, and X is a column matrix containing the flow variables. Determination of the eigenvalues is straightforward by solving the matrix equation,

$$|C_2 - \zeta C_1| = 0 \qquad (4.1.29)$$

Three distinct real roots are found, ζ = u+a, u-a, and u, confirming that the system is totally hyperbolic. For subsonic flow, these eigenvalues correspond to the slopes of the right-running, the left-running, and the gas-particle characteristic lines respectively.

The eigenvectors of the system $\underline{\Lambda}$ are then determined from the solution to the homogeneous equation.

$$\Lambda^T(C_2 - \zeta C_1) = 0 \tag{4.1.30}$$

The superscript T denotes the transpose of Λ. After some algebra, these eigenvectors are found to be

$$\Lambda = [1 \quad \gamma a \quad \rho] \qquad \text{for } \zeta = u+a \tag{4.1.31a}$$

$$\Lambda = [1 \quad -\gamma a \quad \rho] \qquad \text{for } \zeta = u-a \tag{4.1.31b}$$

$$\Lambda = [0 \quad 1 \quad \frac{-\rho}{\gamma - 1}] \qquad \text{for } \zeta = u \tag{4.1.31c}$$

Multiplication of (4.1.27) by the eigenvectors and rearrangement of the result lead to three characteristic equations, or compatibility relations.

right-running characteristics

$$\frac{1}{\gamma\rho a}\frac{\delta^+ p}{\delta t} + \frac{\delta^+ u}{\delta t} = \frac{c_1}{\gamma\rho a} + \frac{c_2}{\rho} + \frac{c_3}{\gamma a} \tag{4.1.32}$$

$$\frac{\delta^+}{\delta t} = \frac{\partial}{\partial t} + (u+a)\frac{\partial}{\partial x};$$

left-running characteristics

$$\frac{1}{\gamma\rho a}\frac{\delta^- p}{\delta t} - \frac{\delta^- u}{\delta t} = \frac{c_1}{\gamma\rho a} - \frac{c_2}{\rho} + \frac{c_3}{\gamma a} \tag{4.1.33}$$

$$\frac{\delta^-}{\delta t} = \frac{\partial}{\partial t} + (u-a)\frac{\partial}{\partial x};$$

gas particle line

$$\rho\frac{\partial T}{\partial t} - \frac{\gamma - 1}{\gamma}\frac{\delta p}{\delta t} = \rho\frac{c_3}{\gamma} - \frac{\gamma - 1}{\gamma}c_1 \tag{4.1.34}$$

$$\frac{\delta}{\delta t} = \frac{\partial}{\partial t} + u\frac{\partial}{\partial x}$$

Physically, the left- and the right-running compatibility relations represent the time rates of changes of disturbances along the characteristics. For instance, if the

passage of a disturbance moving with the speed u-a brings a change Δu in velocity, then it will change the pressure by $(\gamma\rho a)\Delta u$ and contributions due to source terms. The quantity $\gamma\rho a$ is commonly known as the flow impedance in classical acoustics. The gas-particle compatibility relation is nothing more than an entropy conservation equation; it represents the time rate of change of entropy following a specific gas particle. If the source terms on the right hand side of (4.1.34) vanish, the conventional isentropic relation is recovered and the compatibility relations along the two characteristics can be simplified as shown below.

For an isentropic flow, the thermodynamic properties may be expressed in terms of pressure only. We therefore define a new thermodynamic function F,

$$F \equiv \int_{\bar{p}}^{p} \frac{dp}{\gamma\rho a} = \frac{2}{\gamma-1}\left(p^{\frac{\gamma-1}{2\gamma}} - \bar{p}^{\frac{\gamma-1}{2\gamma}}\right) = \frac{2}{\gamma-1}(a-\bar{a}) \tag{4.1.35}$$

where $\bar{p}$ and $\bar{a}$ are the mean pressure and sonic speed respectively. Substitution of F for the pressure derivatives appearing in (4.1.32) and (4.1.33) leads to the compatibility relations for an isentropic flow.

$$\frac{\delta^{\pm}}{\partial t}(u \pm F) = \frac{\delta^{\pm}}{\partial t}\left(\frac{2a}{\gamma-1} \pm u\right) = -\frac{au}{A}\frac{dA}{dx} \tag{4.1.36}$$

The deviations of u+F and u-F from their mean values correspond to the wave amplitudes along each family of characteristics. For constant-area flow, these quantities remain constant and are the Riemann invariants.

As far as the liquid phase is concerned, the fluidization of fuel droplets allows no signal propagating through them. The only eigenvalue surviving is the local liquid flow velocity u_p; the governing equations change from totally hyperbolic to hyperbolic with the existence of two compatibility relations along the liquid particle line.

$$\frac{\delta u_p}{\partial t} = \frac{\omega_p}{\rho_p}(u_p - u_{sp}) - \frac{F_p}{\rho_p} \tag{4.1.37}$$

$$\frac{\delta T_p}{\partial t} = \frac{\omega_p}{\rho_p}(T_{sp} - T_p) + \frac{\omega_p}{2\rho_p}\left(\frac{\gamma-1}{c_l}\right)(u_{sp}^2 - u_p^2) - \frac{Q_p}{\rho_p c_l}$$

$$+ 3r_b\left[T_p + \frac{u_p^2(\gamma-1)}{2c_l}\right] \tag{4.1.38}$$

where

$$\frac{\delta}{\delta t} = \frac{\partial}{\partial t} + u_p \frac{\partial}{\partial x}$$

Several remarks regarding the liquid-phase compatibility equations should be made at the point. First, equations (4.1.37) and (4.1.38) are exactly the same as the momentum and energy equations in the Eulerian forms. This is due to the fact that the dispersion of liquid particles prohibits the presence of wave-like motion in the liquid phase. The fluid motion is necessarily convective. Second, the energy equation (4.1.38) is valid only for the subcooled liquid flow. When the droplets reach their saturated states, a formula for the surface regression rate (4.1.26) must be used, as discussed earlier. Third, since there is no relation between the bulk density of liquid flow and the droplet temperature, the liquid-phase mass equation is decoupled from the energy equation and cannot be written in the characterisitc form.

4.1.4 Specification of Boundary Conditions

The flow properties at both boundaries for each phase need to be specified in order to solve the problem. For gas flow, these boundary conditions are formulated by considering physical situations and compatibility relations obtained from the method of characteristics.[5,6] Use of the method of characteristics to specify boundary conditions ensures correct signal propagation and consequently consistency

and stability of the numerical results.[7]

Three independent conditions are required as there are three first order governing equations. Focusing attention on the upstream boundary, one should consider four different cases as shown in Figure 4.1. Case 1 represents a subsonic inflow into the engine. The left-running characteristic line (II) serves as a compatibility relationship at the entrance, linking the flow properties in the interior region to those at the boundary; therefore, two physical boundary conditions are required. Case 2 represents a sonic or supersonic inflow. Since there is no characteristic line running from the interior region at the present time to the boundary at the future time, three physical boundary conditions should be specified. Case 3 represents a subsonic outflow at the entrance. Two characteristic lines (II and III) run from the interior region at the present time to the boundary at the future time; therefore, only one physical boundary condition is required. Case 4 represents a sonic or supersonic outflow. Since no outside disturbances can propagate into the interior of the engine, no physical boundary condition can be specified. The boundary conditions are determined solely from the three compatibility relations.

In brief, the number of physical boundary conditions required depends not only on the flow direction but also on the relative magnitude of the flow velocity to the speed of sound, i.e., on the Mach number. The same principle is applied to determine the downstream boundary conditions.

The specification of boundary conditions for the liquid phase is relatively simple. Since no signal can propagate through the dispersed droplets, it is not necessary to use compatibility relations. The boundary conditions are therefore determined either from physical conditions or numerical one-sided differences, depending on the flow direction. Detailed analysis[8] has shown that the one-sided difference has the same virtue as the liquid-phase compatibility relation, at least within the first

CASE 1

$u > 0$
$u < a$

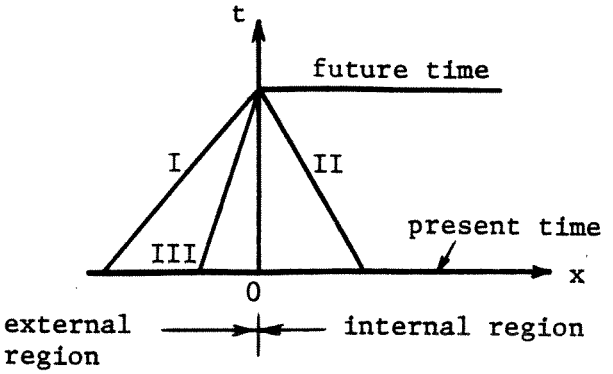

CASE 2

$u > 0$
$u \geq a$

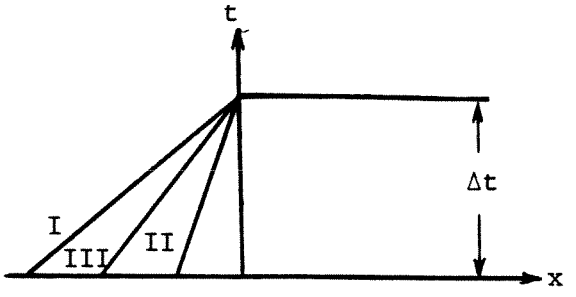

CASE 3

$u < 0$
$|u| < a$

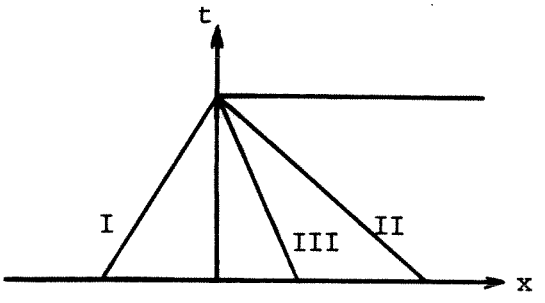

CASE 4

$u < 0$
$|u| \geq a$

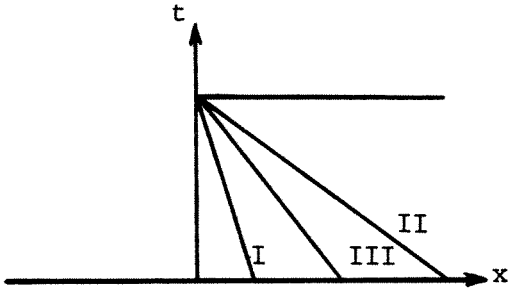

$$\left(\frac{dx}{dt}\right)_I = u + a; \left(\frac{dx}{dt}\right)_{II} = u - a; \text{ and } \left(\frac{dx}{dt}\right)_{III} = u$$

Figure 4.1 Dependence of Boundary Condition Specifications on Flow Situations

order accuracy.

Two different cases, inflow and outflow, should be considered here. In the inflow case, the fuel droplets flow from the exterior to the interior regions; the boundary conditions are specified entirely by the physical conditions at the boundary since the interior flowfields have no effects on them. For the outflow, the situation is reversed. The disability of the liquid flow in the interior region to sense the changes outside the boundary suggests using one-sided differences for the calculation of boundary conditions.

4.2 Numerical Method

In this section, the numerical techniques used to solve the set of nonlinear governing equations (4.1.15)-(4.1.23) are discussed. We start with a brief review of relevant theories underlying numerical methods for hyperbolic problems. After a survey of various techniques, some important criteria for the selection of adequate methods are addressed. Finally, a description of the self-adjusting hybrid scheme with artificial compression is given.

4.2.1 Weak Solution and Entropy Condition

To simplify the description, the gas-phase conservation equations formulated in the previous section are written in the following shorthand notation,

$$\frac{\partial F}{\partial t} + \frac{\partial G}{\partial x} = Z \tag{4.2.1}$$

where F, G, and Z are column vectors containing the conserved flow properties , the fluxes of these properties, and the source and coupling terms respectively. Since the inhomogeous part Z usually does not affect the fundamental features of the equation, in the study of numerical method it is sufficient to consider only the homogeous part of the equation,

$$\frac{\partial F}{\partial t} + \frac{\partial G}{\partial x} = 0 \tag{4.2.2}$$

subject to proper initial and boundary conditions. By differentiating the flux vector G with respect to F, a quasi linear system of the above equation is obtained.

$$\frac{\partial F}{\partial t} + A\frac{\partial F}{\partial x} = 0 \tag{4.2.3}$$

where A is the Jacobian matrix, $\partial G/\partial F$. The system is called hyperbolic in the sense that the matrix A has three real eigenvalues for all values of F. For gas dynamic problems, the flux vector G is homogenous of degree one[9] with respect to F; consequently,

$$G = AF \tag{4.2.4}$$

Because of the nonlinearity of (4.2.2), no smooth solution will in general exist in the entire time and space domain of interest. Shock discontinuities may take place, across which the Rankine-Hugoniot relation holds,[10]

$$S = \frac{G_1 - G_2}{F_1 - F_2} = \frac{[G]}{[F]} \tag{4.2.5}$$

The subscripts 1 and 2 denote respectively the states immediately ahead of and behind the discontinuity, and S is the speed of propagation of the discontinuity. Mathematically, the composite solution which satisfies (4.2.2) at points of continuity and allows jump discontinuities satisfying the shock condition (4.2.5) is called the weak solution in contrast to the strong or smooth solution.

The concept of weak solution appears commonly in the development of numerical schemes for hyperbolic equations. It may be defined alternatively by an intergral relation,[10]

$$\iint_R (F\frac{\partial \varphi}{\partial t} + G\frac{\partial \varphi}{\partial x})dxdt + \int \varphi(x,0)\psi(x)dx = 0 \tag{4.2.6}$$

where R is an arbitrary domain in the (x,t) plane, φ is an arbitrary test function

which has continuous first derivative and vanishes on the boundary of R, and ψ is the initial condition. Function F is called the weak solution of (4.2.2) if the intergral relation (4.2.6) is satisfied for every φ. This alternative definition provides a convenient means to check the validity of a numerical scheme and has been extensively used.

In spite of its mathematical significance and usefulness, the weak solution based on (4.2.6) is non-unique. One has to impose a so-called entropy condition on discontinuities ,i.e., the entropy must increase with flow through shock, in order to determine a physically acceptable solution. Oleinik[11] has shown that this condition can be represented by the following expression,

$$\frac{G(F) - G(F_1)}{F - F_1} \geq S \leq \frac{G(F) - G(F_2)}{F - F_2} \tag{4.2.7}$$

for all F between F_1 and F_2. Also, a weak solution satistifying the entropy condition is uniquely determined by its initial data. A discussion of the role of entropy in numerical calculation has been recently given in reference 12.

4.2.2 Characteristic and Conservation Forms

The system of hyperbolic equations possesses the property that it can be written in two equivalent ways called the *characteristic* and *conservation* forms. These are fundamentally important in the theories underlying numerical schemes. By characteristic form we mean that the governing equations can be written in the characteristic form with the existence of complete sets of eigenvalues and eigenvectors. The resulted characteristic equations provide information about the directions of signal propagation and have long been used as the basis for solving hyperbolic problems. By conservation law we mean that the governing equations are formulated in terms of conserved flow quantities such as mass, momentum, and energy. The total amount of these quantities contained in a control volume

changes only due to the fluxes across the boundary, regardless of the flow distributions inside the volume. Lax and Wendroff[13] have shown in their classic work that if a finite difference scheme in conservative form is convergent, it converges to a weak solution of the governing equations. The conservation law, together with the entropy condition, plays an essential role for a finite difference scheme to capture shock discontinuities adequately.

Depending on the utilization of these two properties, the numerical schemes for solving hyperbolic problems usually fall into the following four categories:

1. method based solely on characteristic information;
2. method based solely on conservative formulation;
3. method based on nonconservation formulation but using characteristic information;
4. and method based on both conservative formulation and characteristic information.

Method of Characteristics. This method simplifies the governing partial differential eqations into a system of nonlinear ordinary differential equations and has long been recognized as a natural way to solve the prolem. For example, Levine and Culick[14] employed this method in their investigation of combustion instabilities in solid propellant rockets. The accuracy of this method is known, but it usually involves complicated and lengthy programming efforts. An undue number of iterations are required to locate the intersections of the characteristic lines and therefore to calculate the flow properties at desirable positions. As a result, it is now generally recognized that this method is best used only for the specification of boundary conditions in which the correct characteristic information is required.

Conservative Difference Scheme. This scheme, which preserves the conserved flow properties in the finite difference approximation and satisfies the entropy

condition, provides an effective means for solving hyperbolic problems with jump discontinuities. The primary advantage is the capability of capturing shocks, i.e., a shock evolves automatically and accurately in the course of calculation. However, it suffers two deficiencies. First, the numerical diffusion and dispersion due to the truncation error smear out the discontinuities, especially for contact discontinuities. Second, most conservative difference schemes produce oscillations in the vicinity of the shock which sometimes may trigger nonlinear numerical instabilities. Vreugdenhill[15] has shown that except for some first order schemes such as Lax's staggered scheme, nonmonotonic shock profiles are inevitable due to spacial interpolations of flow properties across the shock.

Among the several ways to circumvent these defects, the artificial dissipation technique and the self-adjusting hybrid scheme with artificial compression seem to be most powerful and have been applied to various problems. Following the pioneering work of Von Neumann and Richtmyer,[16] many forms of artificial viscosity have been proposed. The purpose is to suppress, not eliminate, oscillations in the shock region while allowing the shock transition to occupy only a few mesh points and retaining the higher order accuracy in the smooth region. For Lax-Wendroff type schemes, the method due to Lapidus[17] has been widely used; it is very easy to be incorporated into an existing scheme and to fit into the conservation form. The use of an artificial viscosity is not advisable in the present application because it can not completely eliminate the ragged appearance of the shock profile and confuses the effects of numerical and physical viscosities.

Since the first-order scheme leads to smooth shock profiles, it is natural to construct a second-order scheme which switches automatically and smoothly to a first-order approximation in narrow shock regions. This self-adjusting hybrid scheme of Harten and Zwas[18] posseses the merits of both first and second order schemes, producing nonoscillatory shock transitions and more accurate results in smooth

regions. Later, Harten[19] developed an artificial compression method used in conjunction with the hybrid scheme. By introducing artificial compression fluxes in the conservation equations, the smeared transition regions containing either shocks or contact discontinuities are sharpened.

Characteristics-Embedded Non-Conservative Difference Scheme. Numerical schemes in this category solve hyperbolic equations in the non-conservative quasi-linear form (4.2.3), rather than (4.2.2), using characteristic information. As an example, we consider the famous Courant-Isaacson-Rees scheme[20] for a simple scalar wave equation.

$$\frac{\partial u}{\partial t} + \lambda \frac{\partial u}{\partial x} = 0 \tag{4.2.8}$$

which implies that u is conserved along the characteristic line $dx/dt=\lambda$. Construction of a stable finite difference approximation to (4.2.8) depends on the direction of the characteristics. If λ is positive, the signal propagates downstream, and the spatial derivative should be replaced by a backward difference according to the domain of influence of signal propagation. Similarly, a forward difference is used for negative λ. The finite difference equation is thus written as follows.

$$u_i^{j+1} = u_i^j - \lambda \frac{\Delta t}{\Delta x}(u_i^j - u_{i-1}^j), \quad \lambda > 0 \tag{4.2.9}$$

$$u_i^{j+1} = u_i^j - \lambda \frac{\Delta t}{\Delta x}(u_{i+1}^j - u_i^j), \quad \lambda < 0 \tag{4.2.10}$$

This scheme is also known as the first upwind (directional biased) difference method. For convenience, (4.2.9) and (4.2.10) are combined into a single equation for arbitrary values of λ,

$$u_i^{j+1} = u_i^j - \frac{\Delta t}{\Delta x}\lambda^+(u_i^j - u_{i-1}^j) - \frac{\Delta t}{\Delta x}\lambda^-(u_i^{j+1} - u_i^j) \tag{4.2.11}$$

where

$$\lambda^+ = \frac{\lambda + |\lambda|}{2}, \quad \lambda^- = \frac{\lambda - |\lambda|}{2}, \quad \text{and} \quad \lambda = \lambda^+ + \lambda^-$$

If λ is positive, then $\lambda = \lambda^+$ and $\lambda^-=0$; the above equation turns exactly out to be (4.2.9). Similarly, (4.2.10) is recovered for $\lambda < 0$ by setting $\lambda = \lambda^-$ and $\lambda^+ = 0$. Therefore, we have successfully split the eigenvalue into two parts: λ^+ and λ^-. This splitting technique provides an automatic switch determining proper difference approximation.

The same idea can be applied to a system of equations. For hyperbolic problems, there exists a similarity transformation such that the Jacobian matrix A of (4.2.3) may be decomposed as

$$A = Q\Lambda Q^{-1} \tag{4.2.12}$$

where Λ is a diagonal matrix with the eigenvalues as its elements, and Q is an orthogonal matrix containing the eigenvectors.[21] Following the same procedure as for the scalar equation, we split the diagonal matrix into two parts,

$$\Lambda = \Lambda^+ + \Lambda^- \tag{4.2.13}$$

where

$$\Lambda^+ = \text{diag}(\lambda_i^+) = \text{diag}(\frac{\lambda_i + |\lambda_i|}{2}), \quad \text{and} \quad \Lambda^- = \text{diag}(\lambda_i^-) = \text{diag}(\frac{\lambda_i - |\lambda_i|}{2})$$

Substituting (4.2.12) and (4.2.13) into (4.2.3) and employing the homogeneity property of the flux vector G (4.2.4), we obtain the following coefficient matrix- and flux-splitting equations:

$$\frac{\partial F}{\partial t} + A\frac{\partial F}{\partial x} = \frac{\partial F}{\partial t} + Q(\Lambda^+ + \Lambda^-)Q^{-1}\frac{\partial F}{\partial x}$$

$$= \frac{\partial F}{\partial t} + A^+\frac{\partial F}{\partial x} + A^-\frac{\partial F}{\partial x} \tag{4.12.14}$$

$$= \frac{\partial F}{\partial t} + \frac{\partial G^+}{\partial x} + \frac{\partial G^-}{\partial x} \tag{4.12.15}$$

Upwind finite difference schemes based on (4.2.14) and (4.2.15) have been recently developed by Chakravarthy et al[22] and Steger and Warming[23]. Note that the Courant-Isaacson-Rees type scheme satisfies the conservation law only if the eigenvalue λ remains the same sign. When the signal reaches such position at which the eigenvalue changes sign, the conservation law is violated and the entire problem becomes very cumbersome. This deficiency may be corrected with the use of a second upstream difference method averaging the eigenvalues on both sides.

Characteristics-Embedded Conservative Difference Scheme. A finite difference scheme accommodating merits of both characteristics and conservation laws seems to be most desirable; it provides shock-capturing capability and preserves the domain of influence of signal propagation. Attempts to construct such a unified scheme are subjects of current research in computational fluid dynamics.

As an example, we present the upwind flux difference splitting method of Yang, Lombard, and Bershader[24] here. Instead of dealing with (4.2.2) or (4.2.3) directly, they considered the following equation.

$$\frac{\partial F}{\partial t} + \hat{A}\frac{\partial G}{\partial x} = 0 \tag{4.2.16}$$

where $\hat{A}$ is the identity matrix and can be regarded as the normalized Jacobian matrix A of (4.2.3). By using the orthogonality property of Q, $\hat{A}$ is split into two parts,

$$\hat{A} = Q(\hat{\Lambda}^+ + \hat{\Lambda}^-)Q^{-1} = \hat{A}^+ + \hat{A}^- \tag{4.2.17}$$

where $\hat{\Lambda}^{\pm}$ = diag($\hat{\lambda}_i^{\pm}$), i=1,2,3, whose element $\hat{\lambda}_i^{\pm}$ is the normalized eigenvalue defined as

$$\hat{\lambda}_i^{\pm} = \begin{cases} \lambda^{\pm}{}_i/\lambda_i & \text{if } \lambda_i \neq 0 \\ 1/2 & \text{if } \lambda_i = 0 \end{cases} \tag{4.2.18}$$

Substitution of (4.2.17) into (4.2.16) leads to

$$\frac{\partial F}{\partial t} + \hat{A}^+ \frac{\partial G}{\partial x} + \hat{A}^- \frac{\partial G}{\partial x} = 0, \tag{4.2.19}$$

The equation is then solved with a upwind difference scheme.

To date, most characteristics-embedded finite difference schemes using splitting techniques are first-order accurate and have not been tested for various problems. Recent numerical experiments of the shock tube problem[24,25] have indicated that while the shock transition is handled remarkably well, these schemes gave rather smeared-out solutions in regions containing contact discontinuities. Consequently, they do not seem promising for the present work.

4.2.3 Dissipation, Stability and Convergence

When the solution of a partial differential equation is approximated by a finite number of data points, errors associated with discretization are inherently embedded. This phenomenon can be explained easily by making the discrete Fourier transformation of the unknown variables with respect to spacial coordinates, in which the number of frequency components is determined by that of computational meshes.[26] For a physical process reqiring a wide range of frequencies to describe it, such as strong gradients or jump discontinuities, the band-limited approximation generates errors which may grow very fast and finally cause numerical instability. To circumvent this aliasing problem, the scheme must accommodate some sort of dissipative mechanism such that the high frequency noise is effectively damped out

while preserving the convergent low frequency approximation. A scheme of this type is said to be stable. The concept of dissipative stable approximation is important even for smooth solutions since the rounding error propagates effectively with high frequency components.[27]

In practice, as a consequence of nonlinearity and complexity of the problem, a rigorous stability analysis is formidable. The stability criterion is therefore usually based on the homogeneous quasi-linear equation (4.2.3) in which the coefficient matrix A is further treated to be constant by "freezing" the local flow variables.[28] The stability of a difference operator with constant coefficients is easily ascertained by using the Fourier transform. In that representation, the difference approximation to (4.2.3) can be written as

$$F(x,t+\Delta t) = \Theta F(x,t) \tag{4.2.19}$$

where Θ is called the augmentation, or amplification, matrix containing the Fourier components of the difference operator and the elements of the coefficient matrix A. The scheme is stable in the sense that the eigenvalues of Θ do not exceed $1+O(\Delta t)$ in absolute value. This is the well-known von Neumann condition of stability.[28]

On the other hand, Courant, Friedrich, and Lewy[29] have observed that the necessary condition for stability requires that the value of $\Delta x/\Delta t$ be greater than the largest eigenvalue of the problem. This is written in the present case as

$$\Delta t \leq \frac{\Delta x}{|u| + a} \tag{4.2.20}$$

Several other stability analyses have been proposed, but few of them gave stricter explicit conditions than these two methods.

The stability analyses cited above are incomplete; they do not include the inhomogeous part of the equation. In many cases, a stable scheme for the homogeous equation may become unstable if the inhomogeous part is accounted for.

Unfortunately, an investigation of such a phenomenon is extremely complicated. Hicks[30] therefore suggested disregarding the study of stability criteria and proceeding to the heart of the problem, the convergence. A finite difference approximation must approach the solution of the original differential equation, and stability then becomes of secondary interest.

For a complicated problem, numerical convergence may be tested by changing the mesh sizes and boundary conditions. In all these tests, the solutions should be bounded and checked with available analytic solutions. Furthermore, a subroutine is always suggested to be built in the program to examine the balances of the conserved flow quantities.

4.2.4 Self-Adjusting Hybrid Scheme with Artificial Compression

As mentioned earlier, the self-adjusting hybrid scheme of Harten and Zwas[18] allows first-order monotonic shock transition and preserves higher-order accuracy in the smooth region. Because of its accommodation of steep-fronted waves and capability of capturing shocks, this scheme is particularly suitable for treating combustion instability problems.[31] It is therefore selected as the primary numerical scheme in the present application.

Mathematically, the scheme can be expressed as follows.

$$F_i^{j+1} = [\vartheta_i L_1 + (1-\vartheta_i)L_2]F_i^j, \quad 0 \le \vartheta_i \le 1 \tag{4.2.21}$$

where L_1 is a nonoscillatory first-order accurate scheme and L_2 is a second- or higher-order accurate scheme. The scalar quantity ϑ_i is called the automatic switch which senses the presence of strong gradients and has value close to unity at discontinuities. If we choose Lax's staggered scheme[32] for L_1 and the two-step Lax-Wendroff scheme[13] for L_2, then the finite difference approximation to (4.2.1) becomes

predictor

$$\tilde{F}_i^{j+1} = \frac{1}{2}[F_{i+1}^j + F_i^j] + \frac{\Delta t}{2}[Z_{i+1}^j + Z_i^j] - \frac{\Delta t}{2\Delta x}[G_{i+1}^j - G_i^j] \tag{4.2.22}$$

corrector

$$F_i^{j+1} = F_i^j + \frac{\Delta t}{2}[\tilde{Z}_i^{j+1} + \tilde{Z}_{i+1}^{j+1}] - \frac{\Delta t}{\Delta x}[\tilde{G}_i^{j+1} - \tilde{G}_{i-1}^{j-1}]$$

$$+ \frac{1}{8}[\vartheta_i(F_{i+1}^j - F_i^j) - \vartheta_{i-1}(F_i^j - F_{i-1}^j)] \tag{4.2.23}$$

The stability criterion for the first order scheme L_1 is

$$\max(|u|+a)\frac{\Delta t}{\Delta x} \leq \frac{\sqrt{3}}{2} \tag{4.2.24}$$

This is stricter than the Courant-Friedrich-Lewy condition[29] for the second order scheme L_2. Therefore, (4.2.24) determines the stability condition for the hybrid scheme.

Within this framework, the automatic switch ϑ_i is specified by requiring (1) sensitivity to shock discontinuity; (2) monotonicity in shock region; (3) preservation of high order accuracy in smooth region; and (4) satisfaction of conservation laws. There are many possible choices for ϑ_i; that used in reference 18 is chosen here. Define

$$\hat{\vartheta}_i = 0 \quad \text{if } |\rho_{i+1}^j - \rho_i^j| + |\rho_i^j - \rho_{i-1}^j| < \varepsilon$$

$$= \frac{|\rho_{i+1}^j - \rho_i^j| - |\rho_i^j - \rho_{i-1}^j|}{|\rho_{i+1}^j - \rho_i^j| + |\rho_i^j - \rho_{i-1}^j|}, \quad \text{otherwise} \tag{4.2.25}$$

, and the switch ϑ_i is

$$\vartheta_i = \max(\hat{\vartheta}_i, \hat{\vartheta}_{i+1}) \tag{4.2.26}$$

With the use of a first order scheme the numerical results are smeared out in regions containing discontinuities. This drawback is remedied by applying artificial

compression fluxes locally. Consequently, the finite difference approximation (4.2.23) is modified as

$$F_i^{j+1} = (F_i^{j+1})^* - \frac{\Delta t}{2\Delta x}(\vartheta_i^j \hat{G}_i^j - \vartheta_{i-1}^j \hat{G}_{i-1}^j) \qquad (4.2.27)$$

The superscript asterisk denotes the result obtained from the original hybrid scheme and $\hat{G}$ is a function of the artificial flux defined in reference 16. Note that the artificial compression method is inherently limited to nonoscillatory first order schemes; extension to higher order schemes yields physically unacceptable results.

The overall calculation procedure of the scheme is given in Figure 4.2.

REFERENCES 4

1. Hussein, G. A., Tasuja, A. K., Fletcher, R. S., "Effect of Air, Liquid and Injector Geometry Variables upon the Performance of a Plain-Jet Airblast Atomizer," *6th International Symposium on Air Breathing Engines*, June 1983.

2. Dickerson, R. A. and Schuman, M. D., *Journal of Spacecraft*, Vol.2, 1956, pp.99-

3. Liepmann, H. W. and Roshko, A., *Elements of Gasdynamics*, 1956.

4. Carlson, D. J. and Hoglund, R. F., "Particle Drag and Heat Transfer in Rocket Nozzles," *AIAA Journal*, Vol.2, November 1964, pp.1980-84.

5. Levine, J.N. and Culick, F.E.C., "Nonlinear Analysis of Solid Rocket Combustion Instability," *AFRPL Technical Report TR-74-45*, 1974.

6. Chen, D. Y., Yang, V., and Kuo, K. K., "Boundary Condition Specification for Mobile Granular Propellant Bed Combustion Processes," *AIAA Journal*, Vol. 19, Nov.1981, pp.1429-1437.

7. Abbett, M. J., "Boundary Condition Calculation Procedures for Inviscid Supersonic Flow Fields," *AIAA Computational Fluid Dynamic Conference*, 1973.

8. Yang, V., Private Communication with F. E. C. Culick, October 1983.

9. Roe, P. L., "An Introduction to Numerical Methods Suitable for the Euler Equations," *von Karman Institute for Fluid Dynamics, Lecture Series*, 1983-01, 1983.

10. Whitham, G. B., *Linear and Nonlinear Waves*, John Wiley and Sons, Inc., 1974.

11. Oleinik, O. A., "Discontinuous Solutions of Nonlinear Differential Equations," *American Mathematics Society, Translation (2)*, Vol.26, 1963, pp.95-172.

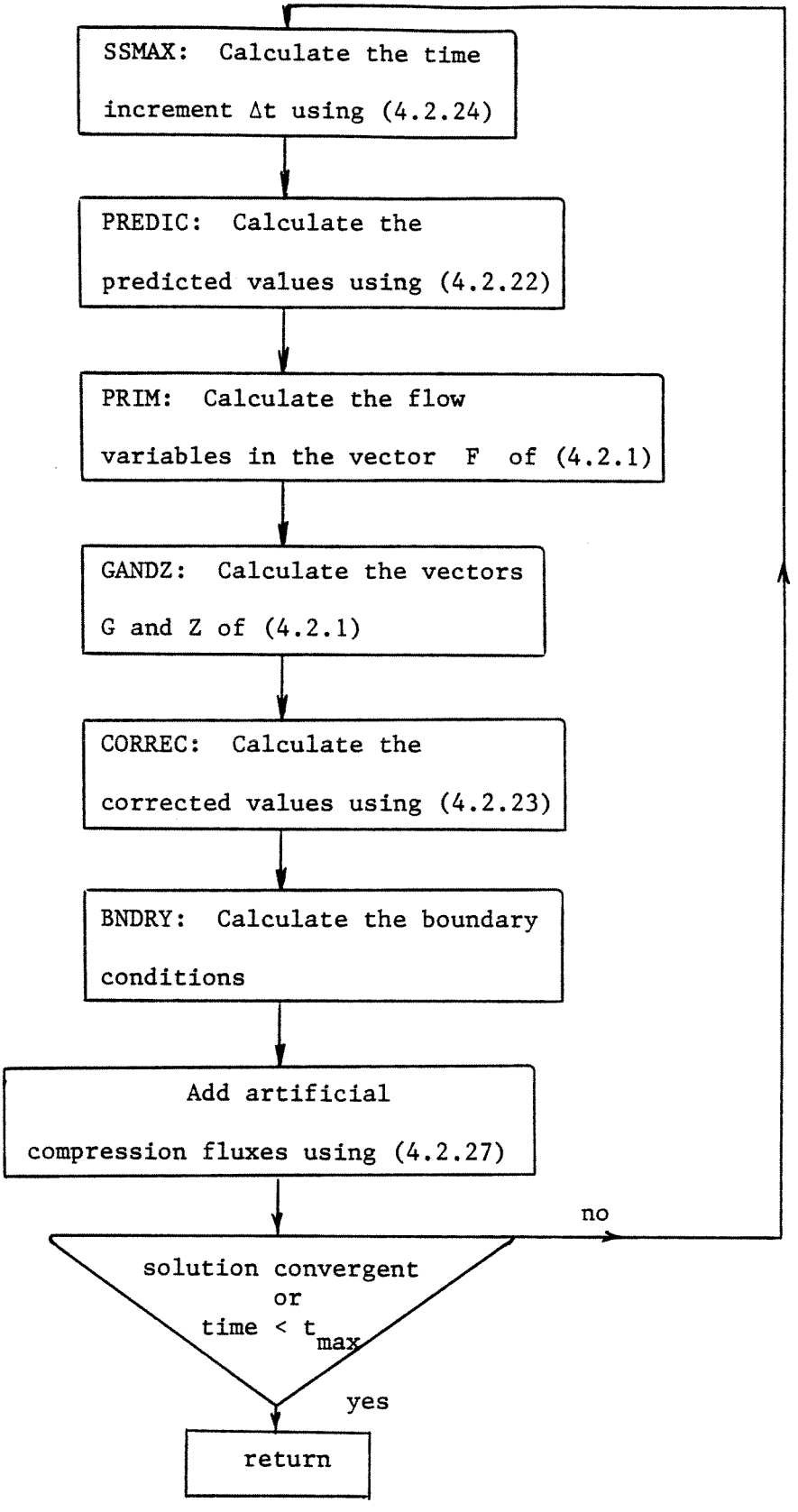

FIGURE 4.2. Flow Chart of Self-Adjusting Hybrid Scheme with Artificial Compression

12. Harten, A., Lax, P. D. and van Leer, B., "On Upstream Differencing and Godunov Type Schemes for Hyperbolic Conservation Law," *ICASE Report No 82-5*, 1982.

13. Lax, P. D. and Wendroff, B., "Systems of Conservation Laws," Communication of Pure and Applied Mathematics," Vol.13, 1960, pp.-217-237.

14. Levine, J. N. and Culick, F. E. C., "Numerical Analysis of Nonlinear Longitudinal Combustion Instability in Metalized Propellant Solid Rocket Motors, Vol.1, Analysis and Results," *AFRPL Technical Report TR-72-88*, July 1972.

15. Vreugdenhill, C. B., "On the Effect of Artificial Viscosity Methods in Calculating Shocks," *Journal of Engineering Mathematics*, Vol.3, 1963, pp.285-288.

16. von Neumann, J. and Richtmyer, R. D., "A Method for the Numerical Calculation of Hydrodynamic Shocks," *Journal of Applied Physics*, Vol.21, 1950, pp.232-237.

17. Lapidus, A. *Journal of Computational Physics*, Vol.2, 1967, p.154-

18. Harten, A. and Zwas, G., "Self-Adjusting Hybrid Schemes for Shock Computations," *Journal of Computational Physics*, Vol.9, 1972, pp.568-583.

19. Harten, A., "The Artificial Compression Method for Computation of Shocks and Contact Discontinuities: III, Self Adjusting Hybrid Schemes," *AFOSR Technical Report TR-77-0659*, 1977.

20. Courant, R., Issscson, E., and Rees, M., "On the Solution of Nonlinear Hyperbolic Differential Equations by Finite Differences," *Communication of Pure and Applied Mathematics*, Vol.5, 1952, pp.243-255.

21. Ames, W. F., *Numerical Methods for Partial Differential Equations*, Academic Press, Inc., 1977.

22. Chakravarthy, S. R., Anderson, D. A., and Salas, M. D., "The Split Coefficient Matrix Method for Hyperbolic Systems of Gas Dynamic Equations," *AIAA Paper 80-0268*, 1980.

23. Steger, J. L. and Warming, R. F., "Flux Vector Splitting of Inviscid Gasdynamic Equations with Application to Finite Difference Methods," *NASA Technical Memorandum 78605*, July 1979.

24. Yang, J. Y., Lombard, C. K., and Bershader, D., "A Characteristic Flux Difference Splitting for the Hyperbolic Conservation Laws of Inviscid Gasdynamics," *AIAA Paper 83-0040*, 1983.

25. Sod, G. A., "A Survey of Several Finite Difference Methods for Systems of Nonlinear Hyperbolic Conservation Laws," *Journal of Computational Physics*, Vol.27, 1978, pp.1-31.

26. Roache, P. J., *Computational Fluid Dynamics*, Hermosa Publishers, Inc., 1972.

27. Kreiss, H. and Oliger, J., "Methods for the Approximate Solution of Time Dependent Problems," *GARP Publications Series No.10*, February 1973.

28. Richtmyer, R. D. and Morton, K. W., 'Difference Methods for Initial-Value Problem," *Interscience Publishers, Inc.*, 2nd edition, 1969.

29. Courant, R., Friedrichs, K. O., and Lewy, H., 'Ueber die Partielien Differenzgleichungen der Mathematischen Physik," *Math. Ann.*, Vol.100, 1928, pp.32-74.

30. Hicks, D. L., "One-Dimensional Lagrangian Hydrodynamics and IDLH Hydrocode," *Sandia Laboratories, SC-RR-69-729*, 1969.

31. Baum, J. D. and Levine, J. N., 'Evaluation of Finite Difference Schemes for Solving Nonlinear Wave Propagation Problems in Rocket Combustion Chambers," *AIAA Paper No. 81-0420*, 1981.

32. Lax, P. D., 'Weak Solutions of Nonlinear Hyperbolic Equations and Their Numerical Computations," *Communication of Pure and Applied Mathematics*, Vol.7, 1954, pp.159-193.

NOMENCLATURE 4

A	cross-sectional area
A_s	specific surface area of droplets
c_l	specific heat of fuel
c_p	constant pressure specific heat of air
d_p	diameter of droplet
d_{jo}	diameter of fuel injector port
F_p	drag force between air and fuel droplets
h	enthalpy
M	Mach number
$\dot{m}_{k,i}$	rate of consumption of ith species
p	pressure
P_r	Prandtl number
Q_p	heat transfer rate between air and fuel droplets
r_b	surface regression rate of droplet
r_p	radius of droplet
R_{ei}	Reynolds number based on relative flow velocity
t	time
T	temperature
u	velocity
V_a	air flow velocity

x	position coordinate along the axis of the engine, normalized w.r.t. the inlet length
Y_i	mass fraction of ith species
γ	ratio of specific heats
μ	viscosity
$\dot{\omega}_f$	rate of consumption of fuel in the stirred reactor
ω_g	rate of air injected into the main flow
ω_p	rate of liquid fuel injected into the main flow
ρ	density
ρ_l	density of liquid fuel
σ_l	surface tension of liquid fuel
ΔH	heat of combustion per unit mass of fuel

superscript

$( )^*$	dimensional quantity

subscripts

f	fuel
o	oxidizer
p	liquid phase
ref	reference quantity
sg, sp	values at port of fuel injector

Chapter 5

ANALYSIS OF UNSTEADY DIFFUSER FLOW WITH A SHOCK WAVE

Unsteady inlet diffuser flow with a shock wave has received considerable attention in recent investigations of longitudinal combustion instabilities in ramjet engines.[1] As a consequence of pressure fluctuations generated by combustion processes, the stability margin of the inlet diffuser may be reduced due to perturbations of the shock system. In this chapter, a finite difference scheme with a shock-fitting algorithm is used to study unsteady behavior of the inlet flow. The formulation is directed specifically to obtaining results required in analysis of unsteady motions in engines.

In a continuing experimental program, Sabjen and coworkers have reported[2,3,4] extensive, detailed observations in the transonic range. They have summarized the features of the flow fields under various conditions. Both self-sustaining and mechanically induced oscillations were investigated. Schadow et al examined[5] oscillations in a research dump combustor with special attention focused on the inlet shock/acoustic wave interaction. Two kinds of data have been taken: the acoustic wave structure and the characteristics of the inlet shock.

Several analyses of the problem have been carried out. Adamson et al[6] obtained systematic solutions for large amplitude shock wave motion in a two-dimensional transonic flow, using methods of matched asymptotic expansions. The same approach was later extended to include boundary layer displacement effects,[7] and shock wave/boundary layer interaction.[8] In references 9 and 10, numerical solutions of Navier-Stokes equations for multi-dimensional transonic/supersonic flows were reported. The detailed information obtained provides a better understanding of the flowfields, especially under conditions when flow separation occurs.

For linear stability analysis of unsteady motions in an engine, the boundary condition at the upstream end of the diffuser is conveniently expressed as the admittance function of a normal shock wave. Culick and Rogers[11] analyzed the problem of small amplitude motions of a normal shock in one-dimensional flow. Results for the admittance function were given for two cases: inviscid flow, and a case which might be regarded as a crude approximation to the influences of separation. The work reported here begins with essentially the same model of the flow, but with the numerical analysis results can be obtained for finite and large amplitude motions. In addition, the effects of viscous boundary layers are accounted for.

Both inviscid and viscous cases are accommodated. As a first approximation, the gas flow is assumed to be inviscid. Figure 5.1 shows the idealized inlet system considered, consisting of a convergent-divergent channel and a fuel injection system. Air is delivered to a diffuser, becomes sonic at the throat, then accelerates supersonically in the divergent section. After passing through a normal shock wave, the flow becomes subsonic and decelerates to the exit, which may represent the inlet/combustor interface. Either fuel or fuel-air mixture, depending on the injector and atomizer used, is injected into the main flow downstream of the shock to provide the necessary combustible mixture. Within this representation, interaction between the inlet and combustor may be visualized as follows. Unsteady combustion generates a pressure wave propagating upstream and causes the shock to oscillate about its mean position. As a consequence, the induced shock motion produces fluctuations of entropy and mass flow rate, which, together with the reflected pressure wave, may augment or attenuate the initial disturbance.

To make the model more realistic, viscous effects in the boundary layers are included. For longitudinal oscillations at relatively low frequencies, the boundary layer behavior can be considered quasi-steady. The flow therefore consists of a one-dimensional unsteady inviscid core flow coupled to a two-dimensional steady

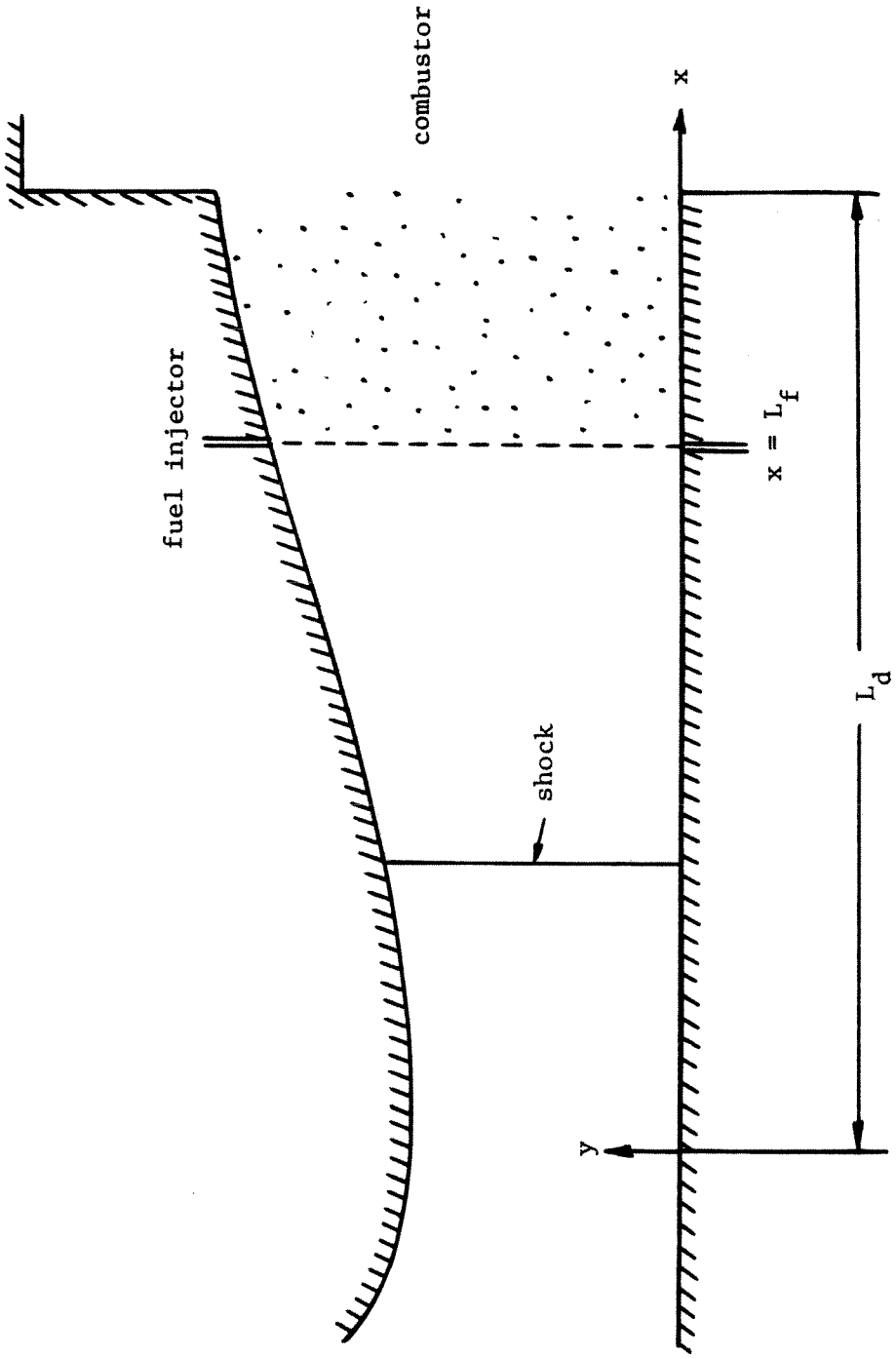

FIGURE 5.1. Schematic Diagram of Inlet Diffuser

viscous boundary layer. The wall boundary layer is assumed to be turbulent and attached, and represented with Green's lag-entrainment method.[12] A simple phenomenological model modified from reference 13 is used to treat the complicated shock wave/boundary layer interactions. By using theoretical and experimental informations, the viscous displacement surface in the vicinity of the shock may be described. Combination of this viscous ramp model with boundary layer analysis completes the theoretical formulation.

The specific objectives of this chapter are

1. to study the response of a normal shock wave to various disturbances;
2. to analyze the changes of flow properties, such as entropy and mass flow rate, due to shock motion;
3. to examine the influences of liquid fuel droplets and wall air jet injected downstream of the shock wave;
4. and to investigate the effects of viscous boundary layers on the flowfield.

The coupling between the inlet and processes in the combustion chamber are not treated here.

5.1 Formulation

The flowfields in the inviscid core and the viscous boundary layer regions are treated separately. This approach has the advantage of reducing the governing Navier-Stokes equations to a set of one-dimensional Euler equations coupled to a set of two-dimensional boundary layer equations by including only those terms which influence the fluid dynamic processes in each region.

5.1.1 Analysis of Core Flow

The core flow consists of three different regions shown in Figure 5.1: the regions upstream and downstream of a normal shock wave, and a region containing both air and fuel droplets. The fuel droplets are assumed to have uniform size and to be distributed over the entire cross-sectional area, the initial phase of fuel jet break-up and multi-dimensional effects being ignored. For some systems, preparation of fuel droplets may be achieved outside the diffuser. In that case, a mixture of air and fuel, rather than pure fuel, is injected into the main stream. Both cases are accommodated here.

The analysis is based on a two-phase, quasi one-dimensional model. If we neglect droplet vaporization, the equations governing the gas flow can be expressed in the following conservation form, displayed earlier as (4.1.18-20) in Chapter 4.

gas phase

$$\frac{\partial \rho}{\partial t} + \frac{1}{A_c}\frac{\partial(\rho u A_c)}{\partial x} = \omega_g \tag{5.1.1}$$

$$\frac{\partial(\rho u)}{\partial t} + \frac{1}{A_c}\frac{\partial}{\partial x}\left[\left(\frac{p}{\gamma} + \rho u^2\right)A_c\right] = \frac{p}{\gamma A_c}\frac{dA_c}{dx} + F_p + u_{sg}\omega_g \tag{5.1.2}$$

$$\frac{\partial}{\partial t}\left[\rho\left(\frac{T}{\gamma(\gamma-1)} + \frac{u^2}{2}\right)\right] + \frac{1}{A_c}\frac{\partial}{\partial x}\left[\rho u A_c\left(\frac{T}{\gamma(\gamma-1)} + \frac{u^2}{2}\right)\right]$$

$$= \frac{-1}{\gamma A_c}\frac{\partial(upA_c)}{\partial x} + \omega_g\left(\frac{T_{sg}}{\gamma-1} + \frac{u_{sg}^2}{2}\right) + \frac{Q_p}{\gamma-1} + u_p F_p \tag{5.1.3}$$

Since the droplets are dispersed and injected downstream of the shock, no wave-like motion may exist in the liquid flow. The governing equations are thus solved conveniently in the non-conservation form.

liquid phase

$$\frac{\partial \rho_p}{\partial t} + \frac{\partial(\rho_p u_p)}{\partial x} = \omega_p - \frac{\rho_p u_p}{A_c}\frac{dA_c}{dx} \tag{5.1.4}$$

$$\frac{\partial u_p}{\partial t} + u_p\frac{\partial u_p}{\partial x} = -\frac{F_p}{\rho_p} \tag{5.1.5}$$

$$\frac{\partial T_p}{\partial t} + u_p\frac{\partial T_p}{\partial x} = -\frac{Q_p}{\rho_p c_l} \tag{5.1.6}$$

where A_c is the cross sectional area of the inviscid core, obtained by reducing the geometric duct area by the boundary layer displacement thickness. The flow properties are normalized with respect to their quantities at the entrance except the velocity which is referenced to the speed of sound. Note that the mass source terms ω_g and ω_p are introduced only at the injector position ($x=L_f$), and the momentum and heat transfer coupling terms F_p and Q_p vanish in regions I and II.

5.1.1.1 Specification of Boundary Conditions

In order to solve this problem, three boundary conditions must be specified at both boundaries for each phase. Depending on the amplitude of shock motion, the upstream boundary is chosen to be either the entrance or the throat of the diffuser. For most cases of finite amplitude oscillations, the shock motion is restricted to the divergent section of the diffuser. The flow remains always sonic at the throat; no signal can propagate through it from the downstream region. Therefore, it is convenient to choose the throat as the upstream boundary. The boundary conditions are then determined by specifying three physical quantities, the Mach number, static pressure and temperature, since there is no characteristic line running from the interior region to the boundary.

Under certain conditions the shock moves upstream of the throat, disappearing as the pressure increases, and then rapidly reappears at its farthermost down-

stream position as the pressure reaches minimum amplitude. This sort of behavior has been observed in recent experiments,[5] referred to as the large amplitude oscillation case in the present work. The upstream boundary is chosen to be the inlet entrance with three conditions obtained by assuming conservation of total energy and isentropic process from a reservoir upstream to the inlet, together with the leftward characteristic equation. Within this assumption, the reservoir serves essentially as a perfect acoustic energy absorber. Any disturbance radiated from the entrance is efficiently damped out. At the downstream end, the flow is subsonic. Two characteristic lines run from the interior region to the exit; only the static pressure needs to be specified.

Because the liquid droplets are dispersed, no signal can propagate through them. The governing equations change from totally hyperbolic to hyperbolic; the three characteristic lines collapse into one. This suggests using a one-sided difference for the calculation of the downstream boundary conditions for the liquid phase. The conditions at the upstream boundary ($x=L_t$) are determined from the physical requirements set by the convection of droplets downstream.

5.1.1.2 Numerical Method

The basis for the analysis is a numerical program described in Chapter 4. The conventional two-step Lax-Wendroff method is hybridized with Harten and Zwas' first order scheme and further modified by an artificial compression correction.[14,15] The spurious pre- and post-shock oscillations produced by second order finite difference approximations are completely eliminated. Because of its remarkable shock-capturing feature, the scheme is applied first to solve for steady flowfields.

For unsteady problems, direct application of that method is accompanied by two problems. First, the shock transition requires a small number of computational

grids. The flow properties immediately in front of and behind the shock are not well defined. Second, there are two time scales involved in the calculation: τ_{sh} and τ_e. τ_{sh} is the time required for a shock to pass through a grid, and τ_e is associated with an external disturbance. Unless very fine meshes are used, i.e., $\tau_{sh} << \tau_e$, the crude time resolution of shock motion may produce false information. To overcome these problems and improve numerical efficiency, a shock-fitting algorithm has been incorporated.

The shock-fitting technique[16] treats the shock as an internal boundary, separating the supersonic and the subsonic regions. The Rankine-Hugoniot equations together with four characteristic relations, three in the supersonic region and one in the subsonic region, suffice to provide the required boundary conditions for the finite difference scheme on each side. The motion of the shock front is determined as part of the solution.

The numerical calculation starts with application of the self-adjusting hybrid scheme. As soon as the shock is captured and reaches its steady condition, the shock-fitting algorithm is activated to refine the solution. This has proved to be an effective procedure, producing accurate results with modest costs.

5.1.2 Turbulent Boundary Layer

The thin turbulent layers on the top and the bottom walls are formulated using Green's lag-entrainment method[12] because of its accuracy and favorable comparison with other methods. In that representation, a turbulent boundary layer is defined by three independent parameters, momentum thickness ϑ, shape factor $H=\frac{\delta^*}{\vartheta}$, and entrainment coefficient C_E, defined as follows.

displacement thickness

$$\delta^* = \int_0^\delta (1 - \frac{\rho u}{\rho_e u_e})dy \tag{5.1.7}$$

momentum thickness

$$\vartheta = \int_0^\delta \frac{\rho u}{\rho_e u_e}(1 - \frac{u}{u_e})dy \tag{5.1.8}$$

entrainment coefficient

$$C_E = \frac{1}{\rho_e u_e}\frac{d}{dx}\rho_e u_e(\delta - \delta^*) \tag{5.1.9}$$

where δ is the boundary layer thickness. The subscript e stands for values at the edge of the boundary layer, being equal to the values in the core flow. By integrating the equations of motion along y-coordinate and utilizing the equation for shear stress which Bradshaw et al[17] derived from the turbulent kinetic energy equation, three ordinary differential equations governing ϑ, H, and C_E are obtained:

momemtum integral equation

$$\frac{d\vartheta}{dx} = \frac{C_f}{2} - (H + 2 - M^2)\frac{\vartheta}{u_e}\frac{du_e}{dx} \tag{5.1.10}$$

entrainment equation

$$\vartheta\frac{d\bar{H}}{dx} = \frac{d\bar{H}}{dH_1}\{C_E - H_1[\frac{C_f}{2} - (H + 1)\frac{\vartheta}{u_e}\frac{du_e}{dx}]\} \tag{5.1.11}$$

rate of change of entrainment coefficient

$$\vartheta\frac{dC_E}{dx} = F\{\frac{2.8}{H + H_1}[(C_\tau)_{EQ}^{1/2} - \lambda C_\tau^{1/2}] + \left(\frac{\vartheta}{u_e}\frac{du_e}{dx}\right)_{EQ}$$

$$- \frac{\vartheta}{u_e}\frac{du_e}{dx}[1 + 0.075M^2\frac{(1 + 0.2M^2)}{(1 + 0.1M^2)}]\} \tag{5.1.12}$$

where M is the core flow Mach number and $\bar{H}$ is the modified shape factor.

$$\bar{H} = (H + 1)/(1 + \frac{M^2}{5}) - 1 \tag{5.1.13}$$

Detailed derivation of the above equations and additional relations for the integral properties are given in reference 12.

5.1.3 Viscous-Inviscid Interaction

The coupling between inviscid core flow and viscous boundary layers is accomplished using an iterative method. The core flow solver provides the velocity distribution at the edges of boundary layers, which is used in the calculation of boundary layer properties. The resulted displacement thickness then modifies the effective cross-sectional area of the diffuser to renew the calculation for the core flow. To ensure convergent solution and improve numerical efficiency, an under-relaxation procedure is employed. The relaxed displacement thickness δ^* in the (n+1)th iteration is

$$\delta^* = \omega_1 \cdot \delta^*_{(n+1)} + (1 - \omega_1) \cdot \delta^*_{(n)} \tag{5.1.14}$$

where the subscript n represents the nth iteration and ω_1 is the relaxation coefficient. In the present work, a value of 0.75 is suggested by trial-and-error.

In the above direct iteration procedure, the core flow velocity field is prescribed in order to determine boundary layer properties. While being straightforward, this method sometimes, especially if the flow is separated, produces a slowly convergent or even a divergent solution unless a suitable relaxation coefficient ω_1 is adopted. To overcome this problem, an inverse iteration scheme has been proposed.[18] The momentum integral equation (5.1.10) is first rewritten as

$$\frac{\vartheta}{u_e}\frac{du_e}{dx} = \frac{1}{H + 2 - M^2}\left[-\frac{d\vartheta}{dx} + \frac{C_f}{2}\right] \tag{5.1.15}$$

With the prescribed displacement thickness δ^*, the boundary layer edge velocity u_e is calculated from (5.1.15), (5.1.11) and (5.1.12). This is then used to compute an

up-dated δ^* through the equation given below.

$$\delta^*_{(n+1)} = \delta^*_{(n)} \frac{u_e}{u_{inv}} \tag{5.1.16}$$

where u_{inv} denotes the inviscid core flow velocity. The same procedure is repeated until the solution becoms convergent.

Both direct and indirect iteration procedures have been used. They all lead to convergent solutions since the boundary layer is assumed to be attached here.

5.1.4 Shock Wave/Boundary Layer Interaction

The strong interaction between a shock wave and a turbulent boundary layer involves the penetration of the shock wave into the boundary layer. As a consequence of the strong normal pressure gradient resulted from the diffraction of the shock wave by the nonuniform velocity field in the boundary layer, the conventional boundary layer approximation is not valid. The interaction may affect the flowfield both locally and globally. The principal local effect is to smear the pressure rise across the shock over a few boundary layer thicknesses. The global influence arises from the rapid increases of boundary layer properties across the shock which may significantly thicken the boundary layer thickness in the downstream region.

Several researchers have analyzed the flowfield near the shock foot using matched asymptotic expansion methods.[19,20] All these models are based on the assumption that for a transonic weak shock, the interaction can be considered as a small perturbation superimposed on the boundary layer. Favorable results were obtained in some limiting cases at the expense of complicated formulations. To simplify the analysis, an alternative phenomenological model is used here. It has proven to be useful in many engineering applications.[13,21] If the shock strength is weak and no flow separation occurs, then the thickening of the boundary layer in the interaction region can be modeled as a viscous ramp shown in Figure 5.2. The

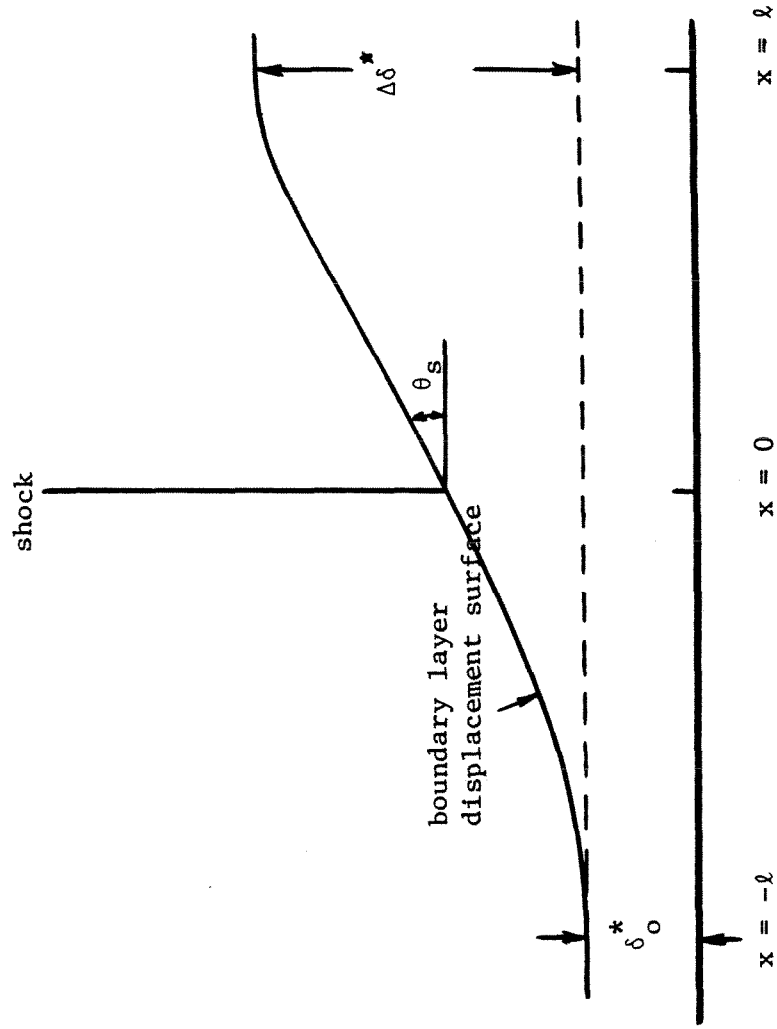

FIGURE 5.2. Viscous Ramp Model for Shock Wave/Boundary Layer Interaction

shock is located in the middle of the ramp, taking into account both the upstream and the downstream influences of the shock on the boundary layer. This feature distinguishes the present model from references 13 and 21 in which the shock is attached to the ramp apex. As shown later, the inclusion of the upstream influence is essential to obtain reasonable quantitative prediction.

Since the interaction is a local phenomenon, an appropriate length scale governing the domain of influence must be determined. By considering the non-trival solution of the transonic small perturbation equation, this scale is defined as[19]

$$\eta = \delta_0 \cdot \sqrt{M^2 - 1} \tag{5.1.17}$$

where δ_0 is the unperturbed boundary layer thickness. For a weak shock, the inclination angle of the ramp agrees roughly with the maximum deflection angle for an attached shock.[22] Thus, from the oblique shock relation we have

$$\vartheta_s = 2\cot\beta \frac{M_1^2 \sin^2\beta - 1}{M_1^2(\gamma + \cos 2\beta) + 2} \tag{5.1.18}$$

where

$$\beta = \frac{1}{2}\left[\frac{\pi}{2} + \sin^{-1}\frac{1}{M_1}\right] \tag{5.1.19}$$

A third-order polynomial is chosen to define the shape of the viscous ramp by satisfying the following conditions.

$$\delta^* = \delta_0^* \quad \text{at } x = -l \tag{5.1.20a}$$

$$\frac{d\delta^*}{dx} = 0 \quad \text{at } x = -l \tag{5.1.20b}$$

$$\frac{d\delta^*}{dx} = 0 \quad \text{at } x = l \tag{5.1.20c}$$

$$\frac{d\delta^*}{dx} = \tan\vartheta_s \approx \vartheta_s \quad \text{at } x = 0 \tag{5.1.20d}$$

Consequently,

$$\delta^* = \delta_0^* + \vartheta_s l\left[\frac{2}{3} + \left(\frac{x}{l}\right) - \frac{1}{3}\left(\frac{x}{l}\right)^3\right] \tag{5.1.21}$$

where l is of the order of magnitude of the length scale η; its actual value used in the numerical calculation depends on the displacement thickness δ^* at $x=l$.

In the limit of a transonic weak shock, the jumps in boundary layer integral properties are proportional to the pressure jump across the shock wave.[23] Therefore, the following linear variations of $\Delta\delta^*$ and $\Delta\vartheta$ with the shock strength are proposed to fit the experimental data reported in reference 24:

$$\frac{\Delta\delta^*}{\delta_0^*} = 6\left(\frac{M_1}{M_2} - 1\right) \tag{5.1.22}$$

$$\frac{\Delta\vartheta}{\vartheta_0} = 3\left(\frac{M_1}{M_2} - 1\right) \tag{5.1.23}$$

Evaluating the displacement thickness δ^* at $x=l$ from (5.1.21) and using the empirical correlation (5.1.22), one may determine the length of the interaction region.

$$l = 4.5\frac{\delta_0^*}{\vartheta_s}\left(\frac{M_1}{M_2} - 1\right) \tag{5.1.24}$$

In general, l is much smaller than the longitudinal acoustic wave length; the entire interaction region is acoustically compact. The processes in the interaction regions on both sides of the shock are therefore considered quasi-steady and isentropic since the entropy fluctuation due to the motion of a weak shock is negligibly small.

The overall calculation procedure with viscous/inviscid and shock wave/boundary layer interactions accounted for is given in Figure 5.3. The interaction module provides the necessary information for calculating the downstream flowfield. Its global role in the program is obvious.

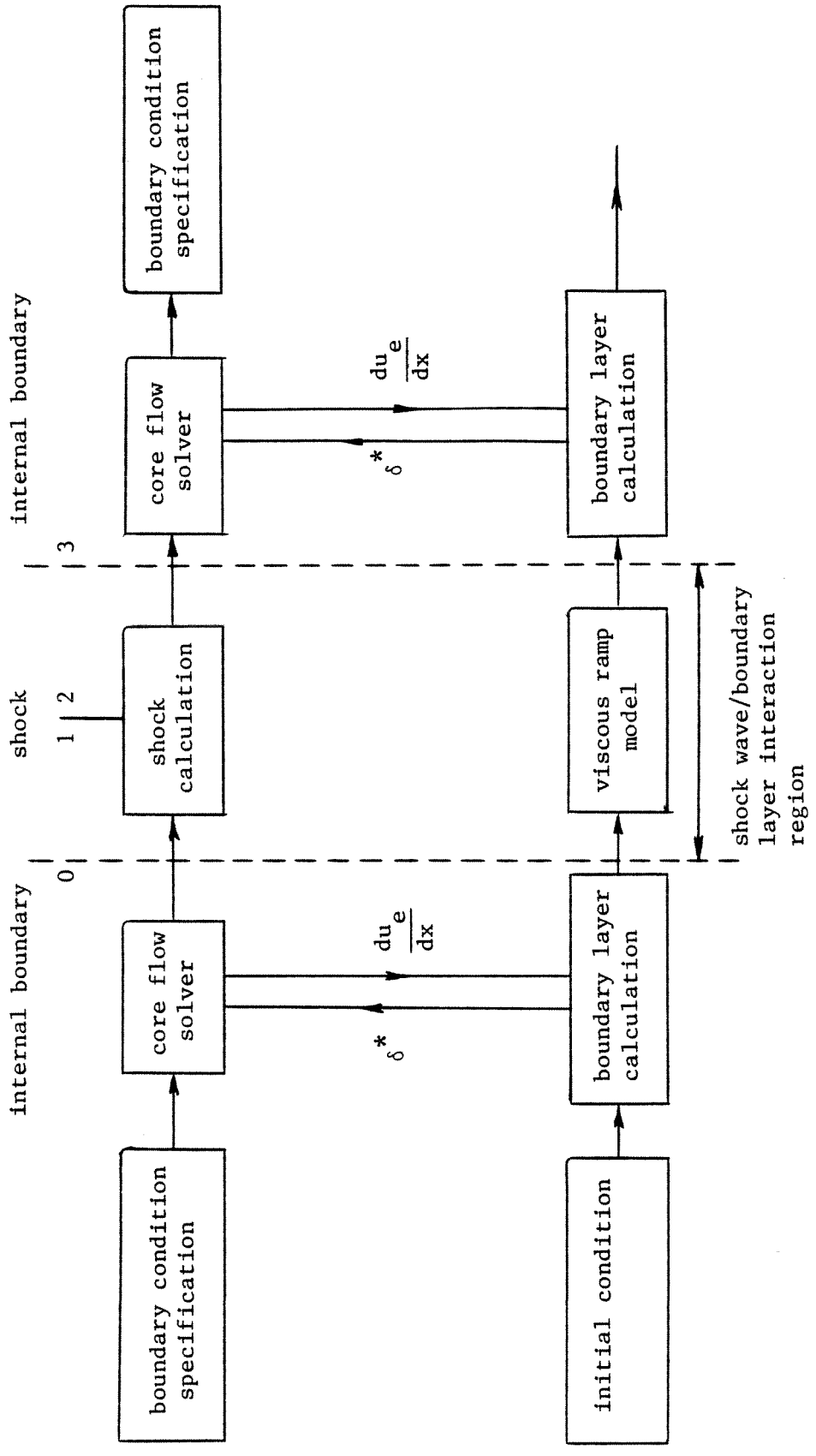

FIGURE 5.3. Overall Calculation Procedure for Unsteady Viscous Diffuser Flow with a Shock Wave

5.2 Discussion of Results

Calculations have been carried out for two different diffusers, referred to as A and B respectively. Diffuser A has a linear area distribution,

$$\frac{A(x)}{A_{in}} = 1 + k\left(\frac{x}{L_d}\right) \tag{5.2.1}$$

where L_d is the length of the diffuser from the entrance to the exit. Diffuser B is a convergent/divergent nozzle with a flat bottom and a contoured top wall, with the axial distribution of area given by the formulas:

convergent section

$$A(x) = \frac{1.4114\cosh\zeta}{0.4114 + \cosh\zeta}$$

$$\zeta = \frac{-0.81\left(\frac{x}{2.598}\right)\left[1 - \frac{x}{2.598}\right]^{0.5}}{\left[1 + \frac{x}{2.598}\right]^{0.6}} \tag{5.2.2}$$

divergent section

$$A(x) = \frac{1.5\cosh\zeta}{0.5 + \cosh\zeta}$$

$$\zeta = \frac{2.25\left(\frac{x}{7.216}\right)}{\left[1 - \frac{x}{7.216}\right]^{0.6}} \tag{5.2.3}$$

It is the baseline diffuser in reference 4. For each case, the analysis is applied first to compute the flowfield under steady conditions. The response of a shock wave to various disturbances and its associated influences on the flowfield are then examined in detail.

Figure 5.4 shows the distributions of the mean flow properties in diffuser A with

only the inviscid gas flow accounted for. The shock-fitting scheme functions well, confining the numerical error within one tenth percent. At t=0 a periodic pressure oscillation is imposed at the exit, simulating a pressure fluctuation induced by combustion instability. After the time required for the disturbance to travel upstream to the shock, the shock begins to oscillate about its mean position. The local pressure and velocity fluctuations just downstream of the shock are of course different from those existing at the exit and exhibit features due to the nonlinear behavior of the shock and the nonuniformity of the mean flowfield. Figure 5.5 shows the instantaneous position of the shock for downstream disturbances having different frequencies and amplitudes. The strong influences of frequency and amplitude on the average position is evident: lower frequency and high amplitude tend to displace the shock towards the throat, unfavorable for the performance of an inlet.

The shock response depends strongly on the local diffuser shape. Earlier work[11] has shown that the dimensionless frequency Ω, defined as follows,

$$\Omega = \frac{\omega/\bar{a}_2}{\left(\frac{1}{A}\frac{dA}{dx}\right)_{shock}} \tag{5.2.4}$$

plays an important role. As a check of the numerical analysis described here, the real and imaginary parts of the admittance function have been calculated with the results given in Figures 5.6 and 5.7. Agreement between the calculations based on the present model, applied in the limit of small amplitudes, and the earlier results from a linear analysis[11] is quite good. The response of the shock increases if Ω is decreased. According to the definition (5.2.4), this happens if the fractional change of cross-sectional area is increased . For the frequencies chosen here, the values of Ω for the two diffusers treated here are:

	300 Hz	600 Hz
A	$\Omega = 17.76$	$\Omega = 35.52$
B	$\Omega = 2.475$	$\Omega = 4.950$

Thus, one would anticipate that the shock wave in diffuser B should be more responsive. Comparison of the results shown in Figure 5.8 (diffuser B) and Figure 5.5 (diffuser A) confirms this conclusion.

5.2.1 Oscillation of Entropy

Entropy fluctuations are generated as a consequence of shock motion due to a pressure disturbance, and are convected downstream by the mean flow. These may in turn produce pressure waves when passing through a region of nonuniform velocity. From the results for temperature and pressure, the entropy fluctuations can be determined from the following thermodynamic relation:

$$\Delta s = \frac{s_2 - \bar{s}_2}{c_p} = \ln\frac{T_2}{\bar{T}_2} - \frac{\gamma - 1}{\gamma}\ln\frac{p_2}{\bar{p}_2} \tag{5.2.5}$$

The induced entropy fluctuation is usually very small except for a strong shock. For example, for diffuser A and the unsteady motions shown in Figure 5.5, the entropy response function, defined as the ratio $\Delta s/(\Delta p_2/\bar{p}_2)$, has magnitude less than 0.1.

Figure 5.9 shows the entropy distributions at various times during a cycle of oscillation in diffuser A. The distributions given include the maximum upstream and downstream excursions of the shock, and an intermediate position. The nonlinear motions are clear in the asymmetrical shapes of curves.

5.2.2 Oscillation of Mass Flow Rate

Even for a fixed mass flow rate upstream of the shock, an oscillation of mass flow will occur in the downstream region due to the shock motion. To first order

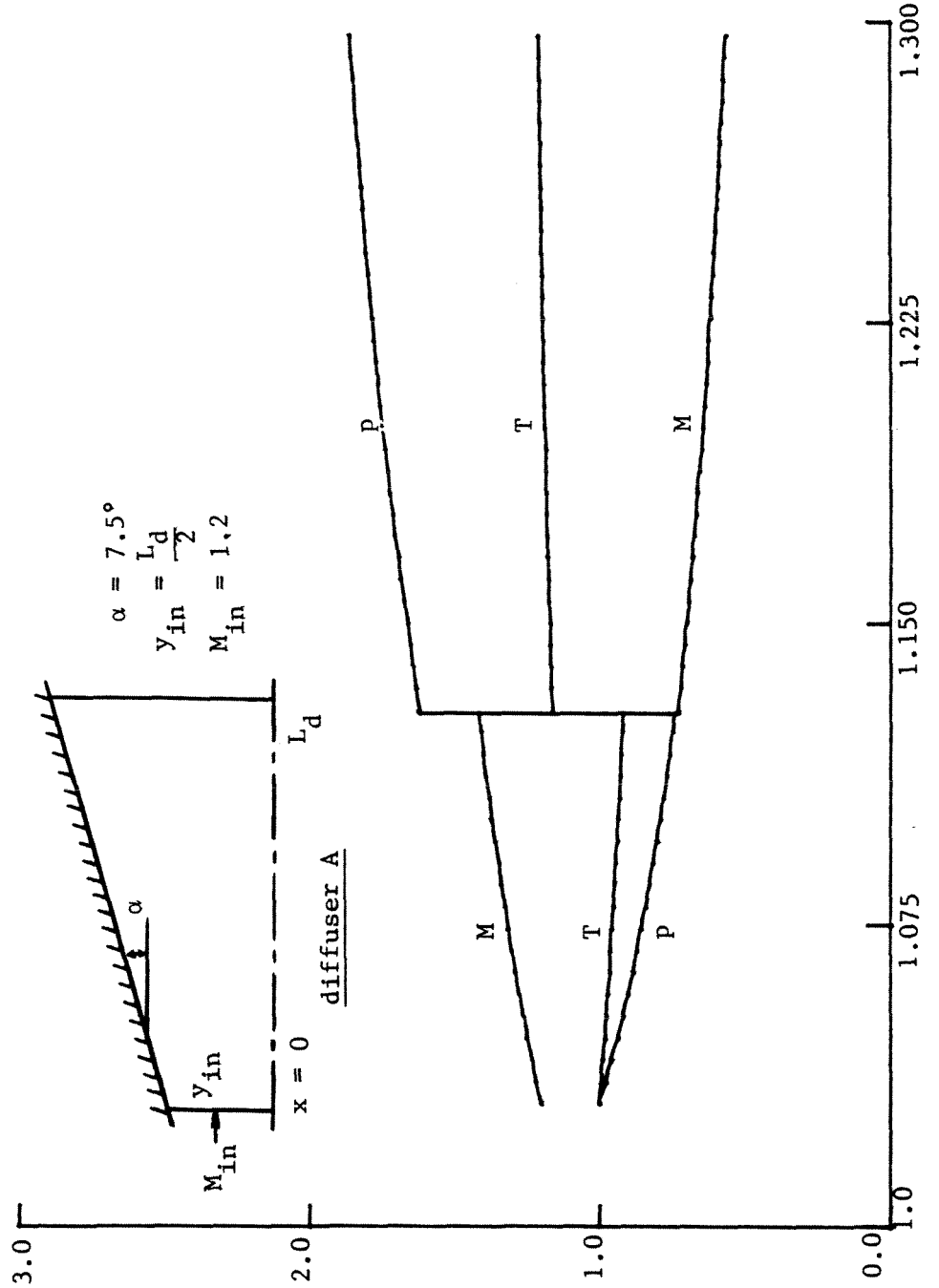

FIGURE 5.4. Distributions of Mean Flow Properties (Diffuser A)

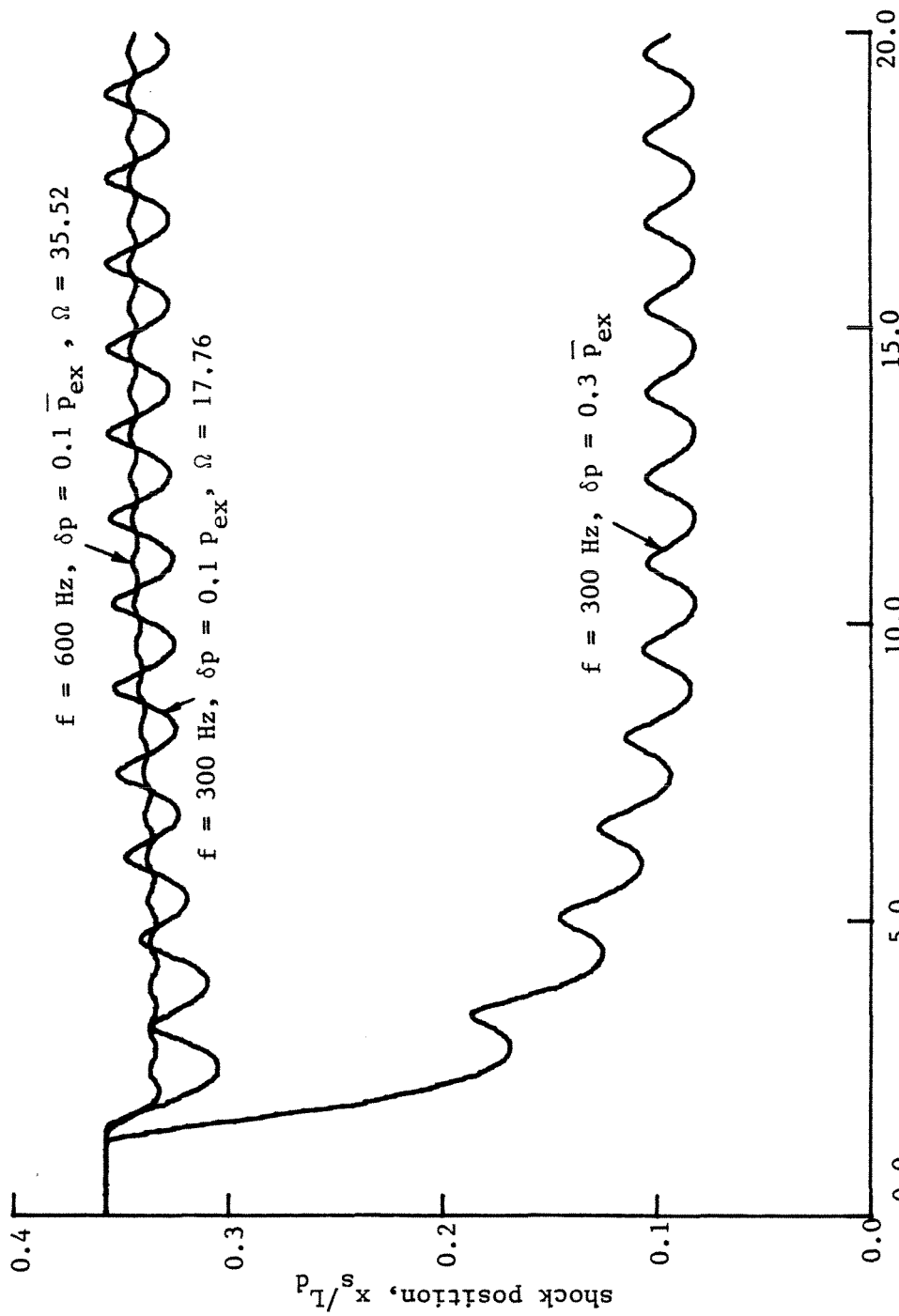

FIGURE 5.5. Instantaneous Shock Position (Diffuser A)

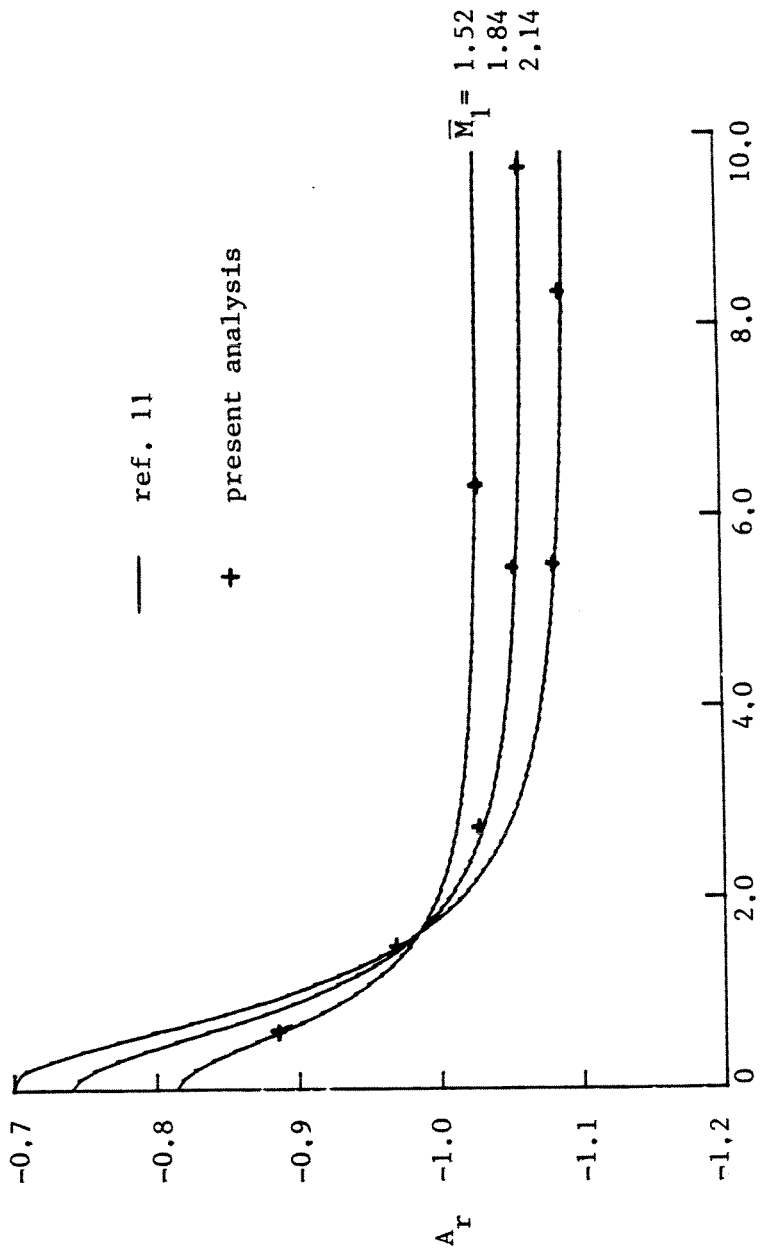

FIGURE 5.6. Real Part of Shock Admittance Function

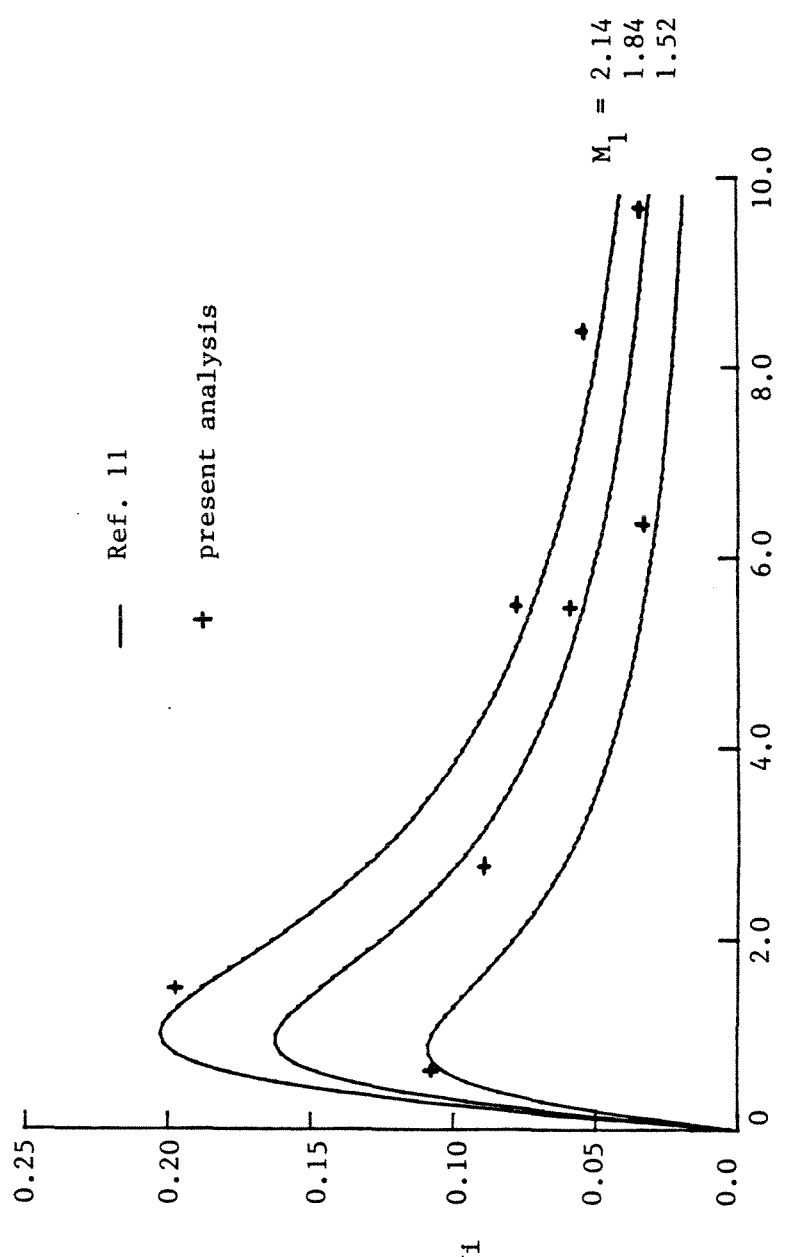

FIGURE 5.7. Imaginary Part of Shock Admittance Function

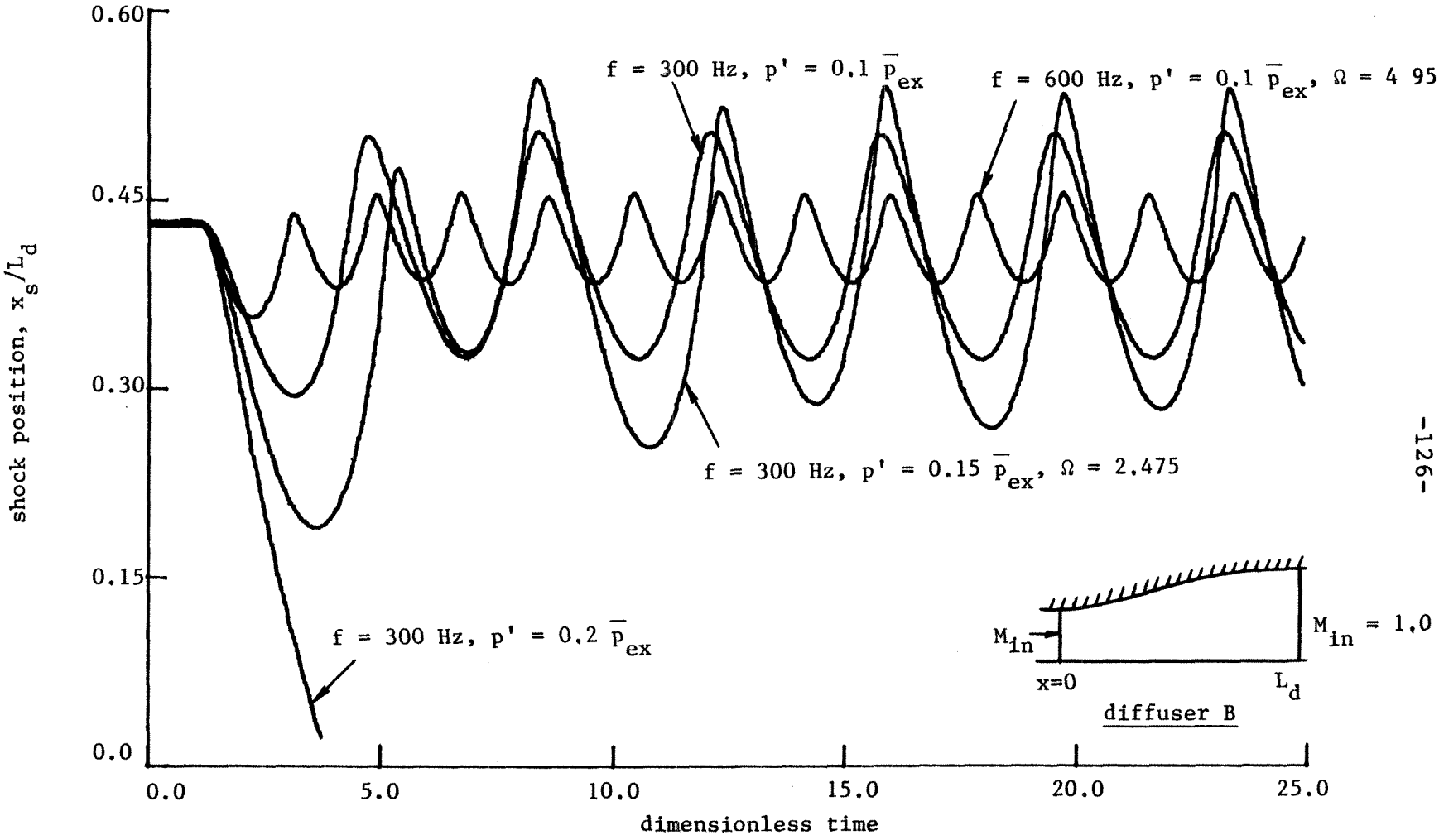

FIGURE 5.8. Instantaneous Shock Position (Diffuser B)

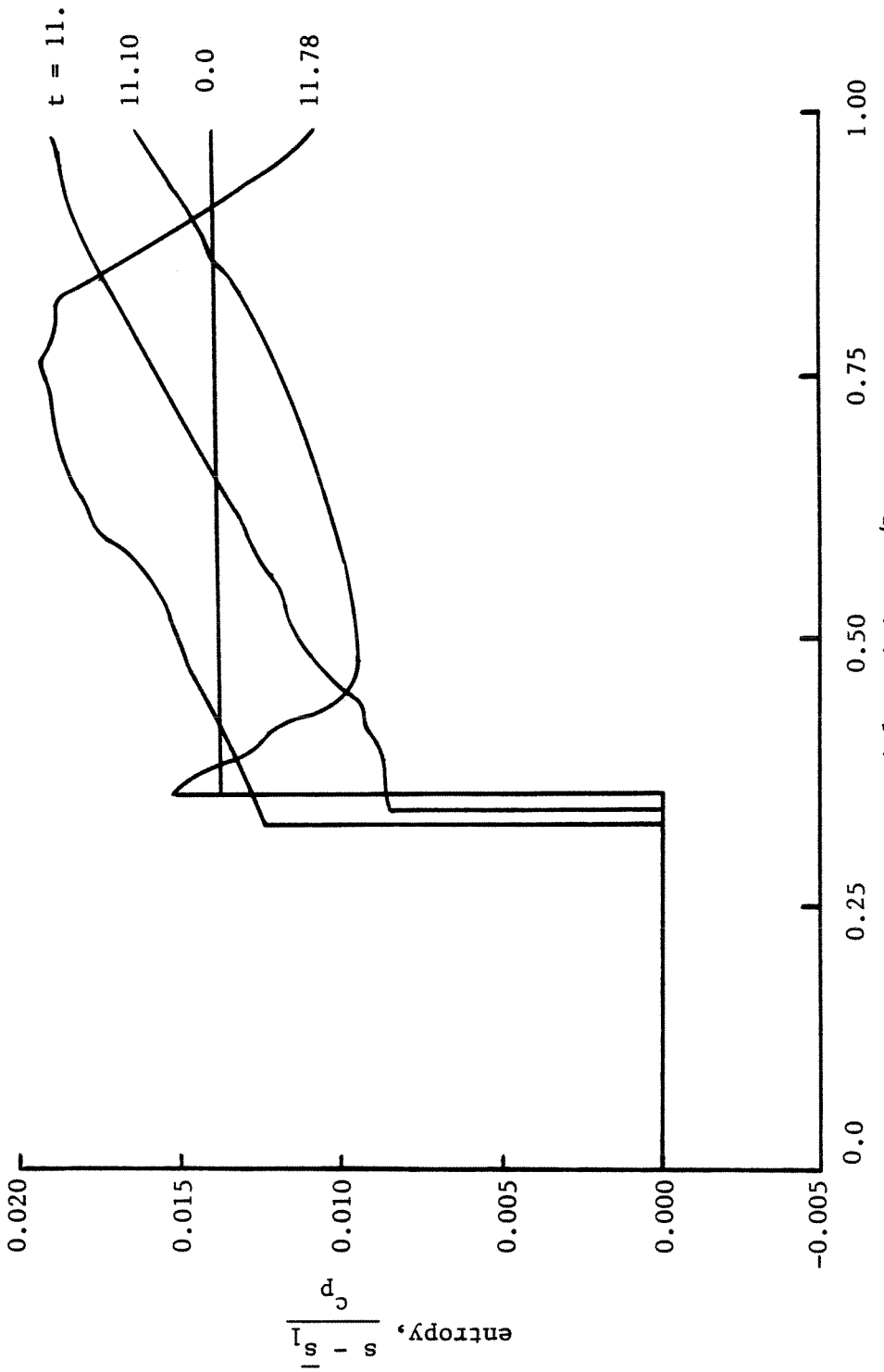

FIGURE 5.9. Entropy Distributions at Various Times within One Cycle of Oscillation (Diffuser A)

accuracy, the fluctuation of mass flow rate can be written,

$$\Delta\dot{m} = \dot{m}_1 - \dot{m}_2 = (\bar{\rho}_1 - \bar{\rho}_2)v_s' A_s \tag{5.2.6}$$

Combination of the above equation with the expression for the incident pressure fluctuation p_e', which is given in reference 11, and rearrangement of the result produce a formula for the mass response function.

$$R_m \equiv \frac{\Delta\dot{m}/\bar{m}}{p_e'/\bar{p}_2} = \frac{(\frac{\bar{\rho}_2}{\bar{\rho}_1} - 1)(\frac{\bar{a}_2}{\bar{a}_1})\frac{i\Omega}{\bar{M}_1}}{\frac{4\gamma\bar{M}_1}{\gamma+1}(\frac{\bar{p}_1}{\bar{p}_2})(\frac{\bar{a}_2}{\bar{a}_1})i\Omega + P_s} \tag{5.2.7}$$

where P_s is a function of $\bar{M}_1$, defined in reference 11. This agrees identically with the result obtained by Waugh using an alternative approach due to Hurrell.[25] Oscillations of the mass flow rate for small amplitude disturbances are easily calculated with this formula.

Oscillations of mass flow rate in diffuser A have also been computed, giving the results shown in Figure 5.10. A pressure disturbance with frequency 300 Hz and amplitude ten percent of the average pressure changes the air flow rate, and consequently the equivalence ratio of the air/fuel mixture, by almost three percent if the fuel flow rate remains constant. This will obviously affect the downstream combustion processes. Unlike the predictions of linear theory, the amplitude of mass flow oscillation is smaller for disturbances with higher amplitude. This is due to the fact that nonlinear effects tend on the average to displace the shock toward the throat and reduce its strength.

5.2.3 Upstream Disturbances

Pressure oscillations originating upstream of the shock due to unsteady boundary layers or changes in flight conditions may be important. Their influences on shock motion and the downstream flowfield are discussed in this section. A linear

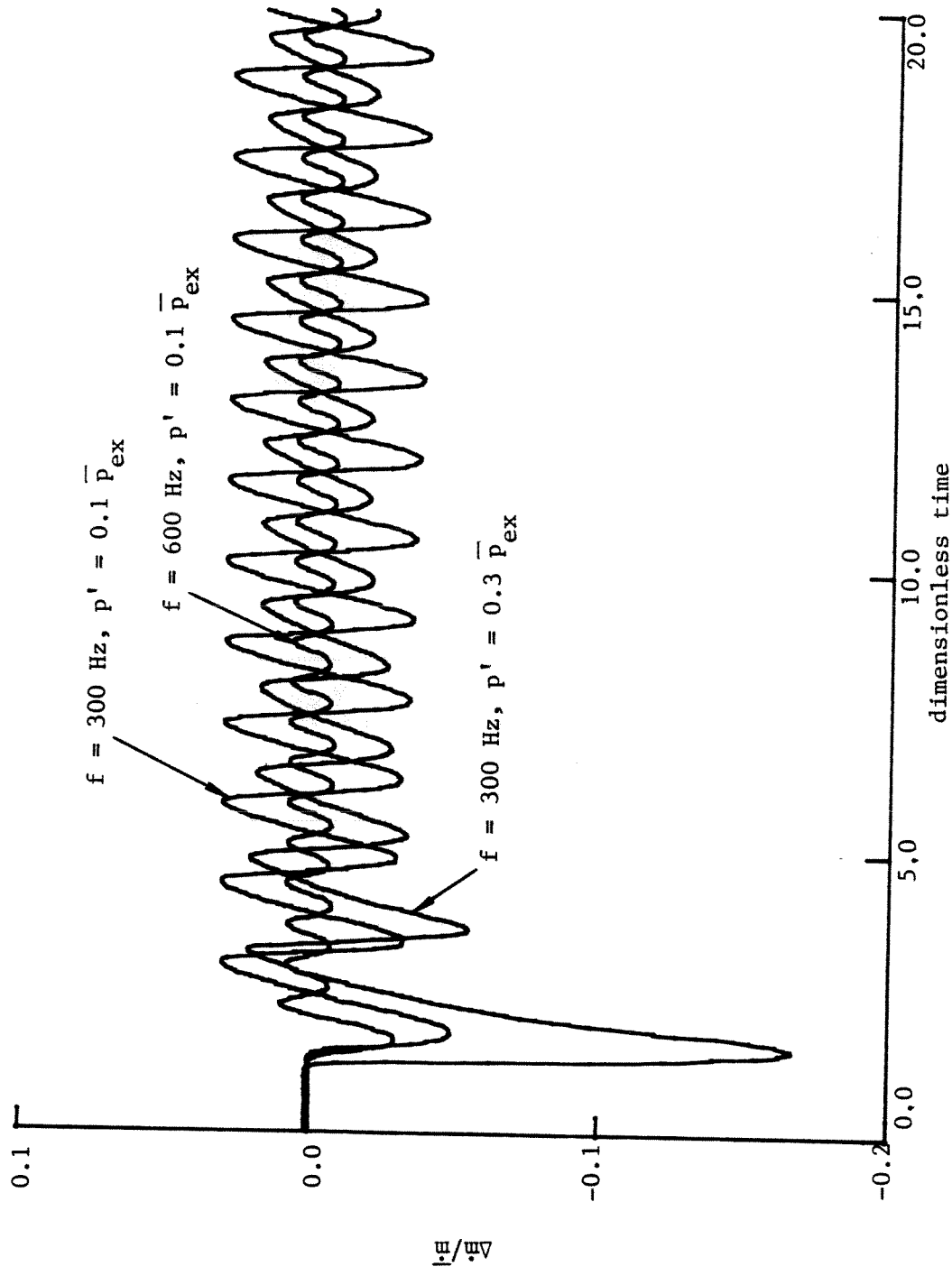

FIGURE 5.10. Oscillation of Mass Flow Rate behind a Shock (Diffuser A)

analysis is first carried out, followed by a numerical nonlinear analysis.

In contrast to the problem dealt with in the earlier work,[11] the shock motion studied here is resulted from upstream disturbances. Thus, the fluctuations of velocity in a frame moving with the shock and pressure just upstream of the shock are

$$u_1' = u_e' - v_s' + \frac{d\bar{u}_1}{dx} x_s', \tag{5.2.8}$$

$$p_1' = p_e' + \frac{d\bar{p}_1}{dx} x_s' \tag{5.2.9}$$

respectively, where the last terms on the right hand sides are due to shock motion in a nonuniform flowfield, and the subscript e denotes the incident disturbance. Similarly, the fluctuating velocity and pressure immediately downstream of the shock are

$$u_2' = u_t' - v_s' + \frac{d\bar{u}_2}{dx} x_s', \tag{5.2.10}$$

$$p_2' = p_t' + \frac{d\bar{p}_2}{dx} x_s' \tag{5.2.11}$$

Substituting the above expressions (5.2.8-11) into the normal shock relations and assuming quasi steady behavior for the shock, we obtain a formula for the transmission coefficient of a shock, T_r.

$$T_r \equiv \frac{p_t'}{p_e'} = \left[\frac{\sigma_1 + i\Omega\sigma_2}{\sigma_3 + i\Omega\sigma_4}\right] \frac{\bar{M}_1}{\bar{M}_2} \tag{5.2.12}$$

where

$$\sigma_1 = \frac{2+(1-\gamma)\bar{M}_1^2}{(\gamma+1)\bar{M}_1^2} P_s + \gamma\bar{M}_2 \left(\frac{\bar{a}_2}{\bar{a}_1}\right)\left[1 + \frac{4\bar{M}_1}{\gamma+1}\left(\frac{\bar{p}_1}{\bar{p}_2}\right)\right] U_s \tag{5.2.13}$$

$$\sigma_2 = -\frac{2\gamma}{\gamma+1}\left(\frac{\bar{a}_2}{\bar{a}_1}\right)\left[2\bar{M}_1\left(\frac{\bar{p}_1}{\bar{p}_2}\right)+\frac{\bar{M}_1^2+1}{\bar{M}_1^2}\right] \tag{5.2.14}$$

$$\sigma_3 = \gamma\bar{M}_2 U_s - P_s \tag{5.2.15}$$

$$\sigma_4 = \frac{-2\gamma}{\gamma+1}\left[1+\frac{1}{\bar{M}_1^2}+2\bar{M}_2\right] \tag{5.2.16}$$

Figure 5.11 shows the magnitude and phase of the transmission coefficient T_r. The result is well known: the shock amplifies all the disturbances from upstream. The magnitude of T_r is always greater than unity, and increases with the shock strength.

Numerical calculations for finite disturbances have shown that the dependence of the shock motion on amplitude and frequency are similar to those for downstream disturbances. The average position of shock wave is always shifted upstream.

5.2.4 Resonance

One of the important issues regarding the oscillatory pressure field in an acoustic cavity is resonance. With supersonic flow upstream of the shock in an inlet diffuser, the cavity is defined as the region from the shock to the exit, where the counter-running wave system exists. Calculation of the natural frequencies is straightfoward using a linear one-dimensional acoustic model. If we assume that the cross-sectional area of the diffuser varies slowly, then the appropriate equation describing the acoustic pressure field is

$$P = \frac{p'}{\gamma\bar{p}} = \sqrt{\frac{\bar{a}^2-\bar{u}^2}{\bar{a}}}\left[P_+ e^{-i\omega t+i\omega\int_{L_T}^{x}\frac{dx'}{\bar{a}+\bar{u}}}+P_- e^{-i\omega t-i\omega\int_{L_T}^{x}\frac{dx'}{\bar{a}-\bar{u}}}\right] \tag{5.2.17}$$

where P_+ and P_- are complex amplitudes of the right - and the left-running waves. By applying the condition for reflection at the shock and treating the exit as an

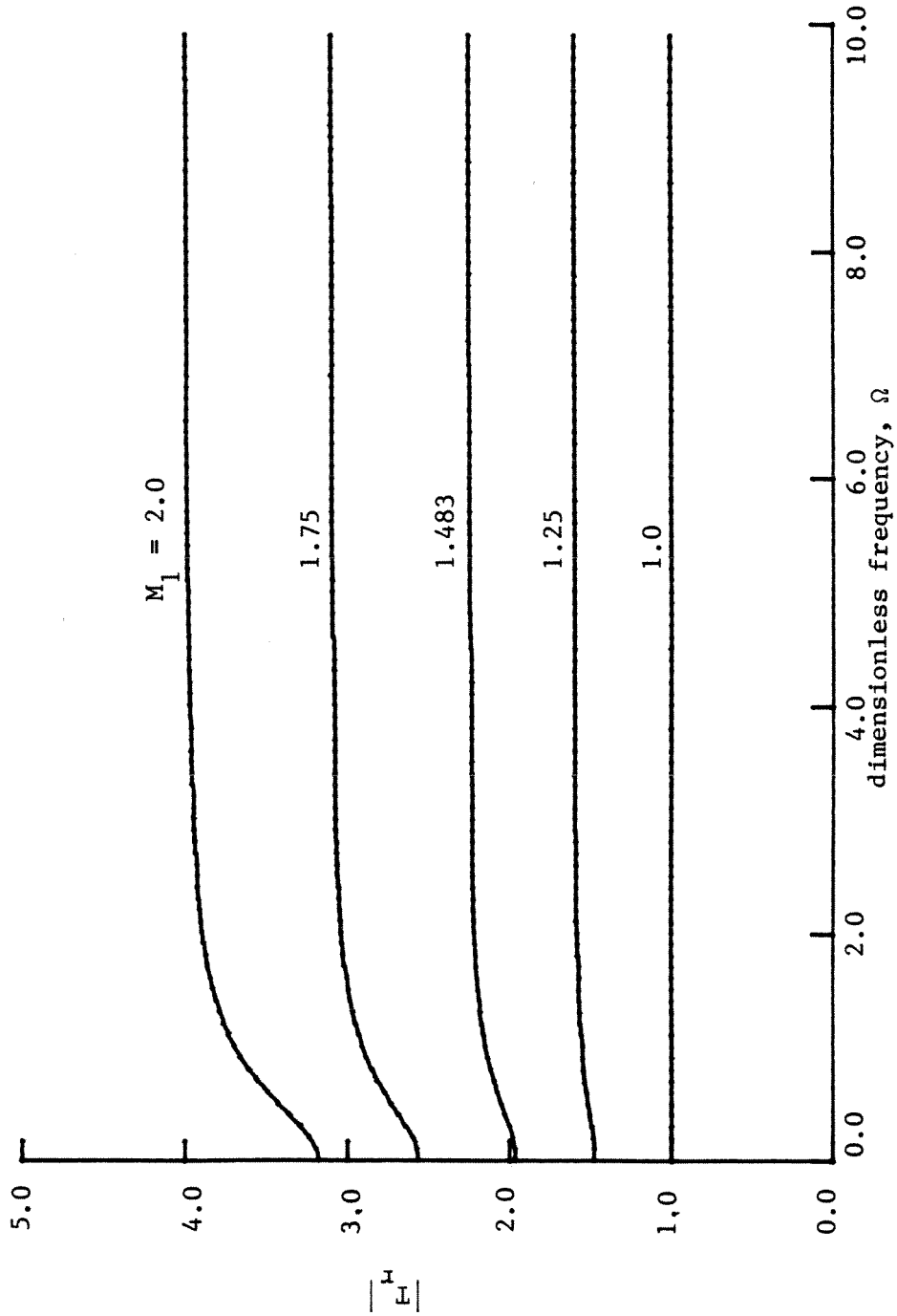

FIGURE 5.11a. Magnitude of Acoustic Transmission Coefficient, T_r

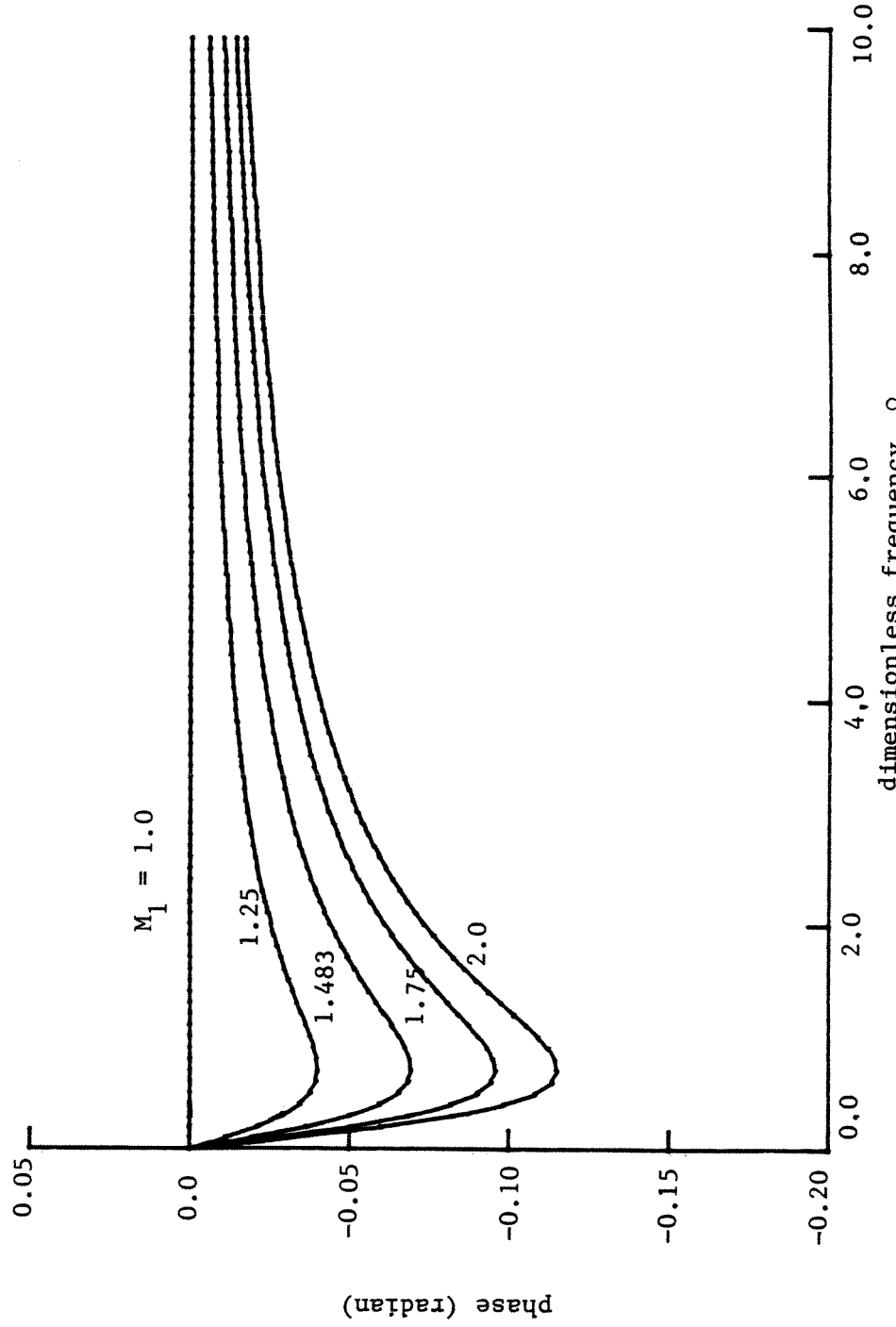

FIGURE 5.11b. Phase of Acoustic Transmission Coefficient, T_r

acoustic node, the following transcendental equation for the natural frequencies is obtained.

$$\beta e^{i\omega\int_{L_f}^{L_d}\frac{dx'}{\bar{a}+\bar{u}}} + e^{-i\omega\int_{L_f}^{L_d}\frac{dx'}{\bar{a}-\bar{u}}} = 0 \qquad (5.2.18)$$

where β is the acoustic reflection coefficient at the shock given in reference 11.

To check if resonances exist, numerical calculations have been carried out for periodic pressure oscillations with a wide range of frequencies imposed at the entrance. Figure 5.12 shows the spectra of the extreme excursions of the shock in diffuser B, where the vertical arrows indicate natural frequencies determined from (5.2.18). Only near the fourth harmonic (560 Hz) does the shock response (weakly) resemble that for resonance. The shock is an over-damped system. A similar conclusion has been reached by Sajben and Bogar[3] in their experimental investigation of forced oscillations in supercritical diffuser flows.

5.2.5 Influence of Fuel and Air Injections

So far we have only examined the behavior of a single-phase flow. For many practical ramjet engines, fuel is injected and atomized in the inlet section. It is thus necessary to examine the flowfield with liquid fuel droplets accounted for. Calculations have been done for various drop sizes, injector locations, and air flow rates through the injector, while keeping the boundary conditions and fuel-to-air ratio fixed. Figure 5.13 shows the mean pressure distributions in diffuser B with stoichiometric RJ-4 fuel droplets ($\dot{m}_{fuel} = 0.07\dot{m}_{air}$) and wall air jet introduced. The injected fuel/air flow modifies the main flowfield noticeably, moving the shock upstream and reducing the shock strength. The mean shock positions for various injection conditions are shown in Figure 5.14. The effects of fuel droplets are best measured by their momentum and heat transfer to the gas flow. Since smaller droplets mean a greater specific surface area for a mixture with fixed fuel-to-air ratio,

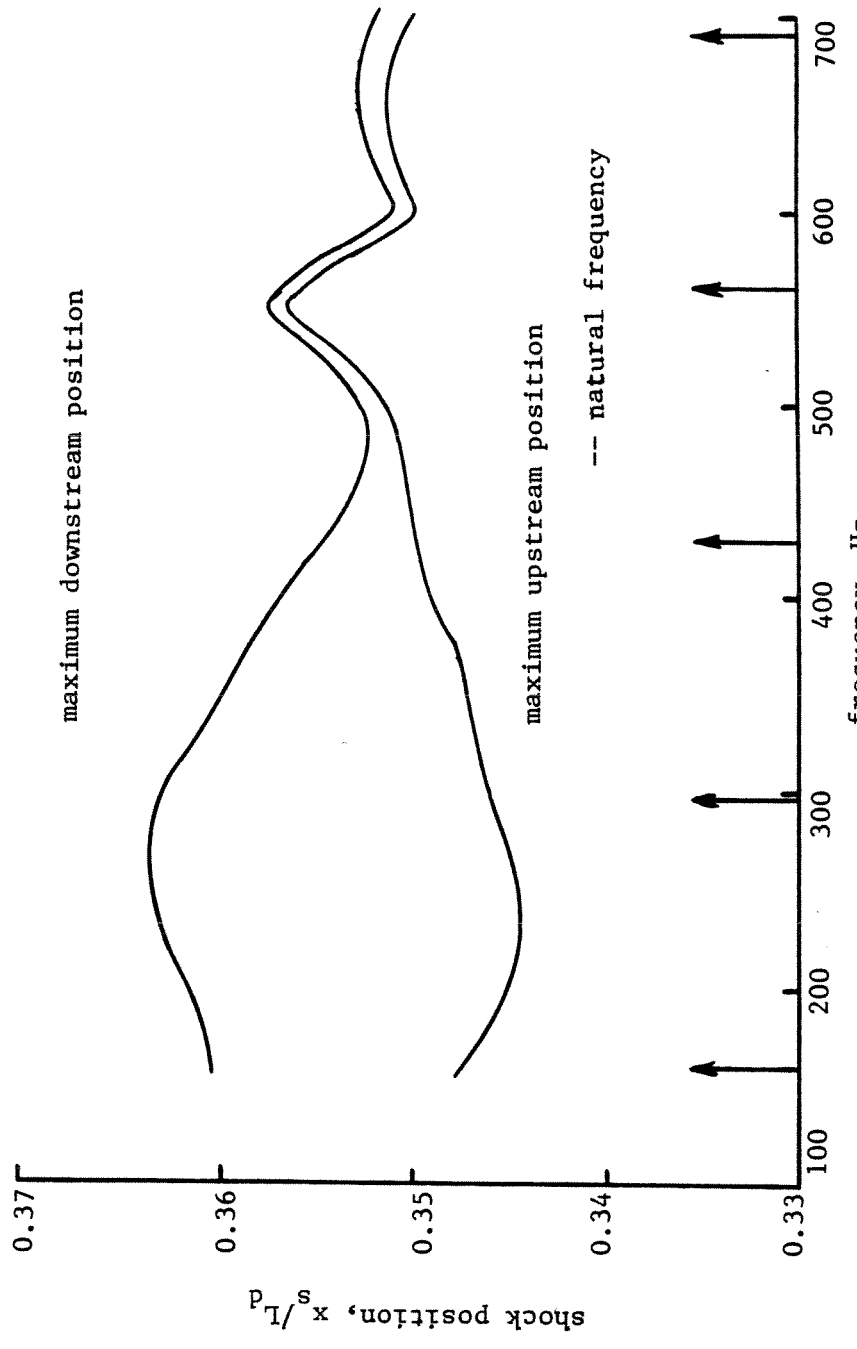

FIGURE 5.12. Maximum Upstream and Downstream Shock Positions (Diffuser A)

the effects increase with decreasing droplet size. Evidently the dependence of shock position on the rate of mass injection is the dominant effect.

Figure 5.15 shows the instantaneous shock positions subject to downstream disturbances. Comparison with Figure 5.8 clearly indicates that the stability margin of a shock is reduced by injecting fuel and air into the main flow. A pressure disturbance with $\delta p=0.1\bar{p}_{ex}$ forces the shock to pass through the throat in a flow with a small amount of air added ($\eta=0.05$), while the stability is ensured even for $\delta p=0.15\bar{p}_{ex}$ in a flow without injection.

5.2.6 Large Amplitude Oscillation

Large amplitude oscillation is of concern when the flow in front of the shock is transonic. Recent experiments on inlet diffuser flow[5] have shown that within the transonic range a small perturbation in back pressure leads to significant shock motion. The shock may be displaced upstream of the throat by the compression part of a periodic pressure wave, then either vanishes in the convergent section or accelerates to the entrance, depending on its strength. After a short while, another shock is generated at the farther downstream position according to the pressure distribution in the diffuser.

To simulate this phenomenon numerically, the entire diffuser B is considered by setting the upstream boundary at the entrance. The flowfield is first calculated under steady state conditions, giving the results shown in Figure 5.16. The scheme produces smooth and accurate transition from subsonic to supersonic flows at the throat. Subsequently, similar to the previous cases, a periodic pressure oscillation is imposed at the exit at time t=0. Figure 5.17 shows the instantaneous shock positions for disturbances having two different amplitudes. A pressure disturbance with amplitude $\delta p=0.2\bar{p}_{ex}$ displaces the shock out of the supersonic region and causes the loss of the stability margin of the system. Note that the shock speed

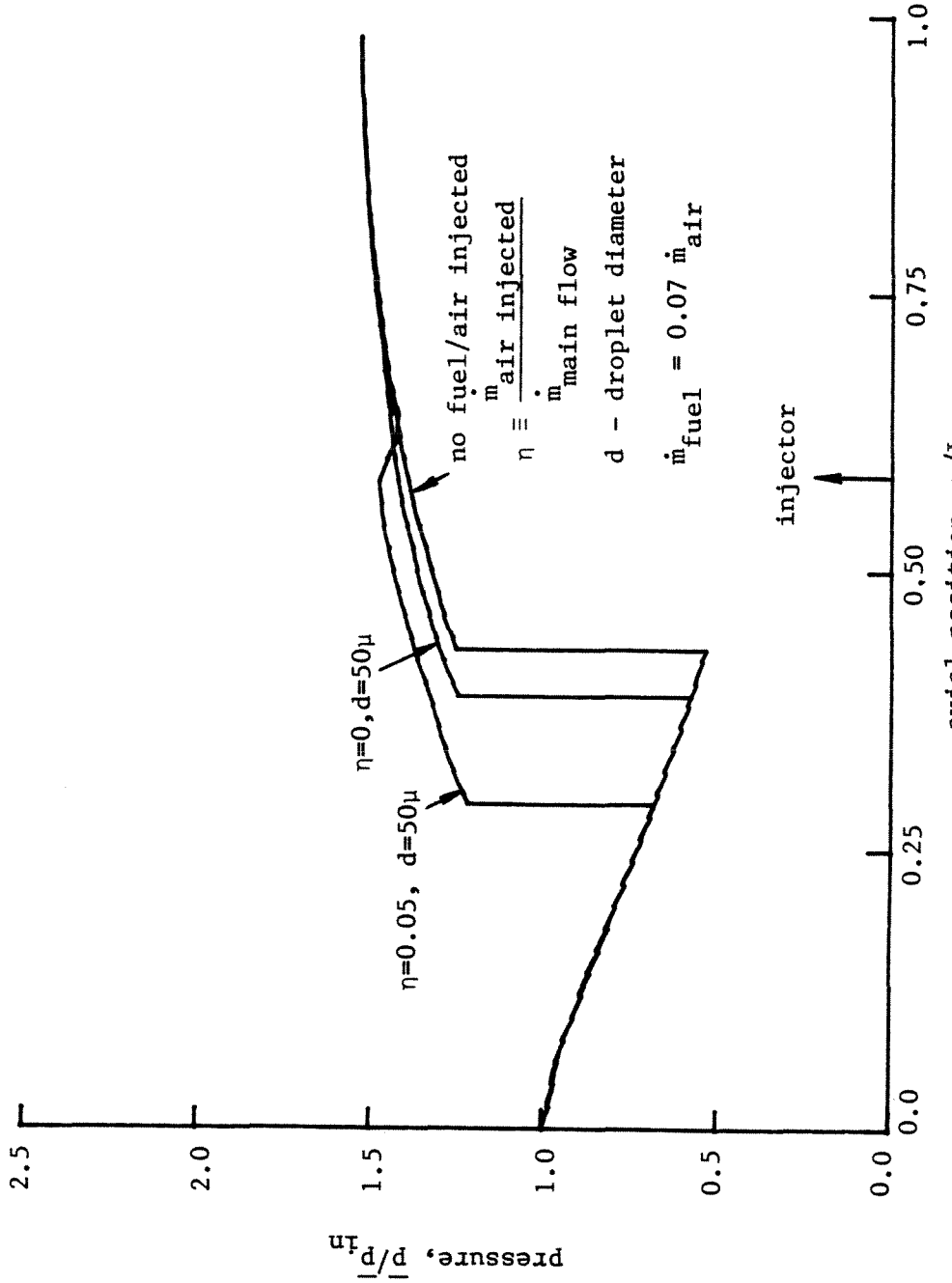

FIGURE 5.13. Mean Pressure Distributions under Various Injection Conditions (Diffuser B)

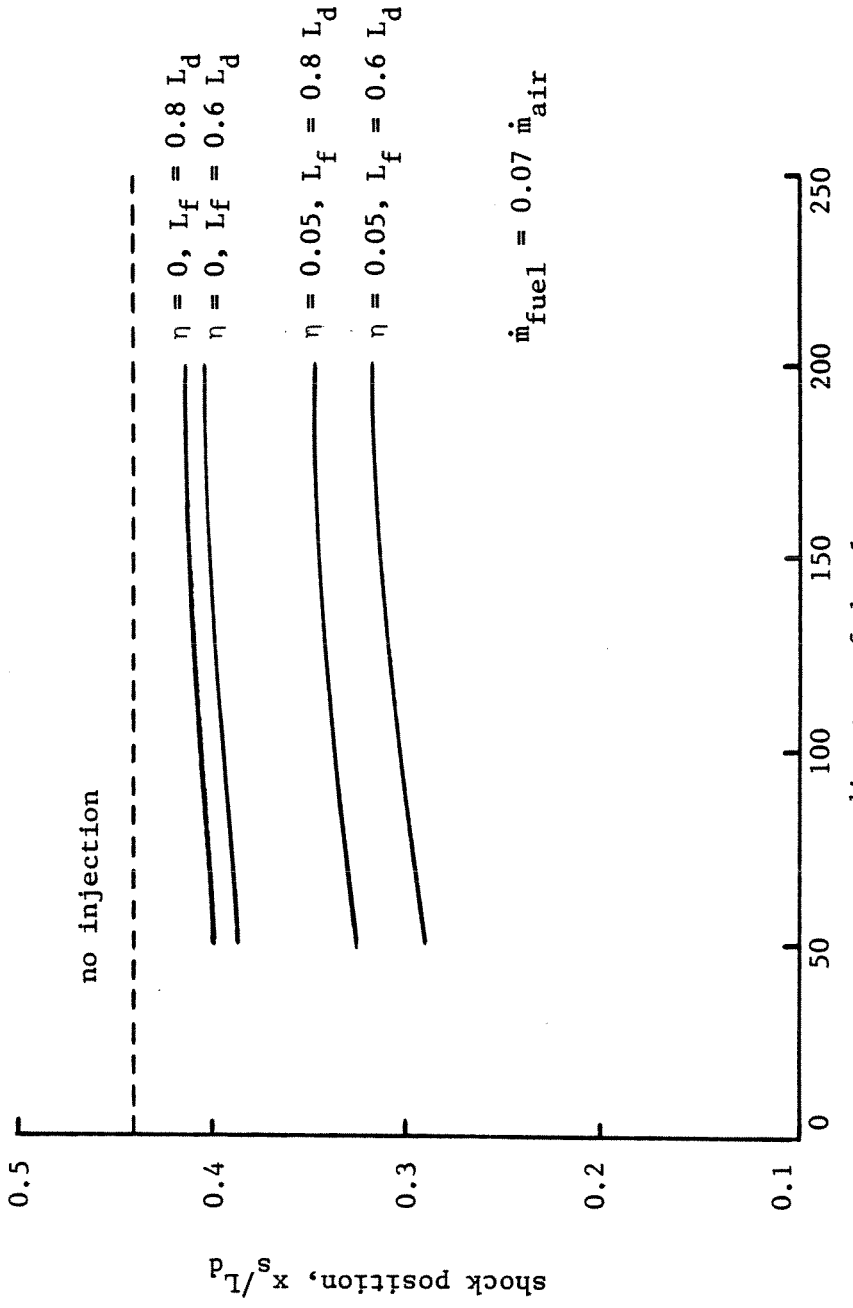

FIGURE 5.14. Dependence of Shock Position on Droplet Size and Injector Position (Diffuser B)

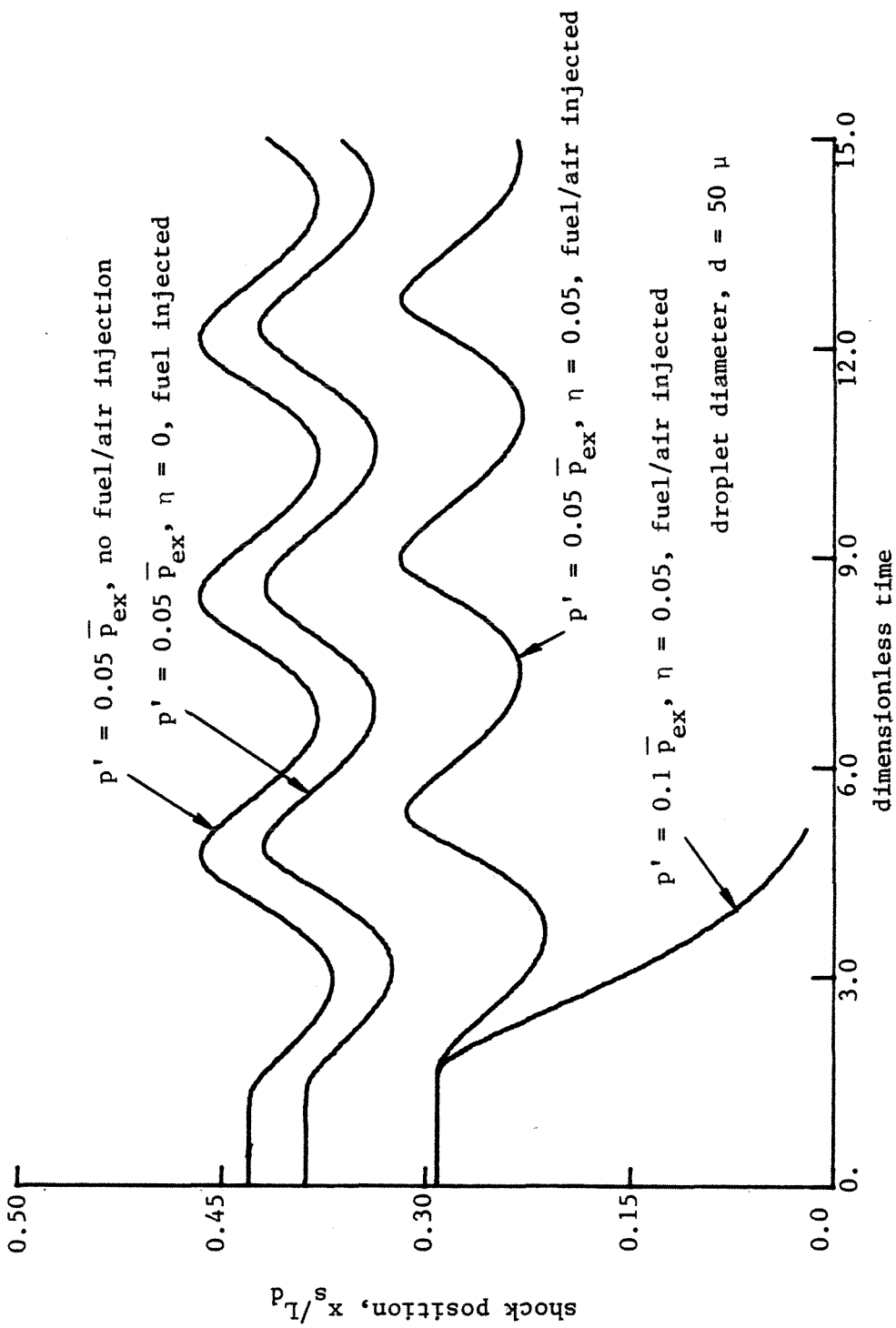

FIGURE 5.15. Instantaneous Shock Position due to Downstream Disturbance with f = 300 Hz (Diffuser B)

increases rapidly in the convergent section in which the shock is unstable within linear analysis. Figure 5.18 shows the pressure distributions at various times for large amplitude oscillation. The intermittent appearance of a shock is clearly displayed. Finally, the mass fluctuations are given in Figure 5.19.

5.2.7 Viscous Flow

Viscous effects in the boundary layers are included in order to make the model more realistic. Figure 5.20 shows the measured wall pressure distribution and the calculated mean pressure field of the core flow in diffuser B. The experimental conditions given in reference 4 are closely reproduced. The calculated Mach numbers in front of the shock are 1.24 and 1.46 respectively for the viscous and inviscid cases. The discrepency in the vicinity of the shock is due to the strong normal pressure gradient in the boundary layer in the interaction region. The viscous boundary layers have profound effects on the mean flowfields, tending to displace the shock upstream and reduce its strength. The spike immediately behind the shock, resulted from the rapid increase of boundary layer displacement thickness due to the shock wave/boundary layer interaction, represents the post-shock expansion and has been observed experimentally.[26]

5.3 Concluding Remarks

The numerical analysis described here serves as a convenient and inexpensive means of assessing the influence of large amplitude disturbances on the unsteady behavior of an inlet diffuser. It is not the intention of this work to provide a theory of the diffuser, but rather to construct an approximate representation which may later be used in analysis of the nonlinear behavior of an entire engine. Any results obtained with the formulation used here are restricted to relatively weak shocks so that flow separation does not occur.

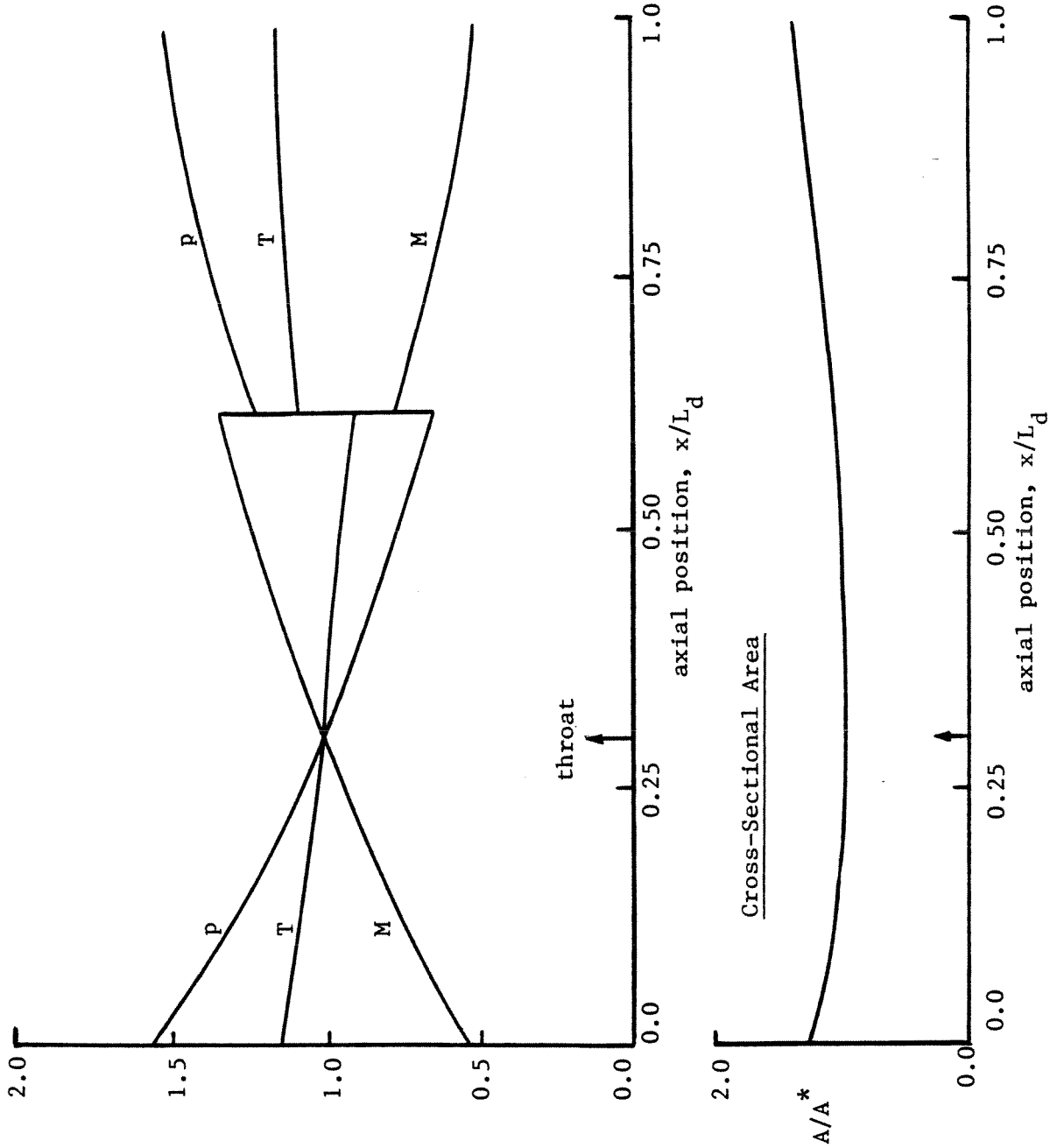

FIGURE 5.16. Distributions of Mean Flow Properties (Diffuser B)

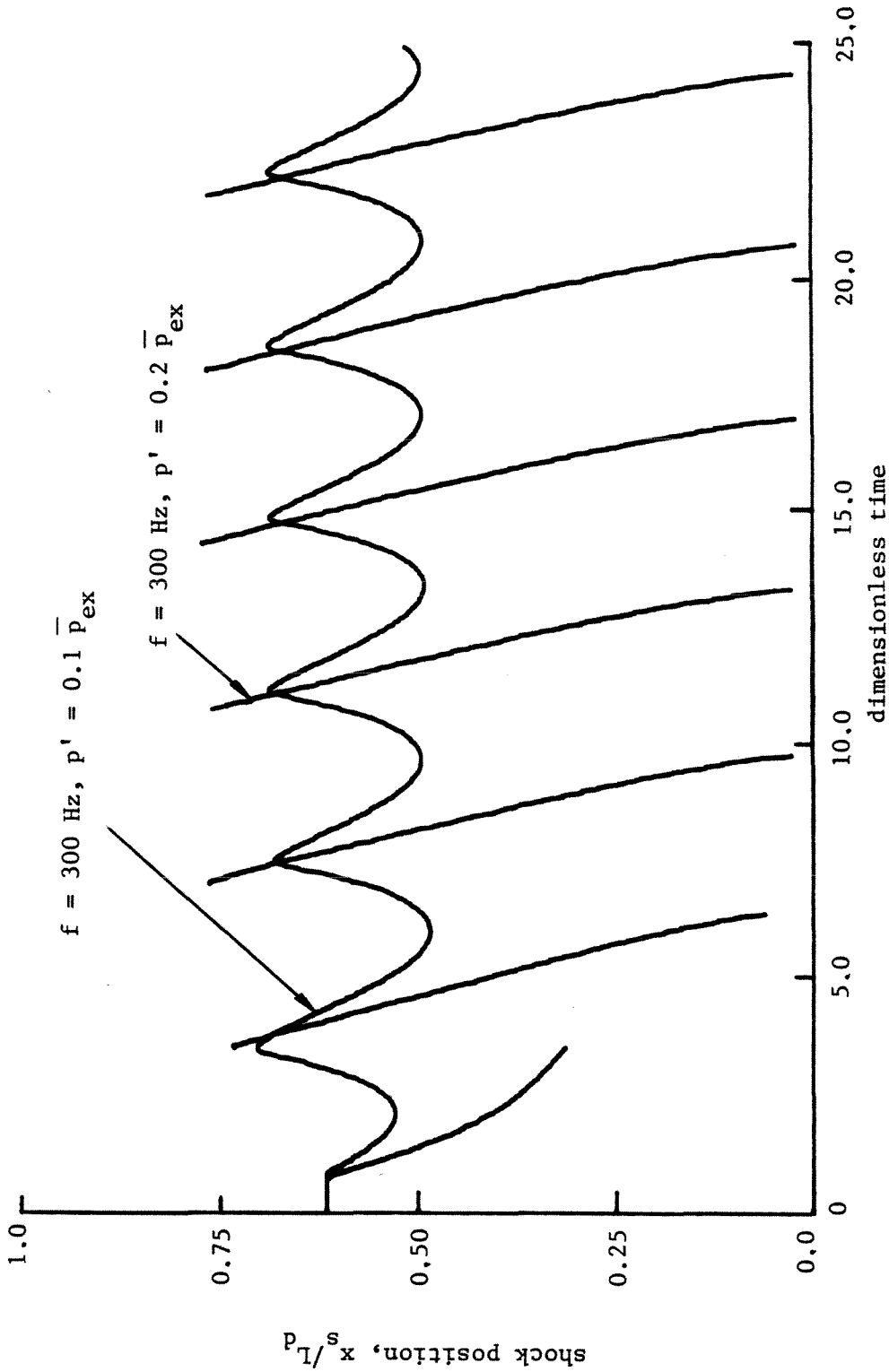

FIGURE 5.17. Instantaneous Shock Position (Diffuser B)

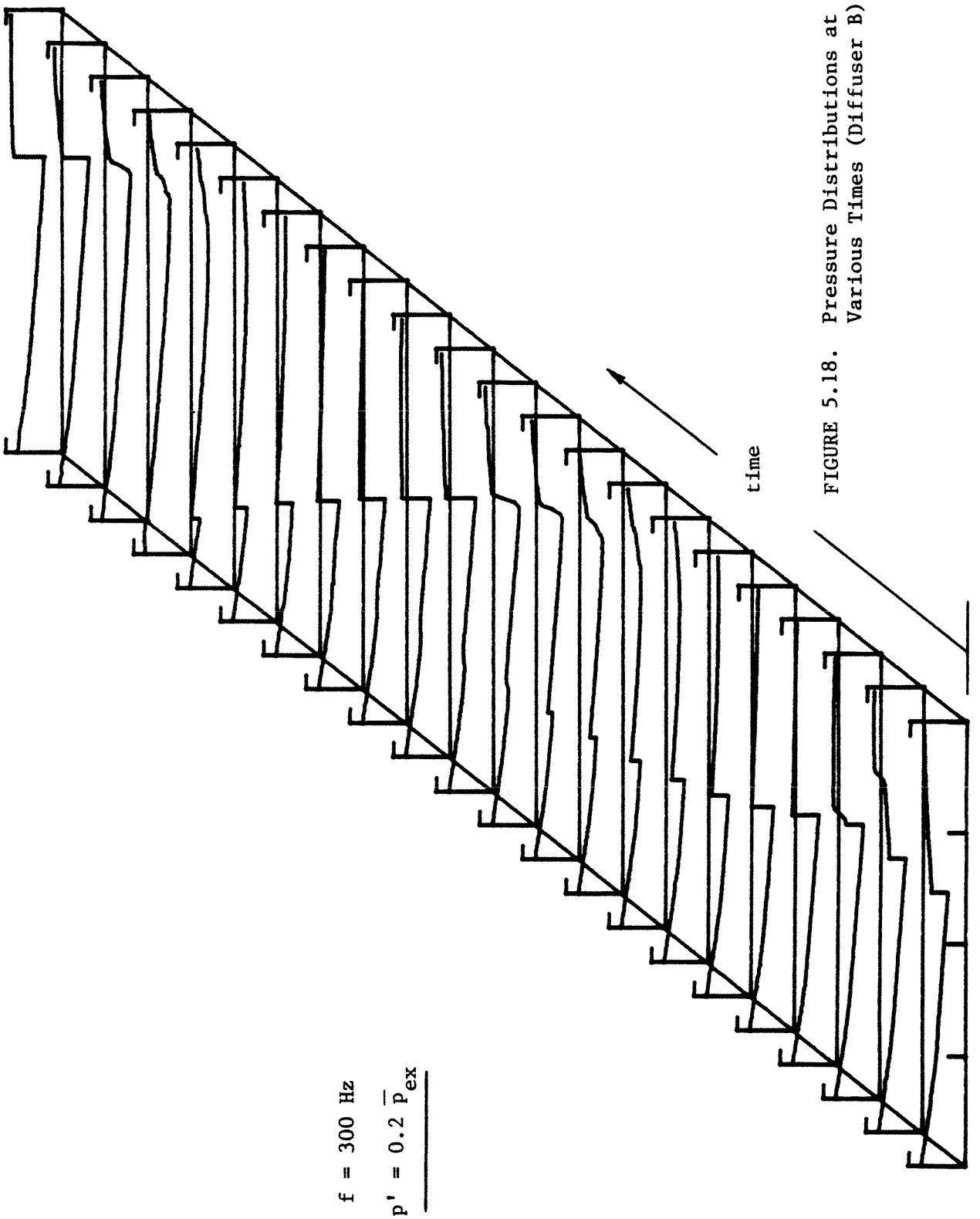

FIGURE 5.18. Pressure Distributions at Various Times (Diffuser B)

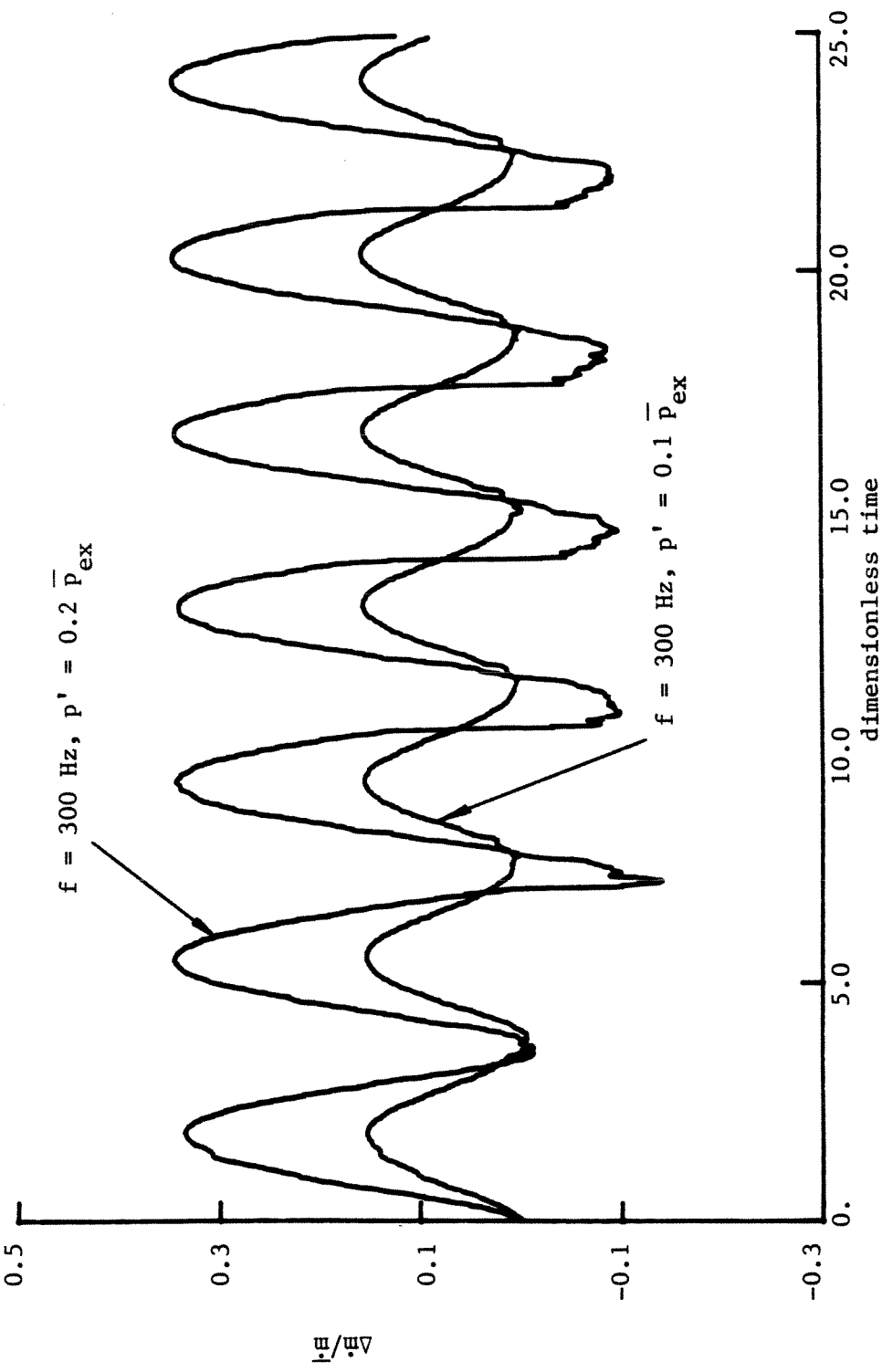

FIGURE 5.19. Oscillation of Mass Flow Rate behind a Shock (Diffuser B)

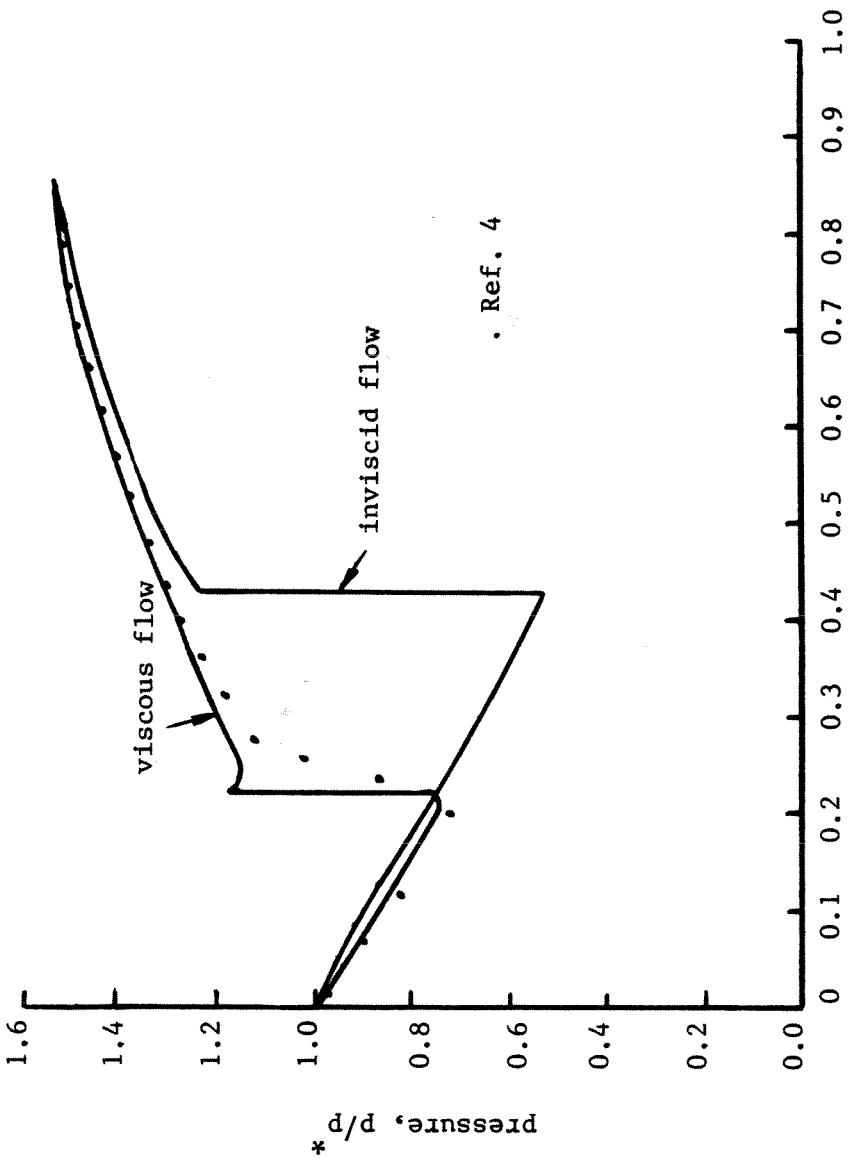

FIGURE 5.20. Measured and Calculated Mean Pressure Distributions (Diffuser B)

REFERENCES 5

1. Culick, F. E. C., 'Report of the JANNAF Workshop on Pressure Oscillations in Ramjets," *17th JANNAF Combustion Meeting*, Nov.1980.

2. Chen, C. P., Sajben, M., and Kroutil, J. C., 'Shock-Wave Oscillations in a Transonic Diffuser Flow," *AIAA Journal*, Vol. 17, Oct.1979, pp.1076-1083.

3. Sajben, M. and Bogar, T. J., 'Unsteady Transonic Flow in a Two-Dimensional Diffuser: Interpretation of Experimental Results," *McDonnell Douglas Final Report, MDC-Q-0799*, Mar.1982.

4. Bogar, T. J., Sajben, M., and Kroutil, J. C., 'Characteristic Frequencies of Transonic Diffuser Flow Oscillations," *AIAA Journal*, Vol. 21, Sep.1983, pp.1232-1240.

5. Schadow, K. C., Crump, J. E., and Blomshield, F., 'Combustion Instability in a Research Dump Combustor: Inlet Shock Oscillations," *18th JANNAF Combustion Meeting*, Oct.1981.

6. Adamson, T. C. Jr., Messiter, A. F., and Liou, M. -S., 'Large Amplitude Shock-Wave Motion in Two-Dimensional Transonic Channel Flow," *AIAA Journal*, Vol. 16, 1978, pp.1240-1247.

7. Liou, M. -S. and Sajben, M., "Analysis of Unsteady Viscous Transonic Flow with a Shock Wave in a Two-Dimensional Channel," *AIAA Paper 80-195*, 1980.

8. Liou, M. -S., 'Analysis of Viscous-Inviscid Interaction in Transonic Internal Flows," *AIAA Journal*, Vol. 21, July 1983, pp.962-969.

9. Liu, N. -S., Shamroth, S. J., and McDonald, H., 'Numerical Solutions of Navier-Stokes Equations for Compressible Turbulent Two/Three Dimensional Flows in the terminal Shock Region of an Inlet/Diffuser," *NASA-CR-3723*, 1983.

10. Liou, M. -S. and Coakley, T. J., 'Numerical Simulations of Unsteady Transonic Flow in Diffusers," *AIAA Paper No. 82-1000*, 1982.

11. Culick, F. E. C., and Rogers, T., 'The Response of Normal Shocks in Diffusers," *AIAA Journal*, Vol. 21, Oct.1983, pp.1382-1390.

12. Green, J. E., Weeks, D. J. and Brooman, J. W. F., 'Prediction of Turbulent Boundary Layers and Wakes in Compressible Flow by A Lag-Entrainment Method," *Report and Memoranda No. 3791*, January 1973.

13. Jou, W. -H. and Murman, E. M., "A Phenomenological Model for Displacement Effects of Transonic Shock Wave-Bounadry Layer Interaction," *AGARD-CP-291*, October 1980.

14. Baum, J. D. and Levine, J. N., 'Evaluation of Finite Difference Schemes for Solving Nonlinear Wave Propagation Problems in Rocket Combustion Chambers," *AIAA Paper No. 81-0420*, 1974.

15. Harten, A., 'The Artificial Compression Method for Computation of Shocks and Contact Discontinuities: III, Self Adjusting Hybrid Schemes," *AFOSR Technical*

Report TR-77-0659, 1977.

16. Richtmyer, R. D. and Morton, K. W., *Difference Methods for Initial-Value Problems*, Interscience Publishers, New York, 2nd edition, 1969.

17. Bradshaw, P., Ferriss, D. H. and Atwell, N. P., "Calculation of Turbulent Boundary Layer Development Using the Turbulent Energy Equation," *Journal of Fluid Mechanics*, Vol.28, 1967, pp.593-613.

18. Carter, J. E., "Inverse Boundary Layer Theory and Comparison with Experiment," *NASA-TP-1208*, September 1978.

19. Melnik, R. E., "Turbulent Interactions on Airfoils at Transonic Speeds - Recent Developments," *AGARD-CP-291*, October 1980.

20. Adamson, T. C. and Messiter, A. F., "Analysis of Two-Dimensional Interactions between Shock Waves and Boundary Layers," *Annual Review of Fluid Mechanism*, Vol.12, 1980,pp.103-138.

21. Yoshihara, H. and Zonars, D., "An Analysis of Pressure Distributions on Planar Supercritical Profiles with and without Jet Flaps at High Reynolds Numbers," *AGARD-CP-291*, October 1980.

22. Nandanan, M., Stanewsky, E. and Inger, G. R., "A Computational Procedure for Transonic Airfoil Flow Including a Special Solution for Shock-boundary Layer Interaction," *AIAA Paper 80-1389*, July 1980.

23. Green, G. E., "Interactions between Shock Waves and Turbulent Boundary Layers," *Progress in Aeronautical Sciences*, Vol.11, 1970, pp.235-348.

24. De'lery, J., "Recherches sur L'interaction onde de Choc-Couche Limite Turbulente," *ONERA-TP-1976-135*, 1976.

25. Waugh, R. C., "Inlet Response to Acoustic Oscillations," Appendix C, *Ramjet Combustor Instability Investigation: Literature Survey and Preliminary Design Study*, prepared by R. C. Waugh et al, United Technologies Report CSD-2770-IR-1, Jan.1982.

26. Oswatitsch, K. and Zierep, J., "Das Problem des senkrechten StoBes an einer gekrummten Wand," *ZAMM*, Vol.40, 1960, pp.143-144.

NOMENCLATURE 5

a	speed of sound
A	geometric cross-sectional area of diffuser
A_c	effective cross-sectional area of diffuser
c_l	specific heat of fuel
c_p	constant pressure specific heat of air

d	diameter of fuel droplet
f	frequency
F_p	drag force between air and fuel droplets
L_d	length of diffuser
L_f	position coordinate of fuel injector
M	Mach number
p	pressure
P_s	defined by Eq. (29), Ref. 11
P_+, P_-	amplitudes of rightward and leftward traveling pressure waves, respectively
Q_p	heat transfer rate between air and fuel droplets
R_m	mass response function, defined by Eq. (5.2.7)
s	entropy
t	time
T	temperature
T_r	acoustic transmission coefficient, defined by Eq. (5.2.12)
u	velocity
U_s	defined by Eq. (30), Ref. 11
v_s	velocity fluctuation of normal shock
x	position coordinate along the axis of the diffuser
x_s	position fluctuation of normal shock
β	acoustic reflection coefficient of normal shock presented to downstream disturbance
γ	ratio of specific heats
η	ratio of air flow through the injector to the main flow
ρ	density
ω	angular frequency
ω_g	rate of air injected into the main flow
ω_p	rate of liquid fuel injected into the main flow
Ω	dimensionless angular frequency, defined by Eq. (5.2.4)

superscripts

$*$	sonic condition
$(\bar{\ })$	average value
$(\ )'$	fluctuation

subscripts

e	incident disturbance
ex	value at exit of diffuser
in	value at entrance of diffuser
p	liquid phase
s	value at normal shock
sg	value at port of fuel injector
t	transmitted disturbance
1	value upstream of normal shock
2	value downstream of normal shock

Chapter 6

PRESSURE OSCILLATIONS IN SIDE-DUMP RAMJET ENGINES

This chapter deals with the combustion induced pressure oscillations in two research side-dump ramjet engines, being motivated by recent experimental work conducted at the Naval Weapons Center.[1,2] Figure 6.1, taken from reference 2, shows the baseline configuration considered. Preheated air is delivered from the plenum chamber to the combustor through two circular side ducts. Fuel injection takes place just behind the diffuser section to ensure adequate mixing of air and droplets, using a fixed orifice, contra-stream injection system. Because the engine exhibits severe transverse oscillations under many test conditions, a tangential mode suppression vane is used. This has proved to be an effective method, suppressing high frequency fluctuations significantly. Details of the system are given in reference 1.

In the following sections, a one-dimensional model is employed to formulate the problem, which is then solved numerically. The engine is treated in two parts: the inlet section, including a region of two-phase flow downstream of the plane of fuel injection, and the dump combustor. Combustion processes are crudely modeled as a stirred reactor, occupying the forward portion of the combustor, followed by a length of plug flow. Calculations are first carried out for the steady flowfields. The unsteady behavior of the engine is then determined by its response to a small disturbance imposed on the mean flow. In addition to the spacial distributions of flow variables at various times, the power and cross spectral densities are computed for the time history of the pressure.

6.1 Formulation

Because the flow properties change abruptly across the dump plane, the engine

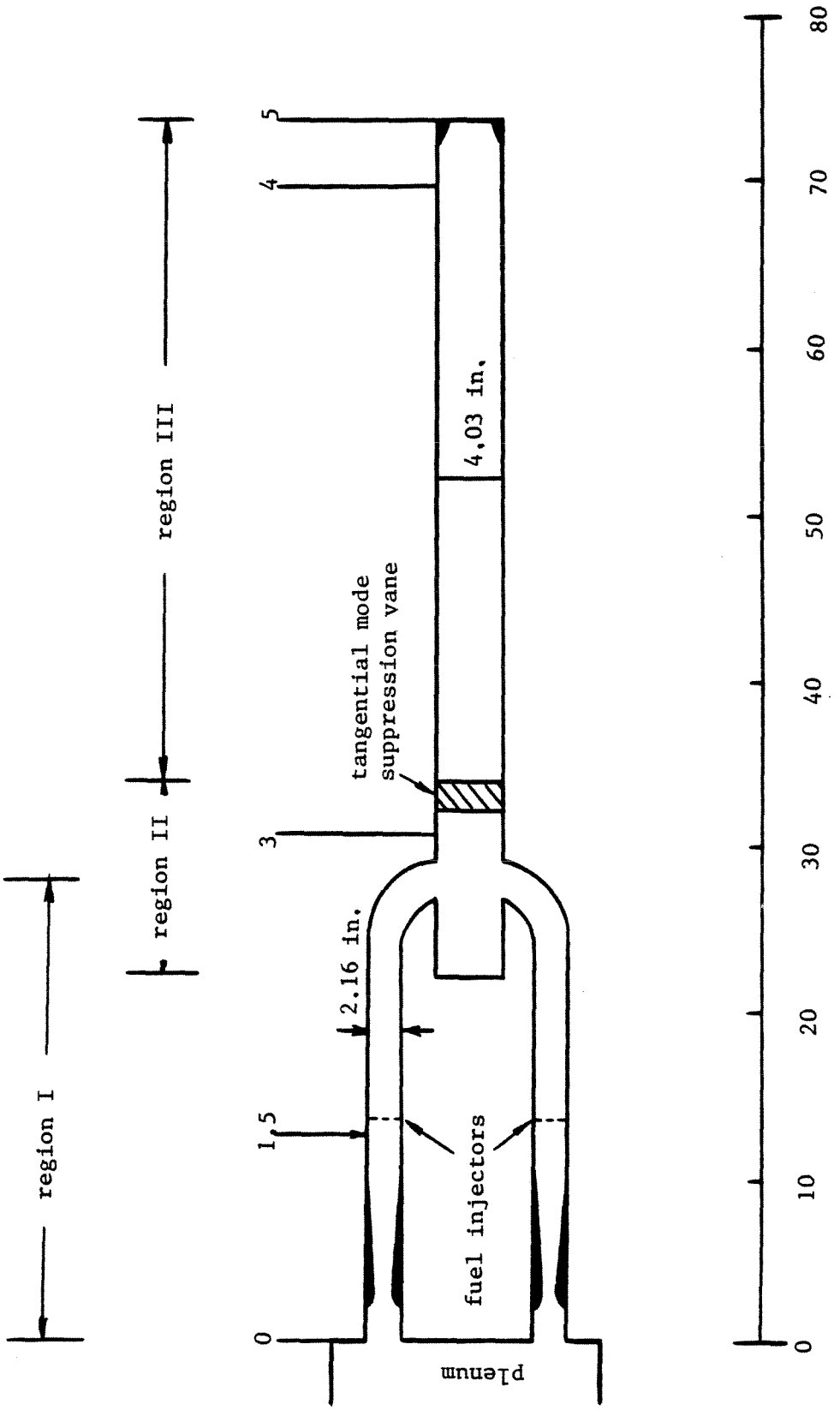

FIGURE 6.1. Baseline Configuration

is first approximated by division into two parts: the inlet section (region I) and the dump combustor. Each region is treated separately and matched with the other. The physical phenomena downstream of the inlet ports, roughly ranging from the dome of the combustor to the transverse mode suppression vane, are extremely complicated. The important processes include mixing of unburned and burned gases, droplet vaporization, and finite-rate chemical reaction. To bypass these complexities, a lumped parameter analysis is used to formulate the combustion processes in this region. The combustor therefore consists of a stirred reaction section (region II) for ignition and preliminary combustion, and a plug flow reactor section (region III) for final burn-out.

The model is based on the one-dimensional approximation for two phase flow, as described in Chapters 4 and 5. The inviscid conservation equations for the gas flow are

gas-phase

$$\frac{\partial \rho}{\partial t} + \frac{1}{A}\frac{\partial(\rho u A)}{\partial x} = 3\rho_p r_b \tag{6.1.1}$$

$$\frac{\partial(\rho u)}{\partial t} + \frac{1}{A}\frac{\partial}{\partial x}\left[\left(\frac{p}{\gamma_{in}} + \rho u^2\right)A\right] = \frac{p}{\gamma_{in}A}\frac{dA}{dx} + F_p + 3\rho_p r_b u_p \tag{6.1.2}$$

$$\frac{\partial}{\partial t}\left[\rho\left(\frac{\chi T}{\gamma_{in}(\gamma-1)} + \frac{u^2}{2}\right)\right] + \frac{1}{A}\frac{\partial}{\partial x}\left[\rho u A\left(\frac{\chi T}{\gamma_{in}(\gamma-1)} + \frac{u^2}{2}\right)\right]$$

$$= \frac{-1}{\gamma_{in}A}\frac{\partial(upA)}{\partial x} + \frac{Q_p}{\gamma-1} + u_p F_p + 3\rho_p r_b\left(h_v + \frac{u_p^2}{2}\right) + \dot{m}_{k,f}\Delta H \tag{6.1.3}$$

species equation

fuel
$$\frac{\partial(\rho Y_f)}{\partial t} + \frac{1}{A}\frac{\partial(\rho Y_f u A)}{\partial x} = -\dot{m}_{k,f} + 3\rho_p r_b \tag{6.1.4a}$$

oxygen $$\frac{\partial(\rho Y_o)}{\partial t} + \frac{1}{A}\frac{\partial(\rho Y_o u A)}{\partial x} = -\dot{m}_{k,o} \tag{6.1.4b}$$

For convenience of numerical calculation, the governing equations for the liquid flow are solved in the following non-conservation form.

liquid-phase

$$\frac{\partial \rho_p}{\partial t} + \frac{\partial(\rho_p u_p)}{\partial x} = \omega_p - \frac{\rho_p u_p}{A}\frac{dA}{dx} - 3\rho_p r_b \tag{6.1.5}$$

$$\frac{\partial u_p}{\partial t} + u_p\frac{\partial u_p}{\partial x} = -\frac{F_p}{\rho_p} \tag{6.1.6}$$

$$\frac{\partial T_p}{\partial t} + u_p\frac{\partial T_p}{\partial x} = -\frac{Q_p}{\rho_p c_l} \tag{6.1.7}$$

surface regression rate of droplet

$$\frac{Dr_p}{Dt} \equiv \frac{\partial r_p}{\partial t} + u_p\frac{\partial r_p}{\partial x} = r_b \tag{6.1.8}$$

The flow properties are normalized with respect to their quantities at the end of the inlet diffuser except the velocity, which is referenced to the speed of sound. A nomenclature is given in the end of this chapter.

In this study, the fuel/air mixture is lean and well mixed before vaporization occurs. Each droplet acts individually without interaction with the others. The droplet regression rate r_b is therefore obtained by considering the vaporization or combustion of a single droplet in a convective environment. For quasi-steady behavior and uniform temperature in the droplet, the surface regression rate r_b is found to be[3]

$$r_b = \frac{\rho D}{\rho_l r_p^2}\ln(1 + B)\cdot[1 + 0.39P_r^{1/3}R_{el}^{1/2}] \tag{6.1.9}$$

The second term in the square brackets is used as an empirical correction for convective heat and mass transfer. The transfer number B represents the *driving*

force for the diffusion process and is defined as follows.[4]

$$\text{pure vaporization} \qquad B \equiv \frac{c_p(T - T_{bp})}{L} \tag{6.1.10a}$$

$$\text{droplet combustion} \qquad B \equiv \frac{c_p(T - T_{bp}) + \varphi_{fo} Y_o \Delta H}{L} \tag{6.1.10b}$$

where φ_{fo} is the stoichiometric ratio of fuel to oxygen. The regression rates of liquid droplets are not strongly influenced by the surrounding pressure and temperature because of the insensitivity of the product ρD to them and the appearance of B in the logarithmic function.

6.1.1 Combustion Process

The chemical reaction rate $\dot{m}_{k,f}$ is an essential element in the entire analysis. Its formulation depends heavily on the conditions of the droplets flowing into the combustor. A simple estimate of the droplet size in the inlet section has been made by comparing various time scales associated with the droplet heating-up, the vaporization rate, and the flow residence. For the problem studied here, the port diameter of fuel injector is 1.016 mm and the initial droplet size is about 30 microns according to the formula given by (4.1.13). Most of the vaporization takes place within the inlet, producing very tiny droplets with diameter of the order of 10 microns at the dump plane. As a result, the combustion processes are assumed to be homogeneous,[5] similar to those of a premixed combustible gas. A further check of this assumption will be given later.

As mentioned earlier, the flowfield in the upstream part of the combustor is treated as a stirred reactor in which chemical reaction takes place uniformly. While the method provides reasonable solutions for the energy release, direct application to unsteady problems is inappropriate. The reactor usually occupies such a space that prohibits certain spacial variations of oscillatory flowfields. Conse-

quently, the frequencies may be overestimated except for very low frequency oscillations.

To get around this problem, a patching technique has been used with the consideration of an equivalent combustor as shown in Figure 6.2. The flowfield is assumed to be quasi one-dimensional everywhere in the combustion chamber. However, the rate of heat generation due to combustion in the stirred reactor section is calculated in an average sense, using a lumped parameter analysis described below.

Conservation laws are applied to obtain three conservation equations together with two species equations. Legitimately, these equations can be derived by integrating (6.1.1-4) with respect to x over the reactor section and ignoring the momentum and heat transfer between two phases.

$$V\frac{d\rho}{dt} = \dot{m}_1 - \dot{m}_3 \tag{6.1.11}$$

$$V\frac{d\rho u}{dt} = \dot{m}_1 u_1 - \dot{m}_3 u_3 + A_2(p_1 - p_3) \tag{6.1.12}$$

$$V\frac{d\rho E}{dt} = \dot{m}_1 h_{t1} - \dot{m}_3 h_{t3} + \dot{\omega}_f \Delta H \tag{6.1.13}$$

$$V\frac{d\rho Y_f}{dt} = \dot{m}_1 Y_{f1} - \dot{m}_3 Y_{f3} - \dot{\omega}_f \tag{6.1.14}$$

$$V\frac{d\rho Y_o}{dt} = \dot{m}_1 Y_{o1} - \dot{m}_3 Y_{o3} - \nu\dot{\omega}_f \tag{6.1.15}$$

The subscripts 1 and 3 denote respectively the inlet and the exit planes of the reactor, and Y_{f1} is the bulk mass fraction of the fuel at the entrance, including both fuel vapor and droplet. The lumped flow properties on the left-hand sides of (6.1.11-15) take the values of those quantities at the exit plane, being consistent with the concept of the stirred reactor.

The chemical reaction rate is determined with a global chemical kinetics model

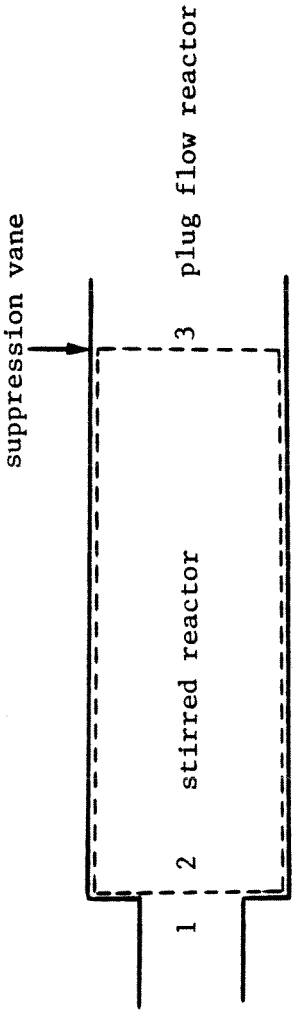

FIGURE 6.2. Schematic Diagram of An Equivalent Combustor

proposed by Edelman and Fortune,[6] which contains as a rate-controlling step the following subglobal oxidation procedure.

$$C_nH_m + \frac{n}{2}O_2 \rightarrow \frac{m}{2}H_2 + nCO \tag{6.1.16}$$

This reaction is unidirectional with an empirically determined rate given by

$$\frac{d[C_nH_m]}{dt} = AT^b p^{0.3}[C_nH_m]^{0.5}[O_2]e^{-E/RT} \tag{6.1.17}$$

where [ ] denotes molar concentration. Therefore, the rate of the total amount of fuel consumed in the reactor can be written as

$$\dot{\omega}_f = \alpha' T p^{0.3} \rho^{1.5} Y_f^{0.5} Y_o e^{-E/RT} \equiv \alpha Y_f^{0.5} Y_o \tag{6.1.18}$$

The constant α' absorbs all the unit conversion factors and the pre-exponential coefficient in the expression for the chemical reaction rate.

Rearrangement of (6.1.11) and (6.1.14-15) leads to

$$Y_{o3} = Y_{o1} + \nu[Y_{f3} - Y_{f1}] + \tau_{SR}[\nu\frac{dY_{f3}}{dt} - \frac{dY_{o3}}{dt}] \tag{6.1.19}$$

where τ_{SR} is defined as $\rho V/\dot{m}_1$, representing the residence time of the combustible mixture in the reactor. If the characteristic time of pressure oscillation is much greater than τ_{SR}, then the time derivatives appearing in the above equations can be ignored. The whole process becomes quasi-steady. Of course, this happens only for very low frequency case.

Equation (6.1.19) is further simplified by taking into account the species concentrations at the inlet plane. For a mixture containing only fuel and air, that equation becomes

$$Y_{o3} = c_1 + c_2 Y_{f1} + c_3 Y_{f3} \tag{6.1.20}$$

where

$$c_1 = 0.231 + \tau_{SR}[\nu\frac{dY_{f3}}{dt} - \frac{dY_{o3}}{dt}]$$

$$c_2 = -3.55$$

$$c_3 = 3.317$$

Combination of (6.1.14), (6.1.18), and (6.1.20) and rearrangement of the result produce a third-order polynominal for Y_{f3}

$$d_3Y_{f3}^3 + d_2Y_{f3}^2 + d_1Y_{f3} + d_0 = 0 \qquad (6.1.21)$$

The coefficients d_i are functions of the lumped flow properties and the inlet fuel concentration, defined as follows.

$$d_3 = \beta^2 c_3^2$$

$$d_2 = 2c_1c_3\beta^2 + 2c_2c_3\beta^2Y_{f1} - 1$$

$$d_1 = \beta^2c_1^2 + \beta^2c_2^2Y_{f1}^2 + 2c_1c_2\beta^2Y_{f1} + 2Y_{f1} - 2c_4$$

$$d_0 = -Y_{f1}^2 - c_4^2 + 2Y_{f1}c_4$$

and

$$c_4 = \tau_{SR}\frac{dY_{f3}}{dt}; \qquad \beta = \frac{\alpha}{\dot{m}_1}$$

The overall calculation for the rate of fuel consumption $\dot{\omega}_f$ is based on an iteration scheme. We first assume the temperature field in the reactor and compute Y_{f3} from (6.1.21), taking the pressure field to be p_1. $\dot{\omega}_f$ is then determined from (6.1.18) and (6.1.20). As a result, the flow properties in the reactor become known after some manipulations of (6.1.11-13). The time derivatives are estimated using the fourth order Runge-Kutta method. The same procedure is repeated until the calculated temperature converges to its initial guessed value. To improve the

numerical efficiency, an under-relaxation method with relaxation coefficient 0.75 has been used for the temperature. It is important to note that in the stirred reactor theory, the solution is usually not unique due to the exponential variation of the energy release with the temperature (6.1.18). Depending on the flow conditions at the entrance of the reactor and the volume V, two or three solutions with different temperatures may be obtained. Only the result having the highest temperature, close to the adiabatic flame temperature, is physically realistic.[3,7]

With a uniform source distribution of energy, the chemical reaction rate $\dot{m}_{k,f}$ in region II is readily obtained by division of $\dot{\omega}_f$ by the volume V. The calculation for the entire flowfield in the combustor then proceeds from the dump plane (location 2 of Figure 6.2) to the exhaust nozzle by solving (6.1.1-3). The flowfield downstream of the suppression vane is treated as a plug flow reactor in which the global reaction rate model (6.1.17) determines the combustion processes.

6.1.2 Treatment of Boundary Conditions

In order to solve this problem, boundary conditions must be specified adequately. Earlier work has shown that these conditions can be obtained by considering: 1) physical processes, 2) compatibility relations obtained from method of characteristics, and 3) numerical one-sided differences. For the gas phase, the boundaries are chosen to be the inlet throat and the entrance of the exhaust nozzle respectively. The upstream boundary conditions are determined by assuming conservation of total energy and isentropic process from the plenum chamber to the throat, together with the leftward characteristic equation or choked condition, depending on the flow speed at the throat. Treated in this manner, the plenum chamber acts as a perfect acoustic absorber. The acoustic wave radiated into the chamber is efficiently dissipated, no resonance taking place. This assumption is confirmed by the experimental results[2] which indicate that the pressure oscilla-

tions upstream of the throat (location 0 of Figure 6.1) are remarkably small. At the downstream end, the flow is subsonic. Two characteristic lines run from the interior region to the exit; the only physical boundary condition required comes from the Mach number at the exit, which is determined by the area ratio of the combustor to the throat for a choked compact nozzle. The conditions for the liquid phase can be specified with the same procedure described in Chapters 4 and 5.

With the treatment of the inlet and the combustor separately, an internal boundary is introduced at the dump plane. The three compatibility relations, two in the inlet section and one in the combustor, together with the continuity equations for the mass, pressure, and total energy provide the necessary boundary conditions for the finite-difference approximation in each region.

6.2 Discussion of Results

The aforementioned self-adjusting hybrid scheme with artificial compression is used to study the flowfields in two research side-dump ramjet engines operated at the Naval Weapons Center.[2] Both engines have the same inlet systems, but with different combustor lengths. Since static pressure measurements in the diffuser section indicated that the throat was unchoked during all the tests, in this work no shock-fitting algorithm is activated.

The mean flowfields must be determined first in order to provide the necessary initial conditions for the analysis of unsteady motions. The primary input data simulating a typical experiment are given in Table 6.1. The liquid fuel used is RJ-4 fuel having stoichiometric fuel-to-air ratio (by weight) 0.0702. Because the engine always exhibits oscillatory behavior, in the calculation of mean flow fields, the Mach number in the inlet section is fixed by the measured value. The requirement for continuity of pressure across the dump plane is then satisfied by choosing a suitable pre-exponential factor in the chemical reaction rate equation. For unsteady

problems, the condition for a fixed inlet Mach number is relaxed. The internal boundary conditions at both sides of the dump plane are calculated, based on the model given in Section 6.1.

Table 6.1 Computer program input parameters

T_{T_0} = 612 K	L = 350 J/g
$p_{1.5}$ = 7.728 atm	ΔH = 42397 J/g
$\rho_{1.5}$ = 4.23 Kg/m^3	ρ_l = 940 Kg/m^3
$M_{1.5}$ = 0.23	σ_l = 0.023 N/m
T_{T_4} = 2323 K	μ_l = 0.0035 Ns/m^2
M_4 = 0.37	c_l = 2.1J/g–K
φ = 0.91	μ = 3×10^{-5} Ns/m^2
T_{bp} = 480K	c_p = 1.05 J/g–K
K = 0.046 J/s–m–K	

Figure 6.3 summarizes the distributions of various mean flow properties in the baseline engine. The rapid changes of pressure and velocity downstream of the dump plane are due to combustion processes. For the conditions chosen here, more than eighty percent of the chemical reaction takes place in the stirred reactor section. Figure 6.4 shows the bulk density of the liquid fuel and the mass concentration of the fuel vapor in the inlet section. The density decreases rapidly downstream of the injection because of the acceleration of fuel droplets. Most of the fuel is vaporized before entering the combustor. This is the basis for the assumption made earlier that only homogeneous reactions occur in the combustor. The kink on the density distribution corresponds to the position at which the liquid fuel begins to vaporate.

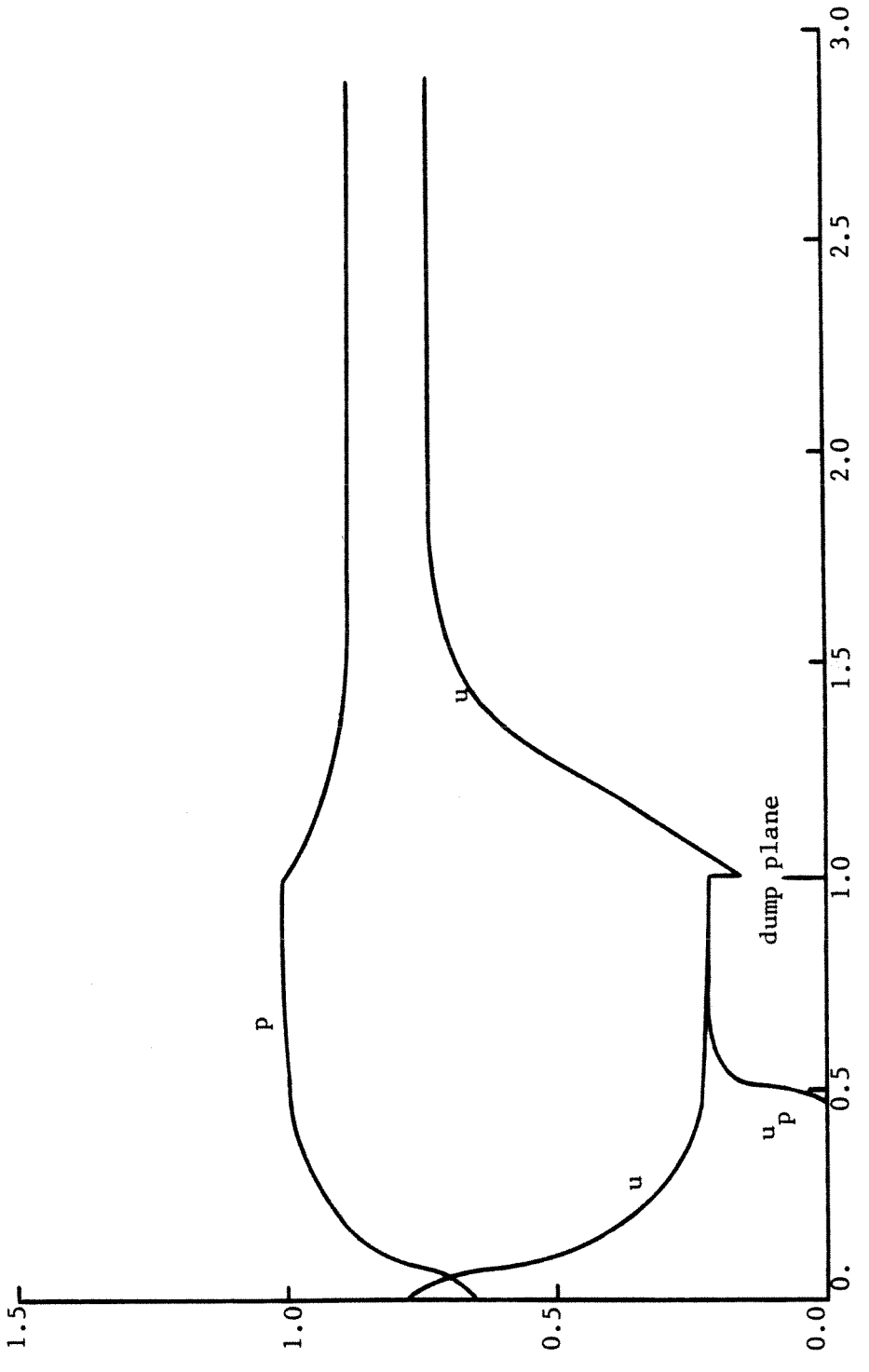

FIGURE 6.3. Distributions of Mean Flow Properties

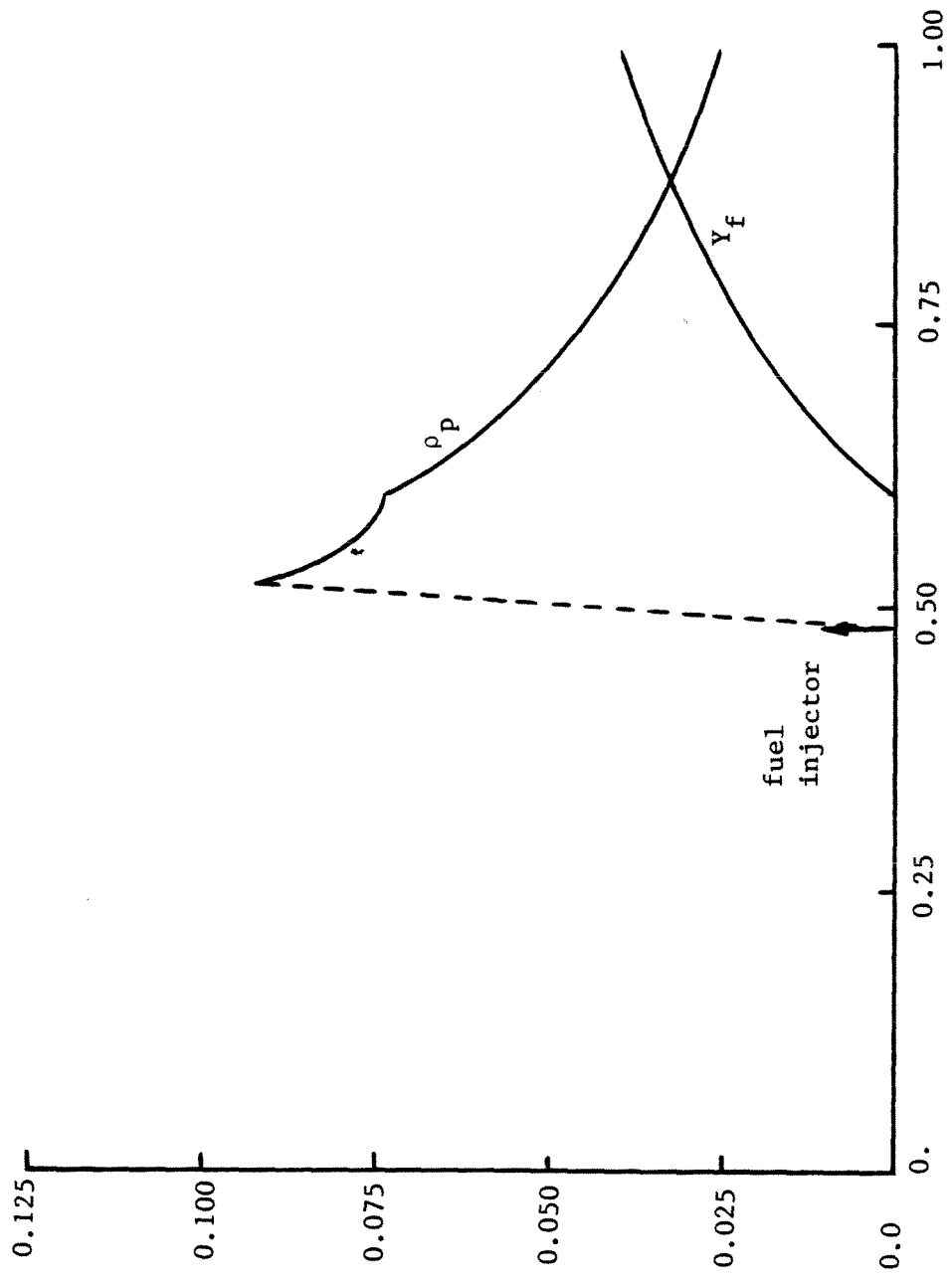

FIGURE 6.4. Distributions of Liquid Fuel Density and Mass Concentration of Fuel Vapor in the Inlet

The stability characteristics of the engine are investigated by examining the response of the flowfield to a disturbance imposed on the mean flowfield. In this case, the mean pressure of the combustor flow is slightly uniformly reduced. Figure 6.5 shows the time history of the pressure at the end of the inlet. The amplitude of the oscillation grows initially, then apparently reaches a limiting value after certain time. Nonlinear effects are clear from the development of this limit cycle and from the structure of the waveform. The pressure distributions at various times within one cycle of oscillations are shown in Figure 6.6. The wave is nearly standing in the combustor with the existence of a pressure node, which corresponds to the first mode oscillation. The acoustic field is driven by the pressure oscillations in the combustor and damped efficiently due to the propagation of waves through the upstream boundary into the plenum chamber.

To make a direct comparison with experimental data and to have a deeper insight into the problem, spectral analysis of the pressure at various locations has been conducted. The power spectral density for the pressure at the exit plane of the inlet is shown in Figure 6.7. The dominant frequency is 320 Hz, compared with the measured value 295 Hz. The wide-band noise is due to the numerical noise and the transient part of the signal. Table 6.2 gives the calculated and the measured frequencies of oscillations.

Table 6.2. Calculated and measured frequencies

mode	$f_{calculated}$	$f_{measured}$
bulk	176 Hz	130 Hz
first	320 Hz	295 Hz
second	624 Hz	590 Hz

Figure 6.8 shows the distributions of amplitude and phase for the first mode. The linear phase distribution in the inlet suggests that the field be dominated by the leftward travelling wave generated by the combustion, the reflected wave being very small. The wave amplitude remains almost constant except in the diffuser section, where the gradual decrease of cross-sectional area toward the throat produces an increase of wave amplitude. The mode structure in the combustion chamber is similar to that for a standing half wave. As far as the absolute magnitude is concerned, the analysis underestimates the fluctuation almost by a factor of 25 percent.

When a short combustor with length 36 inches is tested, the dominant bulk and first mode oscillations occur at 187 Hz and 419 Hz respectively, as shown in Figure 6.9 where the vertical arrows represent the measured results. In comparison with the oscillations in the baseline combustor, the frequencies are greater as a consequence of the reduction of the combustor length. However, the wave amplitude of the first mode drops significantly almost by a factor of eight. This phenomenon may be crudely explained by Rayleigh's criterion[8] which states that to sustain a self-excited standing wave system, the local energy fluctuation must be positively correlated with the pressure fluctuation. Obviously, the condition is best fulfilled if the energy source is located at the pressure antinode. For the baseline (longer) combustor, the active combustion takes place in the forward part of the combustor, close to the pressure anti-node and away from the node point. Therefore, it is easier to drive the first mode instability. Situations are different for the short combustor. Since the combustion is distributed throughout much of the region between the acoustic anti-node and the node , rather away from the node, the amplitude of the pressure oscillation is thus reduced.

Figure 6.10 shows the first mode pressure and phase distributions in the engine with a short combustor. Again, a standing half wave exists in the combustor, and

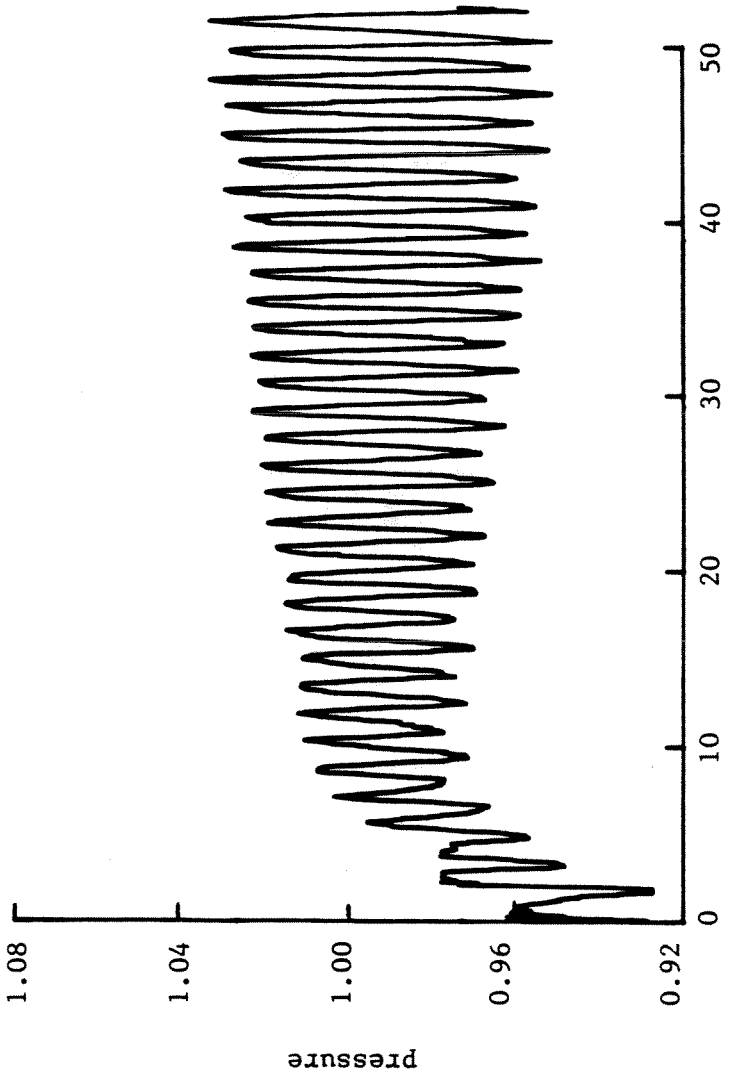

FIGURE 6.5. Time History of Pressure at the End of the Inlet

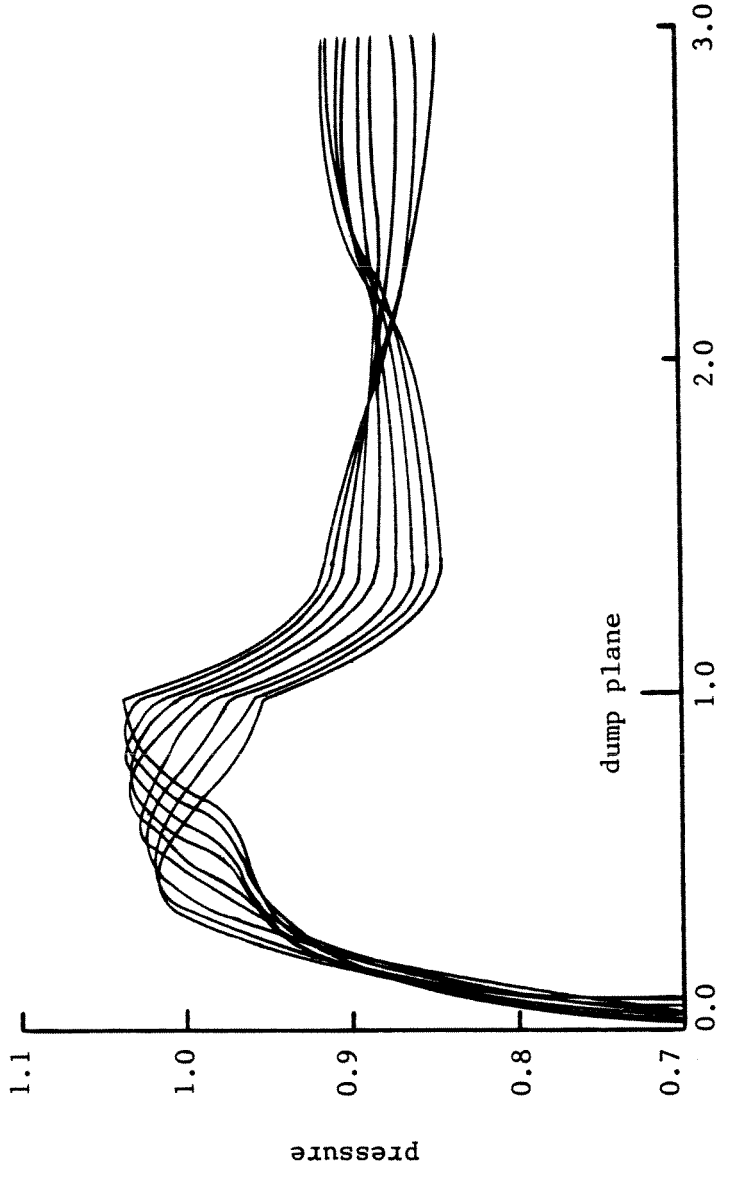

FIGURE 6.6. Pressure Distributions at Various Times within One Cycle of Oscillation

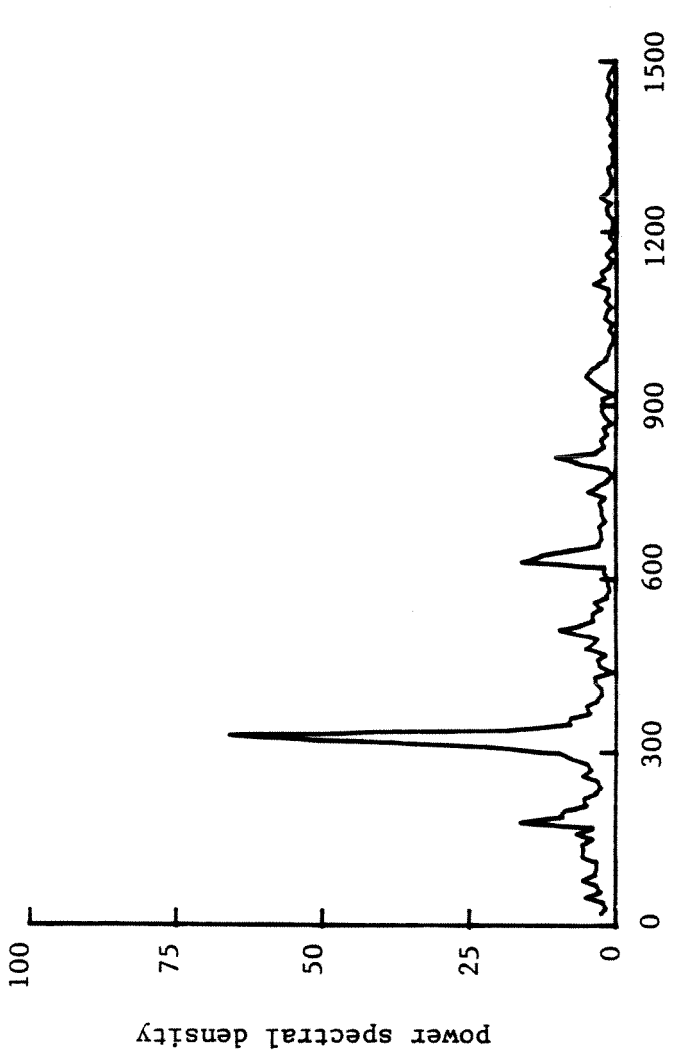

FIGURE 6.7. Power Spectral Density of Pressure at the End of the Inlet (Baseline Combustor)

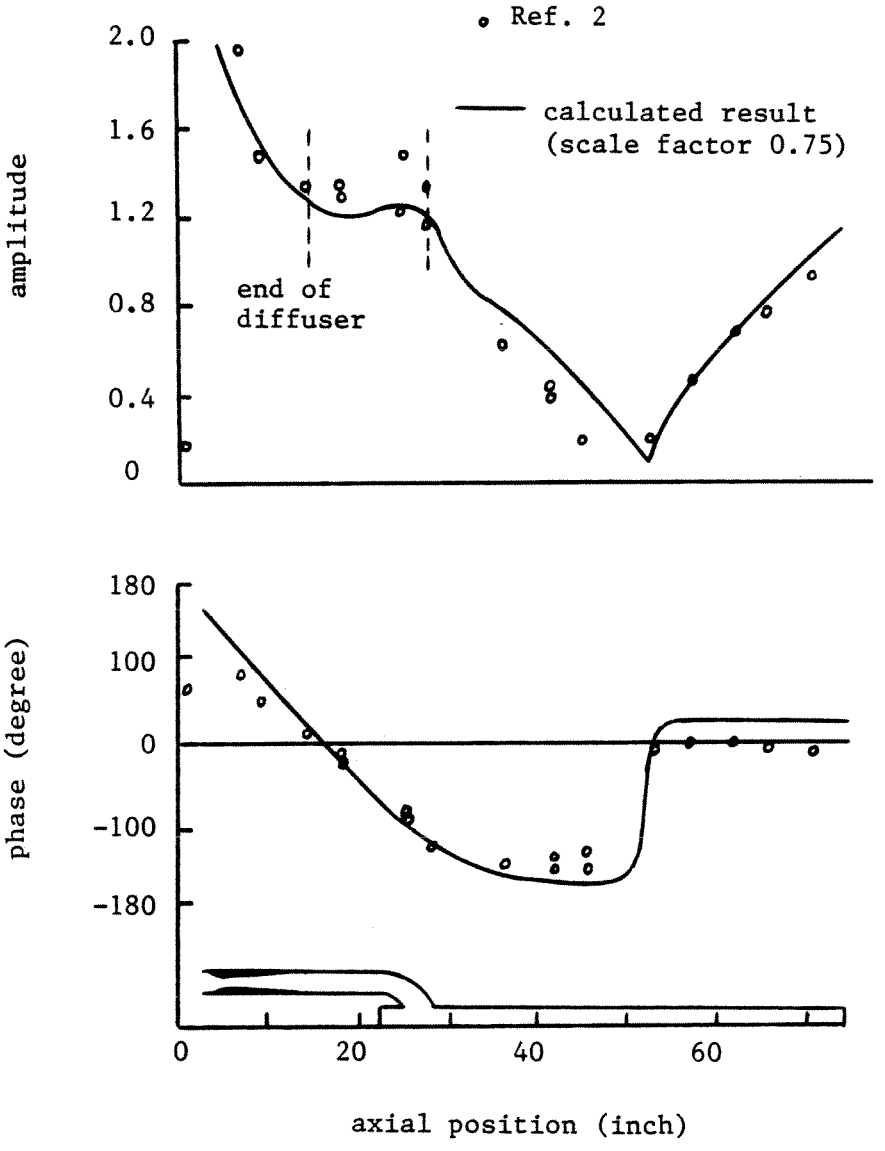

FIGURE 6.8. Distributions of Amplitude and Phase of First Mode Oscillation

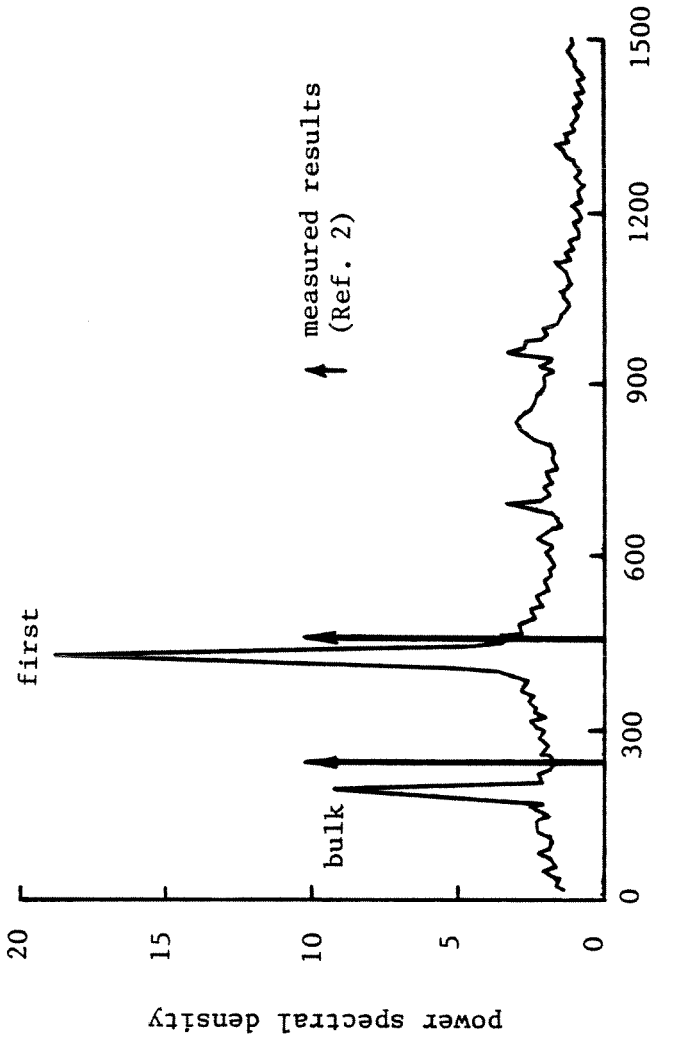

FIGURE 6.9. Power Spectral Density of Pressure at the End of the Inlet (Short Combustor)

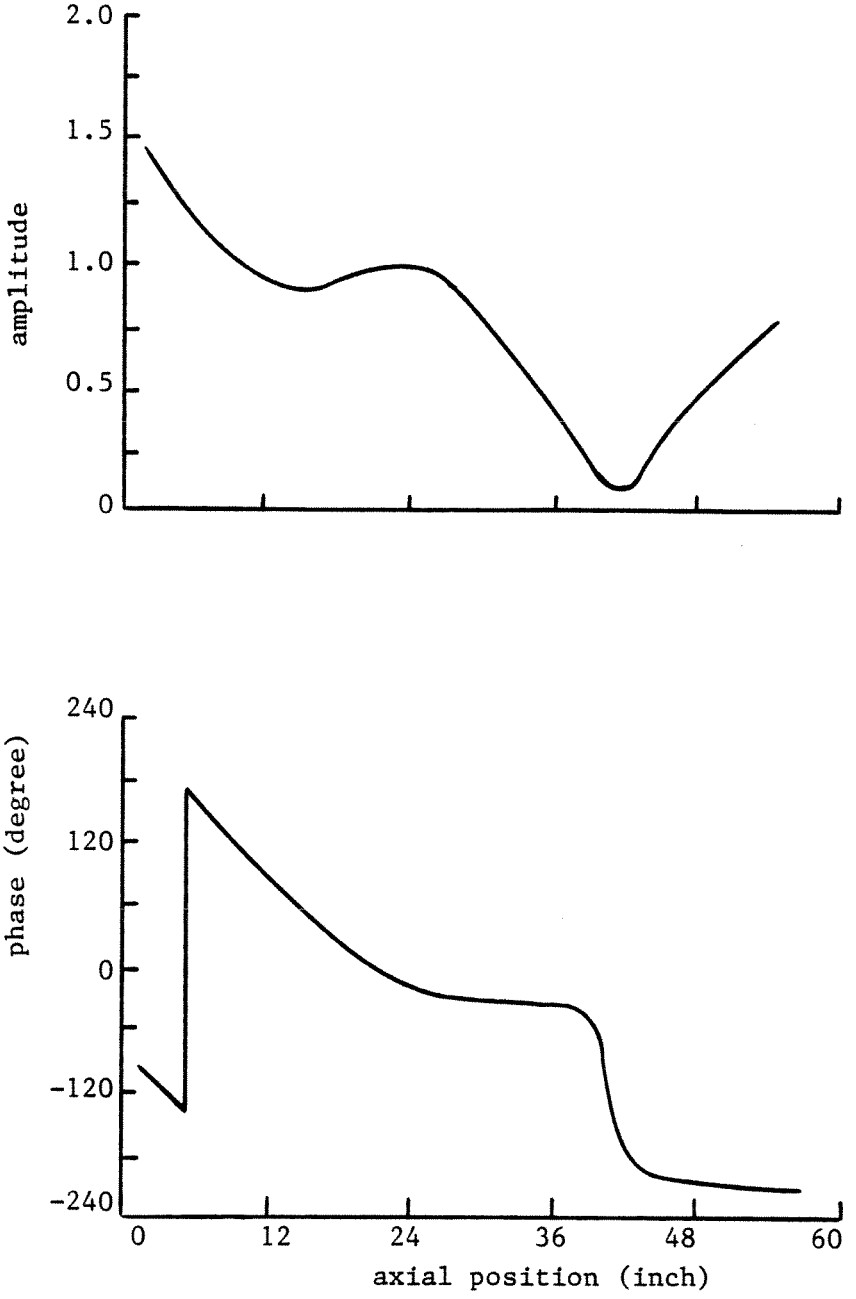

FIGURE 6.10. Distributions of Amplitude and Phase of First Mode Oscillation (short combustor)

the unsteady field in the inlet is dominated by the leftward travelling wave.

6.3 Concluding Remarks

In this chapter, numerical calculations of pressure oscillations in side-dump ramjet engines have been carried out, based on the one-dimensional approximation for two-phase flow. Results have shown favorable comparison with experimental data for the frequencies and mode shapes, but the amplitude of the dominant mode is underestimated almost by a factor of 25%. Nevertheless, the analysis provides a basis for interpreting experimental observations and for predicting some of the global behavior of the engine. Within the present framework, no representation of multi-dimensional effects, such as vortex shedding and recirculating flow, has been attempted. Extension must be made to these matters.

REFERENCES 6

1. Clark, W. H., "Experimental Investigation of Pressure Oscillations in a Side-Dump Ramjet Combustor," *Journal of Spacecraft and Rockets*, Vol.19, No.1, Jan.1982, pp.47-53.

2. Clark, W. H., "Geometric Scale Effects on Combustion Instabilities in a Side-Dump Liquid Fuel Ramjet," *19th JANNAF Combustion Meeting*, Oct.1982.

3. Glassman, I., *Combustion*, Academic Press, Inc., 1977.

4. Spalding, D. B., *Combustion and Mass Transfer*, Pergamon Press, Inc., 1979.

5. Williams, F. A., "Monodisperse Spray Deflagration," in *Liquid Rockets and Propellants*, Vol.2 of Progress in Astronautics and Rocketry, edited by L. E. Bollinger et at, Acadmic Press, Inc., 1960, pp.229-264.

6. Edelman, R. B. and Fortune, O. F., "A Quasi-Global Chemical Kinetic Model for the Finite Rate Combustion of Hydrocarbon Fuels with Application to Turbulent Burning and Mixing in Hypersonic Engines and Nozzles," *AIAA 7th Aerospace Sciences Meeting*, Jan.1969.

7. Swithenbank, J., Poll, I., Vincent, M. W. and Wright, D. D., "Combustion Design Fundamentals," *14th Symposium (International) on Combustion*, 1973, pp.627-636.

8. Rayleigh, J. W. S., *Nature*, Vol.18, 1878, p.319.

NOMENCLATURE 6

A	cross-sectional area
c_l	specific heat of fuel
c_p	constant pressure specific heat of air
D	mass diffusivity
E	activation energy
f	frequency
F_p	drag force between air and fuel droplets
h	enthalpy
K	heat conduction coefficient of air
L	latent heat of liquid fuel
L_f	position coordinate of fuel injector
M	Mach number
$\dot{m}_{k,i}$	rate of consumption of ith species
p	pressure
P_r	Prandtl number
Q_p	heat transfer rate between air and fuel droplets
R	gas constant
r_b	surface regression rate of droplet
r_p	radius of droplet
R_{ei}	Reynold's number based on relative flow velocity, defined by Eq.(4.1.13)
t	time
T	temperature
T_{bp}	boiling temperature
u	velocity
V	volume of stirred reactor
x	position coordinate along the axis of the engine, normalized w.r.t. the inlet length
Y_i	mass fraction of ith species
χ	gas constant, normalized w.r.t. that of the air
γ	ratio of specific heats
μ	viscosity
ν	stoichiometric coefficient
$\dot{\omega}_f$	rate of consumption of fuel in the stirred reactor
ω_p	rate of liquid fuel injected into the main flow

φ	equivalence ratio
ρ	density
ρ_l	density of liquid fuel
σ_l	surface tension of liquid fuel
ΔH	heat of combustion per unit mass of fuel

subscripts

f	fuel
o	oxygen
in	inlet flow
p	liquid phase
sg	value at port of fuel injector
1	value at the exit plane of the inlet
2	value at the inlet plane of the combustor
3	value at the exit plane of the stirred reactor

Chapter 7

CONCLUSION

The work reported here must be regarded as the first step towards a complete understanding of the low frequency longitudinal pressure oscillations in ramjet engines. Because the problems to be treated are complicated and contain many uncertainties, it will not be fruitful to formulate elaborate theories treasured for their alleged predictive powers. The effort has been directed to constructing an acceptable approximate model accommodating the fundamental features of the flowfields.

We started with an analytic linear analysis, followed by a numerical nonlinear analysis. The main results of the linear analysis are frequencies, growth constants, mode shapes, and perhaps more important, the basis for nonlinear analysis. Chapter 2 deals with the longitudinal unsteady motions in several laboratory coaxial devices operated at the Naval Weapons Center. The engine is approximated by division into two parts: the inlet and the dump combustor, in each of which we assume the mean flowfield to be uniform. The oscillatory field is therefore the superposition of two simple plane acoustic waves running upstream and downstream, and an entropy wave convected downstream. With appropriate matching conditions at the interface, the stability characteristics of the engine can be determined.

The assumption of the uniform mean flowfield in the dump combustor has been released in Chapter 3. We have modeled the flow in three regions: the upstream flow of reactants, a recirculation zone and a region containing combustion products. The flame zone and the shear layer at the edge of the recirculation zone have been considered infinitesimally thin. With that mean flowfield, small amplitude motions have been calculated as one-dimensional

waves. The apparent mismatch between a two-dimensional mean flowfield and a one-dimensional oscillatory field can be easily resolved using the integral formulation. Distributions of the amplitude and phase have shown good agreement with experimental data taken at the California Institute of Technology.

There are several important aspects of linear analysis which require extensive attention. First, the representation of the unsteady combustion is incomplete. Within the flame sheet model, the unsteadiness of combustion appears in the fluid dynamic stretching of the sheet due to the local velocity and pressure fluctuations. The flame speed itself remains constant. Extension should be made to finite-rate chemical reaction. Second, only two-dimensional coaxial configurations have been treated. Extension to axisymmetric and side-dump devices is required. Third, to date we have only analyzed one-dimensional unsteady motions with a two-dimensional mean flowfield. Extension must be made to two-dimensional wave motions. This probably is the key issue of the entire problem. As a consequence, a more realistic and accurate representation of the shear layer and the flame front is required as well.

As fas as the numerical nonlinear analysis is concerned, we have carried out approximate numerical calculations for the inlet diffuser flow with a shock wave. Nonlinear behavior of the shock wave in the inlet is a necessary part of the problem since we need this information as a boundary condition. We did not intend to construct a complete theory of diffusers; we are interested only in the way in which the diffuser influences unsteady motions in the engine. Both viscous effects and the influences of injecting fuel/air mixture have been accounted for. The response of a normal shock wave to various disturbances has been investigated in great detail. Because the viscous boundary layers have been assumed to be steady and attached to the wall, the flow separation, either due to the unfavorable pressure gradient or to the shock wave/boundary layer

interaction, has not been accommodated. These merit thorough consideration in the future.

Numerical calculations have also been conducted for the pressure oscillations in side-dump ramjet engines, based on the one-dimensional model for two-phase flow. Combustion processes have been crudely modeled as a stirred reactor, occupying the forward portion of the combustor, followed by a length of plug flow. The unsteady behavior of the engine has been determined by its response to a small disturbance imposed on the mean flowfield. Within the one-dimensional approximation, the apparent multi-dimensional effects, such as vortex combustion and recirculating flow in the vicinities of the inlet/combustor interfaces, have been neglected. Future effort should be devoted to correcting this matter.